Université catholique de Louvain
Faculté des Sciences
Institut de Recherche en Mathématique et Physique
Centre for Cosmology, Particle Physics and Phenomenology

A New Method for Mapping Detector Material in Situ and a Matrix Element Approach to the Search for Heavy Di-muon Resonances at the LHC

Doctoral dissertation presented by

Suzan Başeğmez

in fulfillment of the requirements for the degree of Doctor in Sciences

Prof. Giacomo Bruno (Advisor)	UCL, Belgium
Prof. Jean-Marc Gérard (Chairman)	UCL, Belgium
Prof. Fabio Maltoni	UCL, Belgium
Prof. Steven Lowette	VUB, Belgium
Prof. Andrea Giammanco	UCL, Belgium

September 2015

Curiouser and curiouser! [*]

---

[*] For the 150th anniversary of Lewis Carroll's *Alice's Adventures in Wonderland*

Acknowledgments

After all these years, I learned that sometimes a PhD can be a journey to the inner self, discovering the fundamental ingredients that have motivated me to follow such a path in my life. Of course there are many people who have supported me to continue this direction in academia, and who helped and inspired me during my studies.

First of all, I would like to thank my advisor Prof. Giacomo Bruno for opening up the door and letting this adventure begin. I would like to express my sincere gratitude for his guidance and support throughout my thesis studies and his effort of making my research more interesting and comprehensive. In particular, I thank him very much for his help for correcting this thesis text, as well as his comments to enrich my knowledge.

Besides my thesis advisor, I would like to thank the rest of my thesis committee: Prof. Jean-Marc Gérard, Prof. Fabio Maltoni, Prof. Andrea Giammanco and Prof. Steven Lowette, for their valuable comments and suggestions that I received from various perspectives. Also, I would like to thank Prof. Vincent Lemaitre, the group leader, for providing the facilities and resources to conduct research in a stimulating and fruitful way.

I would also like to thank Prof. Christophe Delaere and Prof. Christophe Ringeval for filling lunchtimes and gatherings with their enthusiasm and friendship. My sincere thanks goes to our precious secretaries Ginette and Carine; not only for making the bureaucratic stuff much easier for me, but also for their warm welcome and kindness.

Furthermore, I would like to acknowledge Loic Quertenmont (my ultimate office mate), Pierre Artoisenet, Davide Pagano and Olivier Mattelaer, for their insightful suggestions and all the help I received during my studies, which is very much appreciated. And, of course, I would like to mention Pavel Demin and Jérôme de Favereau, for their invaluable support of the CP3 computing facilities. I would like to thank also many of my other friendly colleagues from CP3, whose names will not fit in this page, for their discussions and helping me to get through all the paperwork.

I greatly value the friendship of many friends I have met during my PhD, especially Larissa Lorenz, Sean Murray, Lawrence Soung Yee and Simone Zonetti. Thanks for all the joy and fun we had together in Belgium and outside.

Last but not least, I would like to thank my family and particularly my husband, Tristan du Pree. Thanks sweetie for all your love, support and help in my hard times and the joy in good times. I am happy to discover you.

Contents

List of Figures

List of Tables

Introduction

High energy particle physics is a search for the fundamental description of nature. Our current understanding of nature and fundamental interactions are formulated in a theory called the Standard Model. Since the beginning of the 60s, with the quark[†] model and the electroweak theory, the Standard Model has been established and developed. Many of the predictions by the theory have been verified by experimental measurements with high precision. For example, the prediction of the Higgs boson, which is the key element to explain the masses of elementary particles, has already been confirmed by the high energy experiments.

The existence of a Standard Model scalar boson was observed by both the CMS and ATLAS experiments operating at the Large Hadron Collider (LHC) at CERN during the Run1 data taking. The triumph of high energy particle psychics in 2012 was this observation which brought the Nobel Price in Physics[‡] to François Englert and Peter W. Higgs in 2013. Apart from this observation, the LHC experiments did not find any sign of particles belonging to physics Beyond the Standard Model, then the question is *"Is that all in nature?"*

[†] Gell-Mann has introduced the name "quark", as a reference to the novel Finnegans Wake by James Joyce ("Three quarks for Muster Mark!")

[‡] "for the theoretical discovery of a mechanism that contributes to our understanding of the origin of mass of subatomic particles, and which recently was confirmed through the discovery of the predicted fundamental particle, by the ATLAS and CMS experiments at CERN's Large Hadron Collider" [1]

There are still many open questions awaiting to be answered. For example: why is there a matter-antimatter asymmetry in the universe? what is the dark matter and dark energy? is unification of forces possible? Moreover, how can gravity fit into this model?

The attempts to answer these questions are formulated in various theories Beyond the Standard Model. Many possible scenarios have been thought as possible candidates. In particular, Grand Unification and Extra Dimensions models, answering some of the questions mentioned above in different aspects, predict the existence of new heavy neutral particles at the TeV scale.

To search for these particles, detectors based on cutting-edge technologies have been developed and used in the past Tevatron and current experiments at the LHC which are world-wide collaborations. The di-muon decay channel is a clean final state to search for new particles at high mass. The searches conducted in Tevatron experiments, at the center-of-mass energy of 1.96 TeV in proton-antiproton collisions and in the LHC experiments at 7 and 8 TeV in proton-proton collisions, did not find any significant deviations from the expected background in the di-muon mass spectrum.

The possible explanations of the lack of the observation could be that either nature does not include such extra particles, or the interactions of such exotic particles and their decays to Standard Model particles could be weaker than the predictions. More sensitive analysis methods can improve the sensitivity of the search methods used and they can also help to clarify these points.

This thesis is mainly focused on the development and investigations of a potentially more sensitive analysis method than the commonly adopted ones, based on the use of a Matrix Element Method, in the search for di-muon resonances with high-mass ($\gtrsim$200 GeV/c^2). The thesis will also present a novel method for measuring the amount of material in a tracking detector. These methods have been validated and applied to the collision data gathered during 2010 and 2011 with the CMS experiment at the LHC.

Chapter 1 will be a brief description of the Standard Model and the review of some of the theories that attempt to extend the Standard Model. The theoretical predictions for the background and signal models in the di-muon final state will be given. The main physical quantities which can be used as observables in an experimental measurement will be discussed as well. Chapter 2 will be the description of the experimental set-up. The CMS experiment and the sub-systems of the detector that are used to reconstruct the muons will be described. Chapter 3 is the presentation of a new method for the improvement of the material description and measurement of the material distribution of the CMS inner tracker. The method and the obtained results with the collision data will be presented.

Finally, the last three chapters (4, 5 and 6) will focus on a likelihood analysis technique based on the Matrix Element Method, applied to the search for narrow resonances in the di-muon channel. The statistical approach and the treatment of nuisance parameters will be explained in detail. After the comprehensive validation studies of this new technique with Monte Carlo generated events, the implementation of the method and the obtained results with CMS 7 TeV collison data, in terms of a local significance and an upper limit for the considered search region of the invariant mass, will be presented.

The thesis will conclude with a summary of the obtained results of the studies and of the possible improvements for future searches for the upcoming LHC Run2 data taking.

Chapter 1

The Standard Model and Beyond

1.1 The Standard Model

The physics of the subatomic particles and their interactions are established in the theoretical framework called the Standard Model (SM). It incorporates three fundamental forces of nature: the electromagnetic, weak and strong forces. The SM is the relativistic quantum field theory where each particle is described by a field (for more information see [2, 3]). The interactions between elementary particles are represented in the SM Lagrangian by local gauge invariance. A Lagrangian is a mathematical formulation of dynamics, and it determines the equation of motion.

The SM, from a theoretical point of view, is defined on the basis of gauge symmetries [3]. All the particles and their interactions are described by certain groups of symmetry transformation. The SM is a gauge theory with a symmetry group of

$$SU(3)_C \times SU(2)_L \times U(1)_Y$$

The $SU(3)_C$ symmetry group defines the Quantum Chromo-Dynamics (QCD) theory that describes the strong interactions, where C refers to color quantum numbers. Quarks are the objects described by this group with three possible color states. The group of $SU(2)_L \times U(1)_Y$ is the Electroweak (EWK) theory describing the Quantum Electodynamics (QED) and the weak interactions where the fermions are the objects represented by the group. In $SU(2)_L$, the conserved quantum number is the weak isospin T, and L stands for the left-handed fermions. In $U(1)_Y$, the conserved quantum number is the weak hypercharge which is indicated as Y.

The theory leads to the *gauge bosons* which are the mediators of the three forces. All force carriers are “bosons” having an integer spin: the electromagnetic force carrier is the photon γ, the weak interaction is mediated by $W^{\pm}$ and Z (more specifically Z^0) bosons and the strong force is carried by gluons g. The gravitational force, which is expected to have a hypothetical force carrier, the *graviton* with spin 2, is not included in the SM.

The elementary constituents of matter are leptons and quarks. They are categorized as “fermions” with half-integer spin. The quantum numbers of fermions determine how they interact. All fermions can interact weakly, the fermions that have electrical charge interact electromagnetically, the color charged fermions have strong interactions. Leptons are the fermionic elementary particles which can only interact electroweakly. Neutrinos are electrically neutral leptons which can interact weakly and recent experimental evidence of neutrino oscillation experiments [4, 5] show that they have non-zero mass values. The consequences of non-zero neutrino masses and their implications are not discussed in this thesis.

All fermions are divided into three categories each composed of two quarks and two leptons described as “generations”. As a consequence of symmetry transformation under charge conjugation-parity and time so-called “CPT invariance”, each particle is further associated to an anti particle which transforms under CPT. Figure 1.1 and 1.2 show the fundamental particles and a schematic drawing of the interactions.

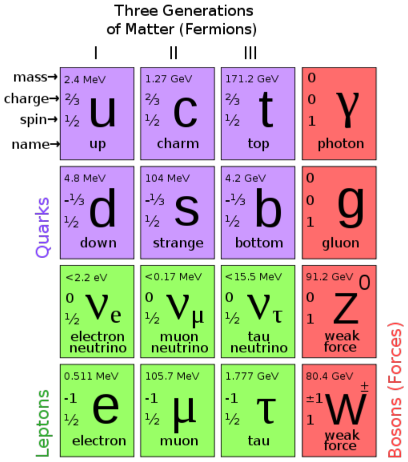

	I	II	III	
mass→ charge→ spin→ name→	2.4 MeV ⅔ ½ u up	1.27 GeV ⅔ ½ c charm	171.2 GeV ⅔ ½ t top	0 0 1 γ photon
	4.8 MeV -⅓ ½ d down	104 MeV -⅓ ½ s strange	4.2 GeV -⅓ ½ b bottom	0 0 1 g gluon
	<2.2 eV 0 ½ ν_e electron neutrino	<0.17 MeV 0 ½ ν_μ muon neutrino	<15.5 MeV 0 ½ ν_τ tau neutrino	91.2 GeV 0 1 Z^0 weak force
	0.511 MeV -1 ½ e electron	105.7 MeV -1 ½ μ muon	1.777 GeV -1 ½ τ tau	80.4 GeV ±1 1 $W^\pm$ weak force

Fig. 1.1: The elementary particles described by the SM.

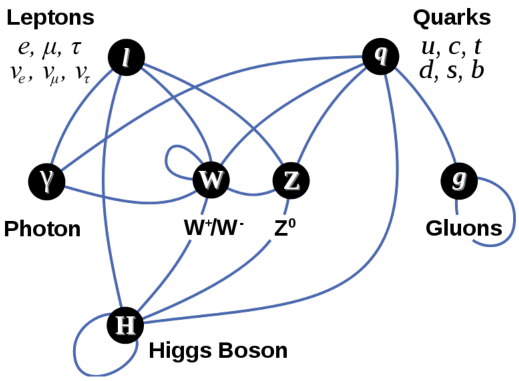

Fig. 1.2: The elementary particles and their interactions, which are shown as continuous lines.

The Lagrangian of the electroweak model in the SM does not include the masses of bosons. This is un-natural to describe the real world, since the only vector boson observed in nature that does not have a mass is the photon. The addition of mass terms to the SM Lagrangian violates the local gauge invariance and spoils the renormalizability of the theory [6]. The bosons and fermions acquire their masses via the mechanism of *spontaneous symmetry breaking*. As today the mechanism is also known as BEH (Brout–Englert–Higgs) mechanism. The detailed description of this mechanism can be found in references [7, 8]. A scalar field is introduced into the theory to provide the symmetry breaking which leads to the prediction of a scalar particle, the Higgs boson.[*] The existence of such scalar particle is already observed by the CMS and ATLAS experiments at the LHC [9, 10]. The combined analysis performed by CMS using the high mass resolution channels of $H \to \gamma\gamma$ and $H \to ZZ^*$ gives a mass measurement of $m_H = 125.03^{+0.26}_{-0.27}(stat.)^{+0.13}_{-0.15}(syst.)$ [11].

After the symmetry breaking, W and Z bosons gain masses and the relation between their masses is

$$M_Z = M_W / \cos\theta_W$$

where θ_W is called the Weinberg or electroweak mixing angle. The latest experimental measurement performed by CMS [12] gives a measurement of

$$\sin^2\theta_W = 0.2287 \pm 0.0020(stat) \pm 0.0025(syst). \tag{1.1}$$

In the SM, the scalar H field gives masses to fermions via Yukawa interactions with the fermion field. After the spontaneous symmetry breaking, a Yukawa interaction leads to a fermion mass of $m_f = g_f v/\sqrt{2}$ in which g_f is the interactions strength and v is the vacuum expectation value of the H field. The SM contains a number of Yukawa couplings to fix the fermion masses. The model itself does not explain the wide range of the couplings (see reference [6, p.284]).

---

[*] Throughout this thesis the Higgs boson will be indicated as H.

1.1.1 The Drell-Yan Production at Hadron Colliders

Hadrons (or mesons) are bound state of three (or two) quark compositions. A proton, for example, is made of two up and one down quark. It is not possible to free a quark from a proton and observe it separately since the quarks are held together by strong forces inside the proton. On the other hand, it is possible to let the quarks (and gluons) inside hadrons to interact by colliding them at high energies. At high energy hadron collisions, a particular process can occur due to high energetic quark-antiquark annihilation. A quark and an anti-quark from the colliding beams can annihilate to produce a lepton pair in the hard scattered collisions. This process is first pointed out by Drell and Yan [13], and therefore it is called the Drell-Yan production.

The lowest order Drell-Yan (DY) production can happen by the neutral current which leads to the production of a neutral Z or a virtual photon. Let us describe this process in the following section, as it is the main irreducible background process to the physics process of our interest, which is described in the section after. The material in the following section is mostly compiled from the ref.[6].

1.1.1.1 Cross section of $pp \to \gamma^*/Z \to l^+l^-$ at the LHC

In proton-proton collisions, the production cross section σ_{DY} for producing a lepton pair via the Drell-Yan process will be the sum of the sub-processes of $q\bar{q} \to \gamma^*/Z \to l^+l^-$. Considering the fact that the parton content of the proton is encoded in the Parton Distribution Functions (PDF) [14], the resulting cross section therefore should be weighted with the PDF[†]. By summing over all quark-antiquark combinations one can obtain the total cross-section

---

[†] Throughout the thesis the abbreviation of PDF in capital letters is referring to Parton Distribution Functions inside the proton. Another abbreviation of "*pdf*" is also used which refers to probability density functions and for distinction it will be indicated by small letters as pdf.

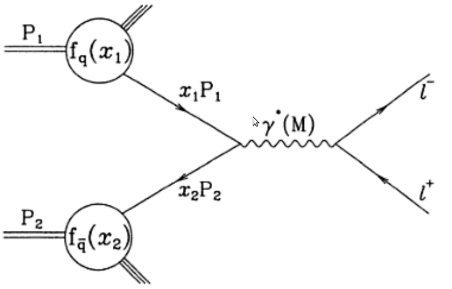

Fig. 1.3: Lepton pair production via quark-antiquark annihilation in the Drell-Yan model [6].

$$\sigma_{DY} = \sum_q \int dx_1 dx_2 f_q(x_1) f_{\bar{q}}(x_2) \hat{\sigma}_{q\bar{q}\to\gamma^*/Z\to l^+l^-}, \tag{1.2}$$

where $\hat{\sigma}_{q\bar{q}\to\gamma^*/Z\to l^+l^-}$ indicates the partonic cross section of the production of lepton pairs.

The partonic sub-process cross section depends on the energy ($\hat{s}$) available in the hard scattering and is given by [6]

$$\hat{\sigma}_{q\bar{q}\to\gamma^*/Z\to l^+l^-}(\hat{s}) = \frac{4\pi\alpha^2}{3\hat{s}} \frac{1}{N_c} \left(Q_q^2 - 2Q_q V_l V_q \chi_1(\hat{s}) + (A_l^2 + V_l^2)(A_q^2 + V_q^2)\chi_2(\hat{s})\right), \tag{1.3}$$

where α and N_c are the electromagnetic coupling constant [15] and the color averaging factor, respectively. If p_1 and p_2 are the four-momenta of the incoming quarks, $\hat{s}$ is defined as $\hat{s} = (p_1 + p_2)^2$ and by momentum conservation it is equal to the invariant-mass squared of leptons. The terms $\chi_1(\hat{s})$ and $\chi_2(\hat{s})$ are defined by

$$\chi_1(\hat{s}) = \kappa \frac{\hat{s}(\hat{s} - M_Z^2)}{(\hat{s} - M_Z^2)^2 + \Gamma_Z^2 M_Z^2}, \tag{1.4}$$

$$\chi_2(\hat{s}) = \kappa^2 \frac{\hat{s}^2}{(\hat{s} - M_Z^2)^2 + \Gamma_Z^2 M_Z^2}, \tag{1.5}$$

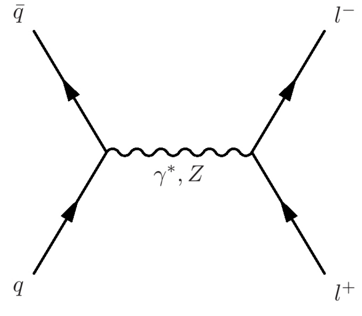

Fig. 1.4: The lowest order Feynman diagram of lepton pair production in the Drell-Yan process.

where M_Z and Γ_Z are the mass and the full width of the Z boson, and κ is equal to

$$\kappa = \frac{\sqrt{2} G_F M_Z^2}{16\pi\alpha}. \tag{1.6}$$

The equation 1.3 has specific features of dependence of the energy at the hard scattering.

- Far below the Z mass pole, the process is dominated by $q\bar{q} \to \gamma^* \to l^+l^-$. The partonic cross-section for this process is given by

$$\hat{\sigma}_{q\bar{q}\to\gamma^*\to l^+l^-}(\hat{s}) = \frac{4\pi\alpha^2}{3\hat{s}} \frac{1}{N_c} Q_q^2. \tag{1.7}$$

  In general, because the incoming quark and antiquark have a spectrum of the collision energies of $\sqrt{\hat{s}}$, it is appropriate to take the differential cross section of the production of lepton pairs. Thus, the differential cross section for the production of a lepton pair with an invariant mass of M via the Drell-Yan process at leading order is equal to

$$\frac{d\hat{\sigma}}{dM^2} = \frac{\sigma_0}{N_c} Q_q^2 \delta(\hat{s} - M^2), \quad \sigma_0 = \frac{4\pi\alpha^2}{3M^2}. \tag{1.8}$$

The square of the $q\bar{q}$ collision energy $\hat{s}$ is related to the overall proton collision energy by $\hat{s} = (p_1 + p_2)^2 = x_1 x_2 s$. Using this relation, the total differential cross section is

$$\frac{d\sigma}{dM^2} = \int_0^1 dx_1 dx_2 \sum_q \{f_q(x_1) f_{\bar{q}}(x_2) + (q \leftrightarrow \bar{q})\} \times \frac{d\hat{\sigma}}{dM^2}(q\bar{q} \to l^+ l^-). \tag{1.9}$$

The $\bar{q}q$ addition is indicated by $q \leftrightarrow \bar{q}$. The double-differential cross-section, using the definition of $x_1 = \sqrt{M^2/s}\exp(y)$, $x_2 = \sqrt{M^2/s}\exp(-y)$ and rapidity as

$$y = \frac{1}{2}\ln\left(\frac{x_1}{x_2}\right), \tag{1.10}$$

will be given by

$$\frac{d^2\sigma}{dM^2 dy} = \frac{\sigma_0}{N_c s}\left[\sum_q Q_q^2 \{f_q(x_1) f_{\bar{q}}(x_2) + (q \leftrightarrow \bar{q})\}\right]. \tag{1.11}$$

Therefore, by measuring the double-differential cross section of lepton pairs of M in rapidity, one can give the direct measurement of the quark-antiquark distribution inside the proton, thus confirming the parton model (see ref. [16]).

- On the Z pole, the cross section is dominated by the production of a neutral Z boson

$$\hat{\sigma} \propto \frac{\hat{s}^2}{(\hat{s} - M_Z^2)^2 + \Gamma_Z^2 M_Z^2}, \tag{1.12}$$

which has a shape of a Breit-Wigner resonance with the width Γ_Z (see eq. 1.15).

1.1.1.2 Z Boson Production and Decay Properties

In neutral currents, i.e. producing a Z boson or a photon, the couplings of the fermions to the Z boson are given by vector and axial-vector couplings as

Fermions	Q_f	V_f	A_f
u,c,t	2/3	(1/2 - 4/3$\sin^2\theta_W$)	1/2
d,s,b	-1/3	(-1/2 +2/3 $\sin^2\theta_W$)	-1/2
ν_e, ν_μ, ν_τ	0	1/2	1/2
e,μ,τ	-1	(-1/2 + 2 $\sin^2\theta_W$)	-1/2

Tab. 1.1: Couplings of fermions to the Z boson [6].

$$\begin{aligned} V_f &= T_f^3 - 2Q_f \sin^2\theta_W, \\ A_f &= T_f^3, \end{aligned} \tag{1.13}$$

where T_f^3 is the third component of the weak isospin and Q_f is the charge of the fermion in units of the positron electric charge e ‡. The couplings are summarized in table 1.1.

The partial decay widths of Z bosons to fermion-antifermion can be calculated at leading order electroweak perturbation theory. The invariant matrix element squared for this process summed (averaged) over final (initial) polarization is given by

$$\overline{\sum}|M|^2 = \frac{8}{3}\frac{G_F M_Z^4}{\sqrt{2}}(|V_f|^2 + |A_f|^2). \tag{1.14}$$

The total decay width is the sum of all partial widths

$$\Gamma(Z) = \sum_f \Gamma(Z \to f\bar{f}). \tag{1.15}$$

The final result for the partial width of the Z is

$$\Gamma(Z \to f\bar{f}) = N_C \frac{G_F M_Z^3}{6\sqrt{2}\pi}(|V_f|^2 + |A_f|^2) \tag{1.16}$$

where N_C is the color normalization factor which is 1 for leptons and 3 for quarks. The G_F is the Fermi coupling constant [17]. Using the partial widths of Z, the branching ratios can be calculated

---

‡The relation between e and weak SU(2) charge g_W is $e = g_W \sin\theta_W$

Decay Process	Coupling	Branching Ratio
$Z \to \nu_e\bar{\nu}_e, \nu_\mu\bar{\nu}_\mu, \nu_\tau\bar{\nu}_\tau$	1/2	3× 6.8%
$Z \to e^+e^-, \mu^+\mu^-, \tau^+\tau^-$	1/4 +(1/2 -2 $\sin^2\theta_W)^2$	3× 3.4%
$Z \to u\bar{u}, c\bar{c}$	3[1/4 +(1/2 - 4/3$\sin^2\theta_W)^2$]	2× 11.8%
$Z \to d\bar{d}, s\bar{s}, b\bar{b}$	3[1/4 +(1/2 - 2/3$\sin^2\theta_W)^2$]	3× 15.2%

Tab. 1.2: Z boson decays to fermion-antifermion [6].

for various fermion-antifermion decay modes as shown in table 1.2. The total width and mass of Z boson are measured to be [17]

$$\Gamma_Z = 2.4955 \pm 0.0009 \text{ GeV for } M_Z = 91.1874 \pm 0.0021 \text{GeV}/c^2. \tag{1.17}$$

At hadron colliders one can usually detect the decays of Z to charged leptons efficiently. Although the hadronic decay modes of Z are enhanced compared to the leptonic decay modes, there is a large QCD background production of two-jet. The fraction of the partial width of Z decays to neutrinos is experimentally measured by subtracting the detectable part from the total width.

- Around the Z mass, there will be interference of a Z and a photon. Therefore, the cross section will be related to interference term

$$\hat{\sigma} \propto \frac{\hat{s}(\hat{s} - M_Z^2)}{(\hat{s} - M_Z^2)^2 + \Gamma_Z^2 M_Z^2}. \tag{1.18}$$

A proton consists of three valence quarks, sea quarks and gluons, therefore in proton-proton collisions not only the valence quarks but also gluons and sea quarks can participate to the interactions where each constituent carries a fraction of the momentum of the colliding proton. In figure 1.3 these fractions for interacting quarks are indicated by x_1 and x_2. The PDF for the colliding partons are given at a factorization scale μ^2, for a momentum transfer of Q^2. The choice of PDF, therefore, will have an effect on the cross section for Drell-Yan process. For clarity, the total cross section can be written as

$$\begin{aligned} \sigma_{DY} = & \sum_q \int dx_1 dx_2 f_q(x_1, \mu^2) f_{\bar{q}}(x_2, \mu^2) \\ & \times \hat{\sigma}_{q\bar{q} \to \gamma^*/Z \to l^+l^-}(x_1 P_1, x_2 P_2, Q^2, \mu^2). \end{aligned} \tag{1.19}$$

Figure 1.5 shows the analytical parametrization of the parton distribution functions [12] using the CTEQ6 [18] parton distribution functions.

1.1.1.3 Higher Order Corrections

The perturbative QCD, QED and weak corrections can be considered among the additional effects on the total cross section. To take into account the higher order QCD corrections, the cross section should be modified with additional terms as

$$\begin{aligned} \sigma = & \sum_q \int dx_1 dx_2 f_q(x_1) f_{\bar{q}}(x_2) \\ & \times \left(\hat{\sigma}_0 + a\hat{\sigma}_1 + a^2\hat{\sigma}_2 + ...\right)_{q\bar{q} \to \gamma^*/Z \to l^+l^-} , \end{aligned} \tag{1.20}$$

with $a = \alpha_S(M^2)/2\pi$. Currently, the cross section for Drell-Yan production can be calculated up to and including $\hat{\sigma}_2$ terms, at so called next-to-next-to-leading order (NNLO). Using the NNLO predictions, the events that are generated at leading order (LO) can be scaled to higher order

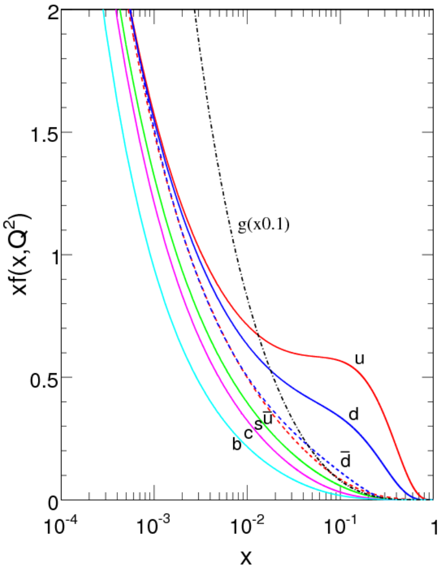

Fig. 1.5: Analytical parameterization of the parton distribution functions xf(x,Q^2) at Q=100 GeV using the CTEQ6 numerical computation for the various quarks, antiquarks, and the gluon [12].

with the scale factors obtained, often called the “k-factor”. QED corrections are model independent and can include initial and final state radiation. The pure weak corrections are small for the Z production [19].

In most cases it is assumed that colliding partons have a negligible transverse momentum relative to the direction of incoming proton beams. Therefore, leptons produced in the DY process are expected to be back-to-back in the transverse plane. However, partons inside proton have a fraction of momentum of protons and can be boosted in the transverse direction. Therefore the produced leptons are expected to have, on average, a small boost on the transverse plane. Additionally, the leading order DY cross-section can receive additional contributions from $q\bar{q} \to g + \gamma^*/Z$ and $qg \to q + \gamma^*/Z$ which makes di-muon events to have a high transverse momentum.

1.1.1.4 Experimental Measurements

Drell-Yan production of lepton pairs have been studied by the CMS [20, 21] and ATLAS [22, 23] experiments. Figure 1.6 shows the invariant-mass spectrum in the di-muon channel obtained by CMS [20] normalized to the Z resonance region. As can be seen, the measurements are in very good agreement with NNLO predictions by FEWZ [24] shown as blue line at the statistically dominated low-mass region.

Similarly, figure 1.7 shows the obtained invariant-mass distribution in the di-electron decay channel by the ATLAS experiment [23].

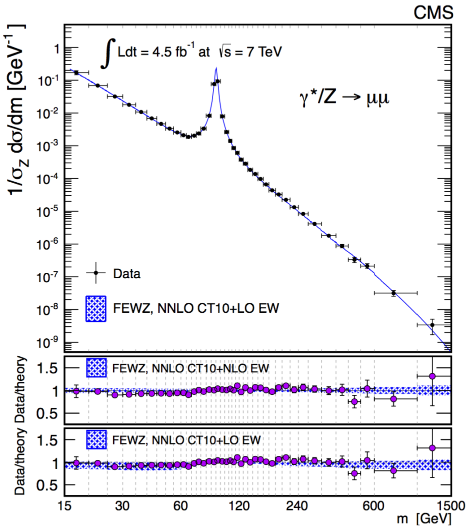

Fig. 1.6: The Drell-Yan invariant mass spectrum in the dimuon channel, normalized to the Z resonance region $1/\sigma_Z * d\sigma/dM$, measured by the CMS experiment [20]. The obtained spectrum and the prediction at NNLO calculations are shown.

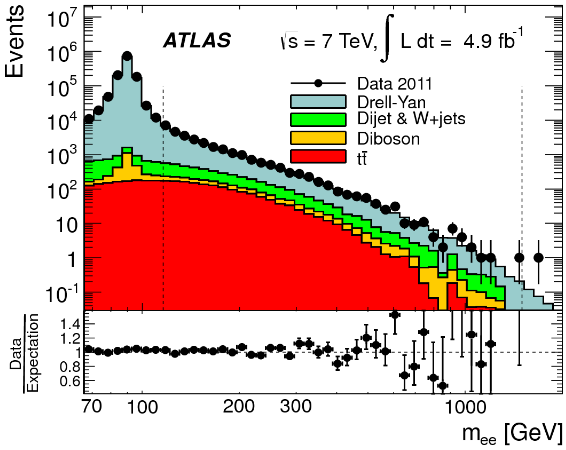

Fig. 1.7: Invariant-mass distribution of electron pairs in data obtained by the ATLAS experiment [23]. The results are compared to the summed signal and background predictions. The Drell-Yan signal is predicted from PYTHIA simulation.

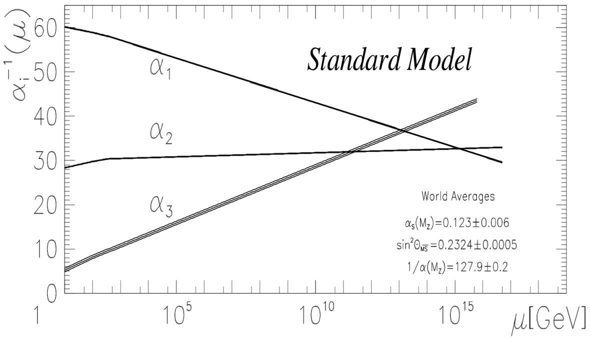

Fig. 1.8: The inverse coupling constants of SM which represent the electromagnetic, weak and the strong couplings, respectively [25].

1.2 Beyond the Standard Model Theories

Although the Standard Model can explain well the electroweak and strong interactions, it is widely believed that it is not the ultimate theory that can explain everything at the fundamental level. Behind this belief, unexplained experimental and cosmological observations lie. For example, the Dark Matter and Dark Energy of the universe, matter-antimatter asymmetry, and the experimentally observed non-zero neutrino masses are not incorporated in the theoretical framework of the SM. Although the gravitational force is very weak at the short range at which QCD and elecroweak interactions occur, the theory can not be complete without gravity included. Solving the hierarchy problem between the low and high energy scale ($m_{EW}/M_{Pl} \sim 10^{-17}$) is another compelling issue.

If we draw the evolution of the values of the coupling constants of the fundamental interactions with the energy scale at which they would apply, there is an energy around which all three coupling constants are nearly but not totally equal, as can be seen in figure 1.8. Grand Unification Theories (GUTs) (see for example [26, 27]) aim to achieve a successful unification of the three gauge coupling constants at the high energy scale around $\Lambda_{GUT} \sim 10^{15}$ GeV. The promising aspect of these theories is that three forces are combined into one coupling constant, corresponding to only one large gauge group which unifies the SM forces. Subsequently, the large group is broken at lower energies to the SM gauge groups.

Grand Unification Theories are promising candidates for physics beyond the SM. Many of these GUTs predict the existence of new particles at the TeV scale, which might be light enough to be accessible at the LHC collider. Also various other theoretical models predict the existence of such extra neutral gauge bosons which are explained briefly in the following sections.

1.2.1 Extra Gauge Bosons: Z′ Models

There is a large literature on this subject where each model describes the different aspects. For simplicity, three classes of extended gauge theories predicting extra neutral gauge bosons can be considered: GUT inspired E6, left-right symmetric models and more generic extension models.

- **Large E_6 Groups:** It is an effective model which originates from the breaking of a larger E_6 group to the SM symmetry [19] as

  $$E_6 \to SO(10) \times U(1)_\psi \to SU(5) \times U(1)_\chi \times U(1)_\psi$$

  The breaking of this group down to the SM symmetry, implies the existence of a gauge boson that is a mixture of two additional neutral gauge bosons:

  $$Z'(\theta) = Z_\psi \cos\theta' + Z_\chi \sin\theta' \tag{1.21}$$

  The mixing angle θ' is usually chosen to be 0 and $\pi/2$, which corresponds to a pure Z_ψ and Z_χ, while the choice of arctan $\sqrt{3/5}$ leads to a Z_η in superstring inspired models.

- **Left-Right Symmetric Models (LRM):** This model is based on the GUT inspired SO(10) group breaking to intermediate symmetries [28], for example

$$\begin{aligned} SO(10) &\to SU(3)_C \times SU(2)_L \times U(1)_Y \times U(1)_\chi \\ &\to SU(3)_C \times SU(2)_L \times SU(2)_R \times U(1)_{B-L} \end{aligned}$$

The first chain of the breaking symmetry leads to the SM Z boson and an additional Z_χ as discussed above, while the second term leads to a right-handed gauge boson and an additional neutral current [28].

- **Generic U′(1) Extension:** The SM can be extended by an extra gauge group. The gauge group of a typical Z′ model predicting a single extra Z′ boson is considered to be

$$SU(3)_C \times SU(2)_L \times U(1)_Y \times U'(1)$$

where the SM is extended by an additional gauge group of U′(1). The U′(1) gauge group could be broken at the TeV scale giving rise to a massive Z′ gauge boson with couplings to SM fermions. In this case it might be possible to detect such a particle at the LHC collider.

In pp colliders, the production cross-section of a Z′ decaying to two muons can be given by [29]

$$\sigma(pp \to Z' \to \mu^+\mu^-) = \frac{\pi}{48s}\left[c_u w_u(s, M_{Z'}^2) + c_d w_d(s, M_{Z'}^2)\right], \tag{1.22}$$

where $w_{u,d}$ are parts of the hadronic structure functions and do not depend any couplings. The coefficients c_u and c_d are given by

$$c_{u,d} = g_z^2(z_q^2 + z_{u,d}^2) \times BR(Z' \to \mu^+\mu^-), \tag{1.23}$$

where g_z is the gauge coupling of $U'(1)$, and z_q and $z_{u,d}$ are the couplings of quarks to Z′ .

A benchmark model used in new vector boson searches is the so-called *Sequential Standard Model (SSM)* or Standard Model like

Z′ model. This model assumes that the Z′ couplings to fermions are the same as those of the Z boson. The model, by itself, is not gauge invariant [28] however it is often used as benchmark signal model in experimental searches because of its simplicity and for the comparison of the experimental results with respect to different signal models being tested.

1.2.2 Extra Dimension Models

There is a number of theories predicting extra space dimensions differing in the number or type (flat or warped):

- **ADD Model:** It is proposed by Arkani-Hamed, Dimopoulos and Davali [30] to solve the hierarchy problem without supersymmetry. The model unites gravity and other interactions at the weak energy scale. The weakness of the gravitational force on distances $\gtrsim$ 1mm is explained by new compact spatial dimensions (≥ 2) larger than the weak scale. The gravitons are allowed to propagate in the extra dimensions while the SM fields are localized in 4-dimensions at the weak scale.

- **Kaluza-Klein Excitations:** The simplest case of Extra Dimension models predict a single extra dimension of a radius R, implying the existence of Kaluza-Klein excitations [31] of the states that can propagate in the bulk[§] with a mass of $\sim n/R$, where n indicates the extra dimensions n = 1,... . If only gravitons are allowed to propagate then it will be possible to probe the graviton experimentally. However, if the SM gauge bosons are also allowed to propagate, R^{-1} should be larger than $\mathcal{O}$(TeV) (R $\lesssim 10^{-17}$ cm).

- **Warped Extra Dimensions:** The Randal-Sundrum (RS) models predict warped extra dimensions [32]. The SM fields are localized in the brane. The RS gravitons (G) are predicted in the mode of G^n: the lightest graviton is massless and mediates the

---

[§] Bulk is a hypothetical hyper-dimensional space that can include surfaces called branes. Our four-dimensional universe is assumed to be on a brane in the bulk.

gravity. The rest of the modes are massive resonances. There are two parameters left free in the model. They are the mass of the graviton and k/M_{Pl}, where k is the coupling constant and M_{Pl} is the Planck Mass $\sim 10^{18}$ GeV where gravity becomes as strong as the gauge interactions.

The mass and the width of the n'th resonance is given by

$$m_n = x_n k e^{-k\pi R}, \ \Gamma^n = \rho m_n x_n \left(\frac{k}{M_{Pl}}\right),$$

where ρ is a constant and depends on the open decay channel modes and x_n is the n-th Bessel function. The main processes producing the graviton resonances are $q\bar{q} \rightarrow G^n$ and $gg \rightarrow G^n$. The graviton can decay to $l^+l^-, \gamma\gamma, q\bar{q}, gg$. The lightest graviton resonances may be accessible at the LHC colliding energies.

1.2.3 Observables Sensitive to BSM Signals

At hadron colliders, the direct production of a Z′ (or a graviton resonance) can be probed in the decay channels to fermion pairs. The most promising channel for the search is $pp \rightarrow Z' \rightarrow l^+l^-$, in which Drell-Yan production will be the dominant background as it gives the same final state. The decay to quark-antiquark will suffer from the extremely high background arising from di-jet production in QCD processes, thus lowering the sensitivity of an experimental search. The expected model parameters which can be used as observables, in the same time assuming that a resonance is found the first measurements to be performed, are the total cross section times the branching fraction of the leptonic decay channel, total width of the resonance, the spin, the parity and the forward-background asymmetry.

As a starting point, in case an excessive number of events is observed anywhere in the invariant mass spectrum of lepton pairs, the *cross-section times branching fraction* ($\sigma_{Z'} \times BR$) for a given Z′ model can be measured by counting the excessive number of events with the measured invariant mass around the resonance mass ($M_{Z'}$). The *total width* ($\Gamma_{Z'}$)

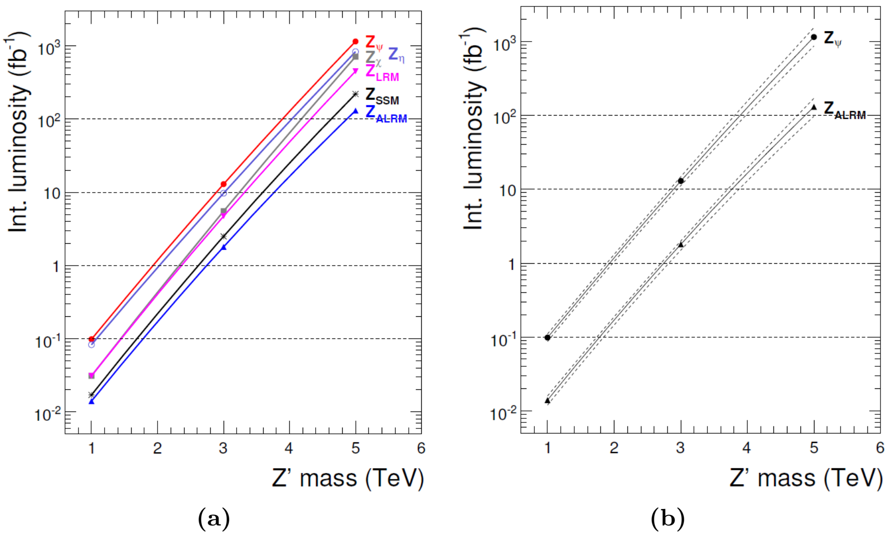

Fig. 1.9: The integrated luminosity to reach the 5σ discovery for various GUT inspired Z' models as a function of Z' mass in the di-muon channel shown in (a). The same reach for Z_Ψ and Z_{ALRM} models predicted with ±1σ theoretical errors bands are shown in (b) [33].

of the resonance can be measured as well by fitting the invariant mass distribution around $M_{Z'}$. In case of an absence of signal events (if no resonance is observed), the cross section times branching fraction can be constrained for the considered benchmark Z′ models.

Assuming the narrow-width approximation of the Z′ leptonic decays, where the detector resolution dominates the mass resolution and the production cross section defined by equation 1.22, can be considered, in which the production of the Z′ depends on the Z′ mass together with the two other parameters c_u and c_d. These parameters can be determined or constrained via experimental measurements.

Another observable sensitive to a Z′ signal is the *forward-backward asymmetry* (A^l_{FB}) of produced lepton pairs which can be used to distinguish between the Z′ models. As advocated in reference [34] the *rapidity dis-*

tribution (Y_{ll}) of lepton pairs might also provide extra information on the couplings of Z′ which might help to separate the benchmark models used to test. It should be noted that the maximum sensitivity can be achieved by using all or as many possible observables together.

1.3 Experimental Searches for High Mass Resonances

Evidence for the production of mentioned particles, arising in the theories beyond the Standard Model, has been searched for long at the Tevatron experiments CDF [35] and D0 [36], as well as the LHC experiments. The searches for such extra particles are mostly conducted as direct searches for a "resonance bump" in the di-lepton invariant mass spectrum, which would appear on top of the smooth background mostly given by the production of the Drell-Yan process. Figure 1.9 shows the discovery potential of CMS, where such peak-search approach is adopted, for various Z′ models in the di-muon channel at the design luminosity and collision energy.

No significant deviations in the observations from the Standard Model predictions have been found so far. Figure 1.10 shows the upper limits on the cross-section×branching ratio set by the ATLAS experiment [37, 38] for GUT inspired E6 models and the sequential standard model at 7 TeV collision data in di-muon and combined lepton channels, respectively. Figure 1.11 shows the invariant mass distribution of di-muon events obtained by the CMS experiment [39, 40], which is also compatible with the expectations from the standard model processes. In this case, upper limits (at 95% CL) were set on the ratio of the production cross-section×branching fraction of some Z′ models to that of the Z boson which is shown is figure 1.12. The lower limit (at 95% CL) on the mass of the sequential standard model Z′ , resulting from the search in the di-muon channel, is nearly 2.8 TeV/c^2. The current mass limits set by LHC experiments are the most stringent limits up to date.

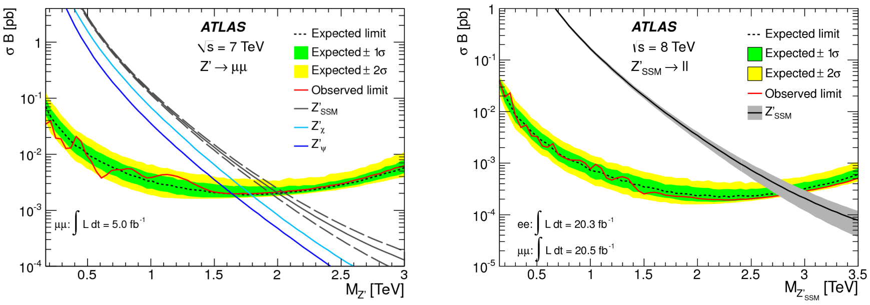

(a) (b)

Fig. 1.10: Upper limits at 95% CL on $\sigma \times$BR performed by the ATLAS experiment [37, 38] (a) for Z'_{SSM} and the two E6-motivated Z' models in the di-muon channel with 7 TeV collision data and (b) for Z' SSM production for the di-muon and di-electron channels combined with 8 TeV collision data.

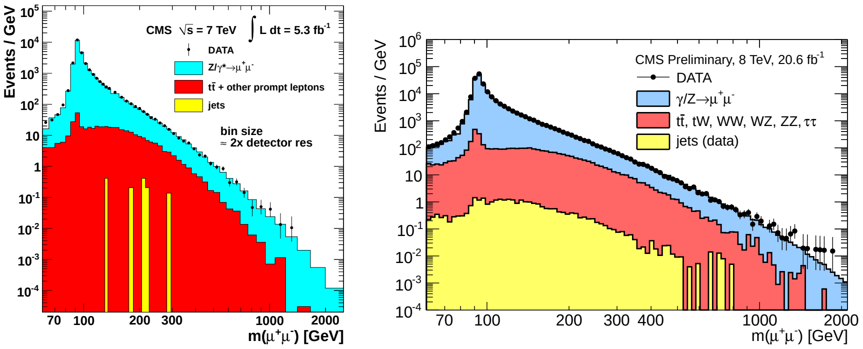

(a) (b)

Fig. 1.11: The invariant mass spectrum of dimuon events performed by the CMS experiment [39, 40] (a) at 7 TeV and (b) at 8 TeV collision data.

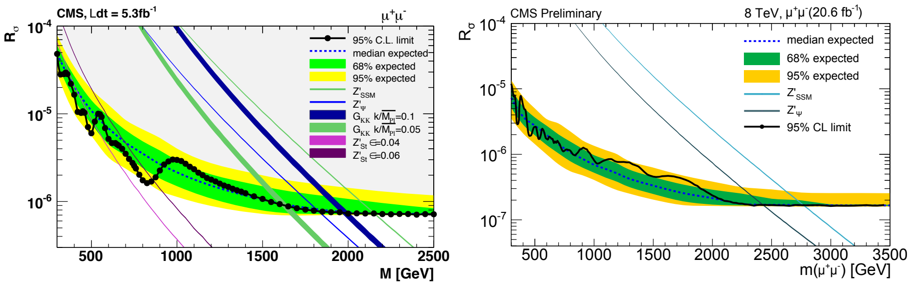

(a) **(b)**

Fig. 1.12: Upper limits on the production ratio R_σ of cross section times branching fraction into lepton pairs for various BSM signal production relative to the Z bosons by the CMS experiment [39, 40] (a) at 7 TeV and (b) at 8 TeV collision data.

1.4 Motivation of the Research

The di-muon final state is experimentally advantageous to study. It is a relatively clean final state and represents a clean signature in the detector. Therefore, these types of events are ideal for discovering BSM signatures in high energy physics experiments.

The current CMS analysis in which only the distribution of the invariant mass of di-muon events is used, does not show any significant evidence for new phenomena. A more powerful method could help increasing the sensitivity of this search. Our aim is to improve the analysis methods in terms of the sensitivity of the detection of a possible BSM signal, as well as the performance of the reconstruction techniques used.

We investigate the use of a "Matrix Element Method" to search for a heavy resonance in the di-muon final state. Instead of the invariant mass of di-muon events as used by peak-search approaches, the full event kinematic information which contains all the measured particles and their measured properties in the event is used as observables in the analysis. Throughout the thesis, in order to be sensitive to a large group of theoretical models predicting new resonances, the narrow width approximation is used. This means that the natural width of the resonance is assumed to be significantly smaller than the experimental mass resolution of the experiment. Furthermore, a spin-1 hypothesis is considered for the Sequential Z' model, as the main benchmark model to test. A possible sensitivity gain in the analysis will be very useful for current and future searches for heavy resonances which are predicted by various theoretical models, as few of them briefly described in this chapter.

This thesis will also describe a new technique to measure from data the amount of material encountered by particles produced at the collision point. The knowledge of this amount of material is one of the fundamental ingredients of the measurement of the particle momentum with tracking detectors.

Chapter 2

The CMS Experiment at the LHC

2.1 The LHC Project

The Large Hadron Collider (LHC) at CERN is the world's most powerful particle accelerator among the high energy particle physics collider machines. Based on superconducting technology, it accelerates particles in a circle of 27km underground and is designed to collide proton beams at the center of mass energy of up to 14 TeV with a target luminosity of $10^{34} cm^{-2} s^{-1}$. It can also collide heavy lead (Pb) ions up to 2.8 TeV. The aim of the project is to prove the existence of SM Higgs particle and reveal physics beyond the SM by testing the current understanding of nature at the high energy frontiers. LHC has two high general purpose detectors called ATLAS and CMS.

2.2 The CMS Detector

The Compact Muon Solenoid (CMS) is a multi-purpose operating detector at the LHC at CERN. It is constructed at one of the interacting points of the proton beams at the collider. One of the main features

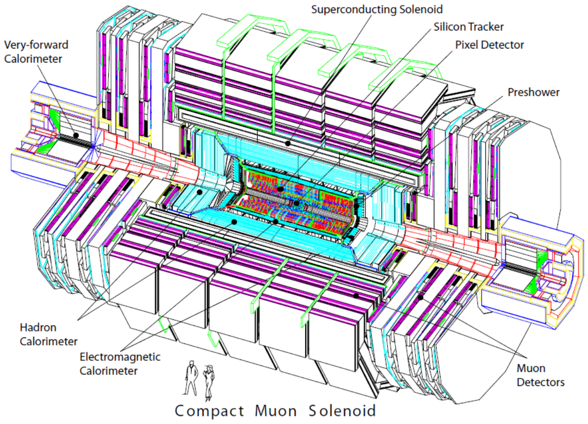

Fig. 2.1: Overall schematic view of CMS detector.

of the CMS detector is a superconducting solenoid providing a high magnetic field up to around 4T providing a large bending power for the reconstruction of muon momentum. Overall schematic view of the CMS detector is shown in figure 2.1 [15]. From in to out of the detector respectively, the pixel and silicon detector for the tracking system, the pre-shower and the electromagnetic calorimeter can be seen. Then the hadronic calorimeter is placed. After the magnet, the muon system covers the barrel and the endcap of the detector.

The CMS detector requirements to accomplish the physics programme are good muon identification and muon momentum resolution together with good track reconstruction for charged particles in the inner tracking system. A good electromagnetic energy resolution in the reconstruction of photon and electrons, good jet reconstruction, an accurate missing transverse energy reconstruction and the overall geometric coverage are the key factors of the detector design.

The total proton-proton cross section at $\sqrt{s}$ =14 TeV is expected to be roughly 100 mb. At the design luminosity the general purpose detectors will provide around 10^9 inelastic scattering events/s [15]. This leads to an incredible experimental challenge of selecting the "interesting" events among all collisions. The large flux of particles coming from the interaction point requires high granularity and good detector response in time.

The coordinate system of CMS is centered at the collision point. The y-axis is vertically pointing upward and x-axis is pointing to the center of the LHC. Hence, the z-axis lies along the beam direction. The azimuthal ϕ angle is measured from the x-axis in x-y plane. The polar angle θ is measured from the z-axis in z-y plane. The pesudorapidity is defined as $\eta = -lntan(\theta/2)$. By the definition of the coordinate system, the momentum of the charged particles are measured in the vertical plane transverse to beam direction denoted as p_T. The other components of the physical quantities can be measured kinematically.

Particle identification is a crucial part of the building an experiment. It plays a main role in the structure and the geometry of the detector design. Depending on the physics goals to achieve, different layout for the detector can be chosen in order to have the optimal performance on the type of particles to be reconstructed with the detector system. There are different techniques used in the calorimetry as well as the tracking. Although the technology used can be different in the detectors, the main principles are the underlying psychics processes which affect the performance of the detector. The calorimeters measure the energy deposited by the traversing particle due to the generated electromagnetic and hadronic showers. The main principle of tracking is the curving the path of the electrically charged particle with a strong magnetic field so that calculation of the curvature will allow to measure the particle's momentum.

2.3 The CMS Superconducting Magnet

The superconducting solenoid magnet is one of the distinctive features of the CMS detector. It has two main components: one is the coil solenoid and the other part is the return yoke. To accomplish the good measurement of the muon momentum resolution and an efficient inner tracking, a strong bending power and therefore a strong magnetic field is necessary. The CMS coil solenoid is 13m in length and 5.9m in diameter and allows a muon detection up to 2.4 in η [41]. The 4T magnetic field is an optimal choice to enable a good inner tracking. The occupancy of the outer tracker in the barrel is reduced by the strong field. This also reduces the flux of charged particles reaching to the electromagnetic calorimeter.

The magnetic flux is returned by an iron yoke. The CMS iron yoke in designed to saturate the magnetic flux generated by the magnet coil. It is composed of 6 disks and 5 barrel wheels. The muon chambers are interleaved between the iron plates of the yoke. The thick iron yoke allows not only good muon identification by absorbing the hadrons, but also helps fast triggering.

2.4 The CMS Tracking System and Track Reconstruction

2.4.1 Tracker Layout

The CMS tracking system is designed to provide a precise measurement of trajectories of charged particles. It covers the interaction point, the center of CMS and extends to a length of 5.8m and a 2.5m in diameter. In order to measure the charged tracks accurately at the nominal luminosity, the tracking system is built with high granularity and fast response to differentiate each bunch crossing. However, the technologies used in the tracking system pay off with the requirement of powerful cooling and electronic systems. The amount of material required for optimal operation of detector, placed within the tracking system, will directly affect the amount of interactions with the detector material. Therefore, the chances of a deteriorated, inaccurate measurement of trajectories will be increased.

The requirements of the detector having high granularity, fast response and radiation hardness makes the choice of the tracking system being made out of silicon. The tracking system consists of inner pixel and outer silicon detection layers. The pixel detector is made out of three barrel layers and two endcap disks. The silicon strip tracker is composed

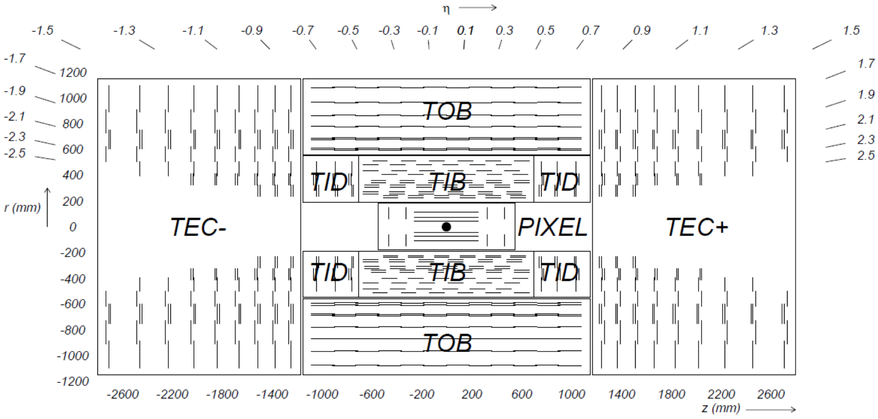

Fig. 2.2: Schematic drawing of the CMS tracking system where each line represents the detection modules.

of 10 layers in the barrel 3 plus 9 disks in the endcap region of detector. The acceptance of tracking system extends up to $|\eta| < 2.5$. Figure 2.2 shows the schematic view of the CMS tracking system. The single lines represent the single modules while double lines represent the detection modules providing stereo hits.

The inner pixel tracking system surrounds the CMS interaction point at a very close radius of 4.4 to 7.3 cm and 10.2 cm in cylindrical layers along the beam pipe. The silicon tracking system has different subsystems called Tracker Inner Barrel (TIB), Tracker Outer Barrel (TOB) and Inner Disks (TID) and Endcap (TEC). The tracker has a complete symmetrical view with respect to the x-y plane of the CMS detector.

The pixel detector delivers high precision space-points with resolutions of 15-20 μm. The first two layers of TIB and TOB and the first two disk of TID as well as 1,2 and 5 disks of TEC are mounted with second layers of detector modules to improve the detector resolution. The strip pitch is 80 μm on layers 1 and 2 and 120 μm on layers 3 and 4 in the TIB, leading to a single point resolution of 23 μm and 35 μm, respectively. Outer barrel of tracker (TOB) provides 6 measurements with single point resolution of 53μm (in the first 4 layers) and 35 μm (in layers 5 and 6), respectively. In addition, the modules in the first two layers and rings, respectively, of TIB, TID, and TOB as well as rings 1, 2, and 5 of the TECs carry a second micro-strip detector module which is mounted back-to-back with a stereo angle of 100 mrad in order to provide a measurement of the second coordinate (z in the barrel and r on the disks). The tracker assembly ensures approximately 9 hits in the range of $\eta < 2.4$ in the silicon strip tracker while providing more hits in the transition region of barrel-endcap.

2.4.2 Track Reconstruction and Performance

The main principle of track reconstruction is based on the idea of building a trajectory of particle using digitized hits (clustered signals) in the electronic readout, given detector set-ups. The track reconstruction is performed by the reconstruction algorithms implemented in the CMS software framework called CMSSW [42]. The CMS standard track reconstruction algorithm is performed by the combinatorial track finder (CTF) [43] in a number of iterations providing the final track parameters and corresponding uncertainties in the form of a 5×5 covariance matrix. Parameters describing a track are chosen to be d_0, z_0, ϕ, $\cot\theta$ and the transverse momentum p_T. These parameters are defined at the point of closest approach to the beam axis where d_0 and z_0 define the coordinate of the impact point in the transverse and longitudinal directions, ϕ and θ are the azimuthal angle and θ the polar angle, respectively.

The track reconstruction is performed in many steps. These steps can be summarized briefly as following;

- **Local reconstruction**: It starts from clustering signals recorded on individual electronic channels as a result of the passage of charged particle in the silicon and pixel detectors. For each of these clusters a 2 dimensional position of the crossing point and the associated uncertainty are estimated.
- **Seed generation**: Initial “seeds”, which are estimate of the track parameters (particle momentum and position) and associated uncertainties, is provided at this step either externally (from the

muon system for example) or internally from the innermost tracking layers. In the latter case seeds are constructed out of either triplets of hits in the tracker or pairs of hits with an additional constraint from the beamspot or a pixel vertex.

- **Pattern recognition**: Starting from a seed provided, additional hits from the various detection layers of the detector and compatible with the trajectory of a charged particle, are added to the candidate track. To explain briefly: the seed is propagated outward, to the next detection layer where compatible hits are searched for. As a compatible hit is found, its spatial information is added to update the track parameters and the uncertainties. This search continues until either the boundary of the tracker is reached or no more compatible hits are found. If more than a compatible hit is found, as many track candidates are created and the procedure is continued for each of them.

- **Final track fitting**: Having associated a set of hits to a track candidate, a final fit is performed with the aim of obtaining an estimate of the track parameters and their uncertainties at every detection layer and at the interaction vertex. These estimates are obtained by reproducing the procedure outlined in the previous step in the inward direction. At every detection layer the outward and inward states are weighted averaged to obtain the final estimate of the track parameters and uncertainties at the considered detection layer (or at the interaction point). Such a weighted average is proved to be mathematically equivalent to a full χ^2 global fit to all measured positions using a model that includes the particle energy loss, the deflection in the magnetic field and the change in trajectory resulting from the interactions with the detector materials. This alternative equivalent procedure is called the Kalman Filter [44].

- **Track selection**: After applying the final quality cuts, fake tracks are removed. Fake tracks are identified as those that share a large number of hits with other candidates and/or that have a very large fit χ^2.

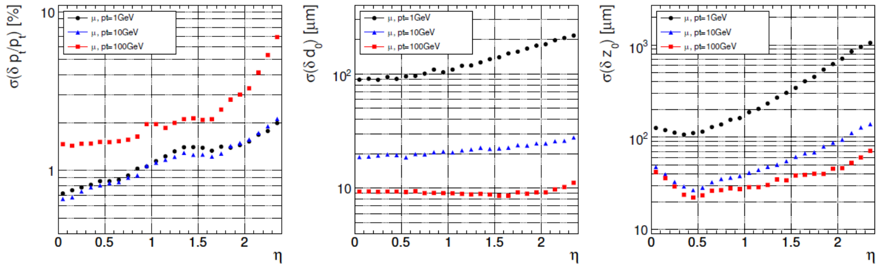

Fig. 2.3: The resolution of track parameters for single muon tracks having 1, 10 and 100 GeV/c of transverse momentum. The resolution of transverse momentum (left), transverse impact parameter (middle), longitudinal impact parameter (right) are shown as a function of η [45].

For muons having a transverse momentum between 1 and 100 GeV/c the tracking efficiency is higher than 99% in the full coverage of the tracker. Figure 2.3 shows the expected resolution of muon tracks having 1, 10 and 100GeV of transverse momentum [45].

2.5 The CMS Muon System and Muon Reconstruction

2.5.1 Overview of the Muon System

Muon reconstruction plays a central role in the CMS detector as it appears in the middle of the experiment name. Good muon momentum measurement is a crucial part of many Standard Model measurements and the searches for BSM physics which involves muons in the final state, for example the measurement of the properties of Higgs particle in the four lepton final state, for H decaying to ZZ, then decaying to leptons. The proper identification and the accurate measurement of muons can lead to a potential discovery of BSM physics. The CMS detector has the aim of a good muon momentum measurement and muon identification as well as fast muon triggering.

The muon system of CMS naturally follows the cylindrical shape of the coil solenoid. Three types of gaseous muon detection systems are mounted on CMS. These are;

- **Drift Tube (DT) Chambers**: Standard rectangular shape DTs are mounted mostly in the barrel region where the neutron induced background is small. They cover a pseudorapidity region of $|\eta|$ <1.2 and consist of 4 layers of stations. The DT system is designed to measure muon position in r-ϕ plane and z direction. Figure 2.4 shows the layout of the CMS DT muon system in the vertical plane [45].
- **Cathode Strip Chambers (CSC)**: The endcap region of the muon system between $|\eta|$ 0.9 and 2.4 is equipped with fast response cathode strip chambers. These detector region is expected to have a high hit occupancy during the LHC data taking which are mostly due to beam radiation (photons and neutrons). The 4 stations of cathode strip chambers in the endcap run radially to provide a measurement in r-ϕ.
- **Resistive Plate Chambers (RPC)**: In order to provide redundancy both at the trigger and offline level, the barrel and endcap muon system are equipped with another complementary system consisting of resistive plate chambers. RPCs provide a fast time response and resolution with a large coverage in the rapidity range of $|\eta|$ <1.6.

  Apart from the muon subsystems, a sophisticated optical alignment system measures the muon sub-detector positions with respect to each other and to the inner tracker to optimize the momentum resolution.

The different technologies used in the CMS detector makes the detector to be divided in tree regions:the barrel, which covers $|\eta|$ <0.9, the overlap or transition region in 0.9< $|\eta|$ <1.2, and the endcap region of detector, which covers 1.2< $|\eta|$ <2.4. In figure 2.5 overall layout of one quarter of the CMS detector is shown, together with muon system [46]. The

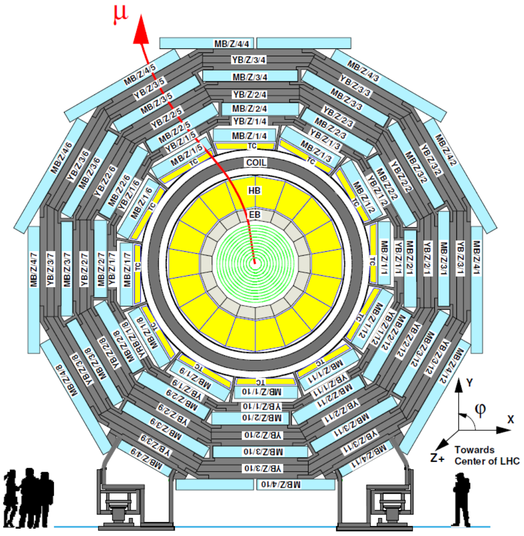

Fig. 2.4: The vertical layout of the CMS barrel muon DT chambers in one of the 5 wheels [45]. A representative trajectory of a muon is drawn as well.

motivation of the geometrical division of the detector regions can be clearly seen.

2.5.2 Muon Reconstruction

The efficiency of reconstruction of charged muon tracks is high with the CMS detector. Energy loss of muons in the silicon tracker is mostly through ionization. Their energy loss via Bremsstrahlung is generally negligible at low momentum. However, it becomes important for muons produced with an initial energy higher than 100 GeV. Multiple Coulomb scattering with the nuclei of the detector material is the main responsible for deflections in the trajectory of charged particles. The effect of multiple scattering is fully included during the pattern recognition in the Kalman filter.

The CMS muon reconstruction is based on combination tracks reconstructed separately in the inner tracker and outer muon system. Tracks

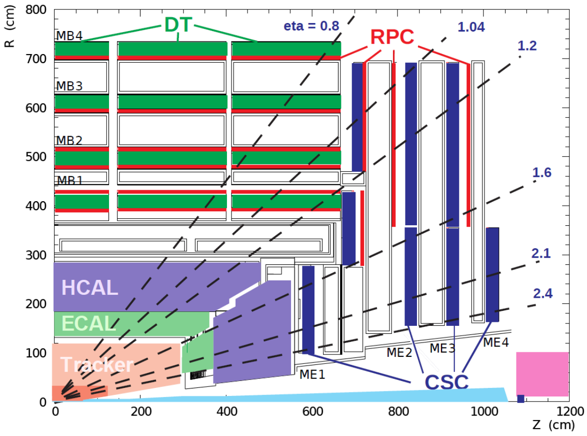

Fig. 2.5: The overall layout of one quarter of the CMS detector with the barrel and endcap muon system shown [46].

are thus reconstructed separately in the tracker and muon system. The full reconstruction can be divided in these parts:

1. **Tracker Muon Reconstruction (inside-out)**: All tracker tracks with p_T >0.5GeV/c and having a total momentum greater than 2.5 GeV are considered as possible muon candidates. The track parameters are extrapolated to the muon system taking into account the effects of the detector set-up. If at least one muon segment is found to match the extrapolated track then the track is identified as a “tracker track” [46].

3. **Standalone Muon Reconstruction**: A track reconstructed with information from just the muon detectors is called “standalone muon track”.

2. **Global Muon Reconstruction (outside-in)**: A “global muon” is the result of fitting the hits belonging to a track reconstructed in the inner tracker and those associated with a standalone muon. The two tracks must be compatible with the trajectory of a single particle. The global track reconstruction can help to improve the reconstruction of muon tracks with a p_T higher than 200GeV/c by using the more precise information from tracker system.

> Most of the times the muons having sufficiently high momentum are reconstructed either as tracker track or global muon or both. If both reconstruction algorithms fail then the muon track is reconstructed as Standalone Muon. 1% of the collision muons are reconstructed standalone only [47].

The default muon momentum assignment in CMS uses the following algorithm, called "sigma-switch". The algorithm uses the momentum measured by the global muon reconstruction if p_T >200 GeV/c and the charge to momentum ratio agrees within 2σ with the momentum measurement of the tracker-only reconstruction. In other cases the tracker-only reconstruction is chosen.

The resolution of the momentum measurements for muons in the transverse momentum region below 200 GeV/c is dominated by the measurements from the inner tracker. At high-p_T the extended fit with the muon system is used to improve the resolution.

2.5.3 Muon Identification

In order to identify muons with high efficiency and purity, different criterias are applied on the reconstructed muon tracks:

Soft Muon Identification: A Tracker Track is required to fulfill a certain criteria when matching to a muon segment in x and y coordinates. The soft muon selection is mostly used in the analyses where low-momentum tracks are required.

Tight Muon Identification: The muon track should be reconstructed by the global muon reconstruction algorithm by requiring the $\chi^2/d.o.f$ of the fitted track to be less than 10. At least one muon chamber hit should be used in the muon reconstruction. Additionally, the muon track should be recontracted as a tracker track which matches to two hits in the muon stations. More than 10 tracker hits including at least one from pixel should be used in the Tracker Track. The transverse impact parameter of track with respect to the primary vertex should be less than 2mm.

Particle-Flow Muon Identification: This identification algorithm is based on the so-called the particle-flow algorithm [48], which uses information from the all detector systems of the experiment to identify all the particles. Starting from these particles, higher-level reconstructed quantities, like jets, missing transverse energy and tau-jets are also identified. The particle-flow muon identification identifies on one side isolated muons and on the other muons in jets.

2.5.4 Performance of the CMS Muon Reconstruction

The muon reconstruction and identification efficiencies are studied by CMS with a tag-and-probe technique [49] for the high and low-p_T momentum region using J/Ψ and Z decays to di-muons. Figure 2.6 shows the muon identification efficiencies for the barrel (upper) and endcap (lower) regions of the detector with different identification algorithms. As muon momentum increases, identification efficiency approaches a plateau close to 100%. The muons identified as tight muons in general have an efficiency of more than 96% for p_T above 20 GeV/c. The dependency of the plateau efficiency on the pseudorapidity of muon is shown in figure 2.7 for muons having a p_T >20GeV using a tag-probe-method with Z→ $\mu^+\mu^-$ events.

Figure 2.8 shows the invariant mass distribution of di-muon events for low-mass values [46]. The low-mass di-muon resonances are clearly separated.

2.5.5 High-p$_T$ Muon Reconstruction Algorithms

The accuracy of the muon momentum measurement can significantly worsen for the high momentum muons. The radiative energy loss occurring mostly in the calorimeters and in the return yoke is not negligible. The radiative process can give rise to the electromagnetic showers in the muon system and therefore increase the number of hits in the muon chambers. Moreover radiative energy losses are not taken into account in the track fit. Because of these effects muon momentum measurement

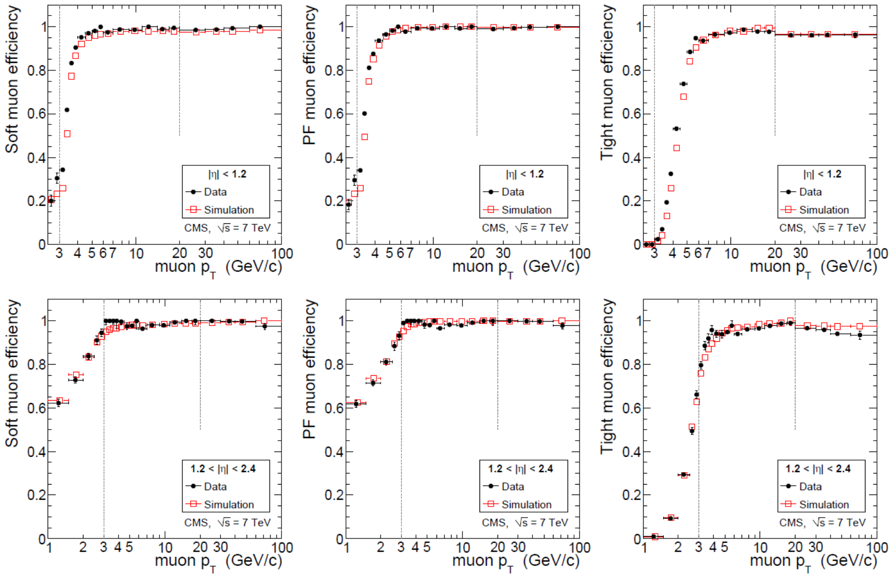

Fig. 2.6: Muon identification efficiencies obtained for data in comparison to simulation with a tag-and-probe method as a function of the reconstructed muon-p_T . The efficiency of Soft Muons (left), PF muons (middle) and Tight Muons (right) are shown with respect to barrel and overlap (upper) and endcap (lower) region of the detector [49].

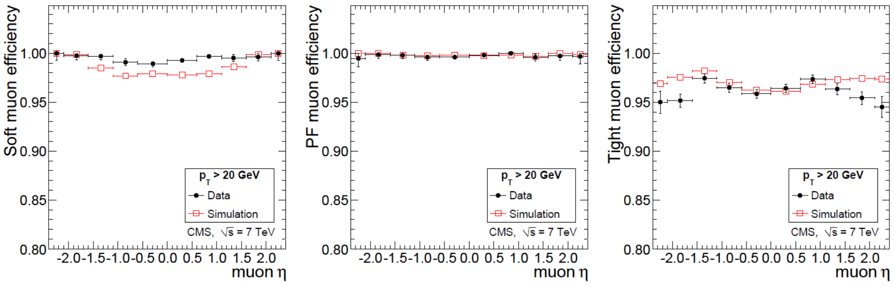

Fig. 2.7: Muon identification efficiencies relative to the tracker track obtained with a tag-and-probe method as a function of the pseudorapidity of muon. The efficiency of Soft Muons (left), PF muons (middle) and Tight Muons (right) are shown [49].

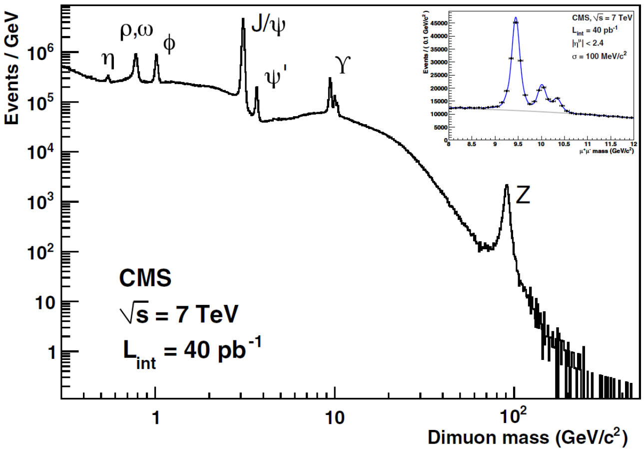

Fig. 2.8: Invariant mass distribution of di-muon events collected by the CMS detector during the 2010 Runs. A good mass resolution on Υ^* can be seen clearly [46].

described in the previous sections can be significantly biased. Therefore special algorithms are used for measuring the high momentum muon tracks.

- Tracker-Plus-First-Muon-Station (TPFMS): This algorithm refits the global-muon track with just the innermost muon chamber ignoring all other hits produced in the muon system.
- The Picky Fit: The algorithm uses the hits in the global-muon track and refits the track using only hits in the muon chambers that are compatible with the extrapolated trajectory in order to reduce bias using extra hits contaminated by the showers.
- Tune-P: This algorithm is also called “Cocktail” and uses the combination of the above fits to improve the momentum assignment of tracks. It takes the measurement associated with the track with the lowest χ^2. In high-p_T muon reconstruction usually Picky or TPFMS algorithms are chosen for the momentum assignments.

Cosmic muons are used to determine the performance of the detector for the high-p_T momentum range by CMS [46]. Figure 2.9 shows the result

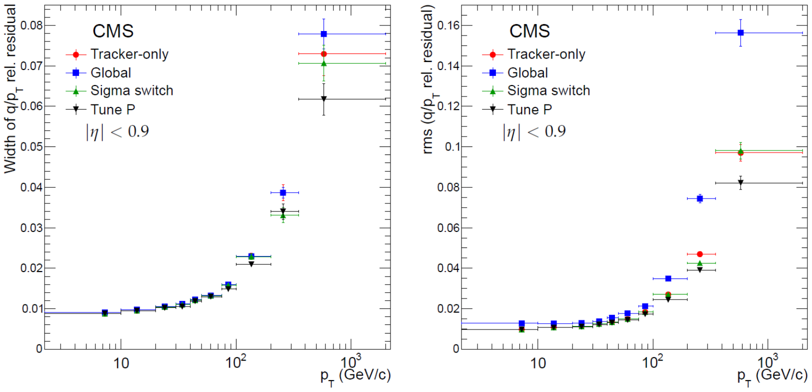

Fig. 2.9: The results of the momentum resolution performance by the CMS experiment [46]. The figure on the left shows the width of q/p_T relative residuals according to various fitting algorithms, while the figure on the right shows the RMS of the same distributions.

of the measured performance. The figure shows the relative resolution measured with different fitting algorithms, for the tracker-only, global, sigma-switch and the Tune-P, respectively. The best performance is obtained from Tune-P algorithm which fits the 350< p_T <2000 GeV/c transverse momentum region with a 6.2% in the resolution. Therefore the physics analyses performed with high-p_T muons require final track parameters provided by the Tune-P algorithm.

Chapter 3

Measurements of the CMS Inner Tracker Material

As described in chapter 2, the material in the detector is necessary for the detection of the particles coming from the colliding protons. On the other hand, the interactions with the sensitive or passive detector material can deteriorate the resolution of the track momentum measurement. In any case the knowledge of the distribution of material within a tracking detector is a fundamental ingredient for the measurement of the momentum of charged tracks based on the bending of the trajectory in a magnetic field. In this chapter, after describing the interactions of traversing particles with the detector material, we present a novel technique to measure the distribution of the material in the inner tracker volume, using the reconstructed particle tracks. The description of this new method will be followed by the presentation of the results obtained with collision data on the inner tracker of the CMS detector.

3.1 Interactions of Particles with Detector Material

The particles that traverse the detector material can undergo a number of interactions. Charged particles will lose their energy by elastic electromagnetic (or Coulomb) scattering with the electrons of the traversed media, also referred to as ionization energy loss, they can also be scattered via the same interaction by the nuclei of the atoms constituting the detector material. This latter interaction, commonly referred to as multiple scattering, results in negligible energy loss, but in significant changes in the particle trajectory. Hadrons can experience in addition nuclear interactions, in which case the initial particle is lost while a number of secondary particles will emerge from the interaction point.

Let us describe in detail the main processes that can occur while muons traverse the detector medium.

Ionization Energy Loss: The ionization energy loss of muons and any other charged particles heavier than the electron when traveling through material is given by the "Bethe" formula [17] that provides the mean energy loss in a unit material length (MeV/ g^{-1} cm^2) as:

$$-\left\langle \frac{dE}{dx} \right\rangle = Kz^2 \frac{Z}{A} \frac{1}{\beta^2} \left[\frac{1}{2} ln \frac{2m_e c^2 \beta^2 \gamma^2 T_{max}}{I^2} - \beta^2 - \frac{\delta(\beta\gamma)}{2} \right]. \quad (3.1)$$

Here, Z is the atomic number of the absorber material, A is the atomic mass of the absorber, $\delta(\beta\gamma)$ is the density effect correction to the ionization energy loss, $m_e \times c^2$ is the electron mass times speed of light squared. The term T_{max} describes maximum kinetic energy that can free a electron in a single collision, and I is mean excitation energy.

In figure 3.1, the mean energy loss as a function of the muon momentum is shown. Note that as the muon momentum increases beyond several hundreds of GeV, the radiative losses become the more dominant processes.

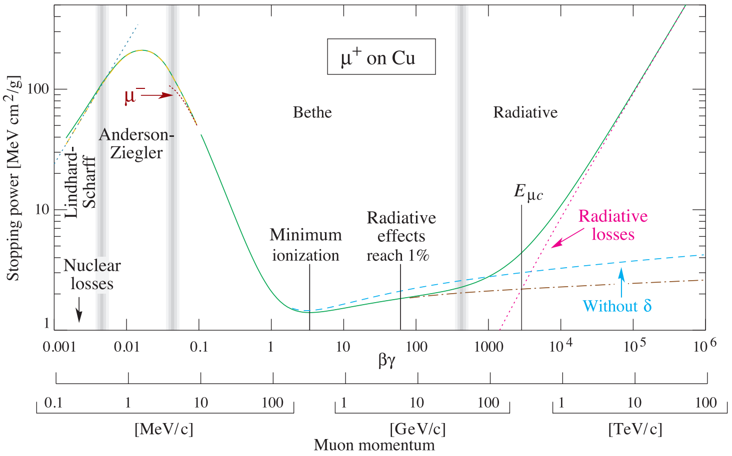

Fig. 3.1: Stopping power for positive muons in copper as a function of the muon momentum [17].

Multiple Coulomb Scattering: A charged particle traversing a material is deflected due to Coulomb scattering from nuclei. Figure 3.2 illustrates the scattering of a particle from a single layer. The projected angular distribution of the scattering is approximately Gaussian with a standard deviation θ_0, given by [17]

$$\theta_0 = \frac{13.6MeV}{\beta cp} z\sqrt{x/X_0}\,(1 + 0.038\ln(x/X_0))\,, \tag{3.2}$$

where p is the momentum, βc velocity and z is the charge number of the incident particles. In the equation, x/X_0 is the material thickness in radiation length units. Radiation length is the scale length for describing high-energy electromagnetic cascades in the longitudinal direction. It is the mean distance over which a high-energy electron losses all but $1/e$ of its energy in a given material.

In case of a particle traversing multiple layers of material or the mixtures of them, it is found to be more accurate if equation 3.2 is applied for total material, once x and X_0 are known for overall thickness [17].

Radiative Losses at High Energy: At sufficiently high energy the radiative processes become dominant over ionization. For muons travers-

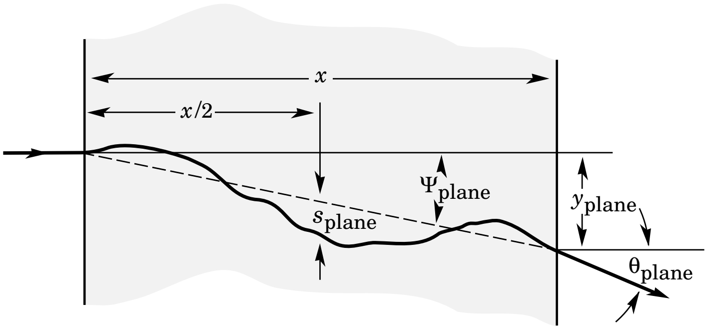

Fig. 3.2: Schematic view of the multiple scattering for an incident particle on the plane. Related parameters are shown as well.

ing iron, for example, this limit occurs at several hundreds GeV. These processes are characterized by small cross sections, hard spectra, large energy fluctuations, and the associated generation of electromagnetic and (in the case of photonuclear interactions) hadronic showers [17].

Figure 3.3 shows the average energy loss of muons in different materials. Each line shows energy loss due to processes like Bremsstrahlung, electron-positron direct production or photonuclear interactions. Energy loss due to ionization in iron is shown as well. It should be noted that an optimal choice of detector material is necessary to limit the multiple scattering, Bremsstrahlung, electron-positron direct production and nuclear interactions in order to limit to the maximum possible extent perturbations to the particle trajectories due to detector material.

3.2 Material Effects in Track Reconstruction

An efficient and precise momentum reconstruction of charged particles produced in the collision is necessary to improve the accuracy of experimental measurements. During the reconstruction of events, the knowledge of the material effects must be used. Inaccurate knowledge of the material description can bias measurements of the energy and direction of the particles and therefore can change the reconstructed event topology, since the events used in the analysis are built from the reconstructed

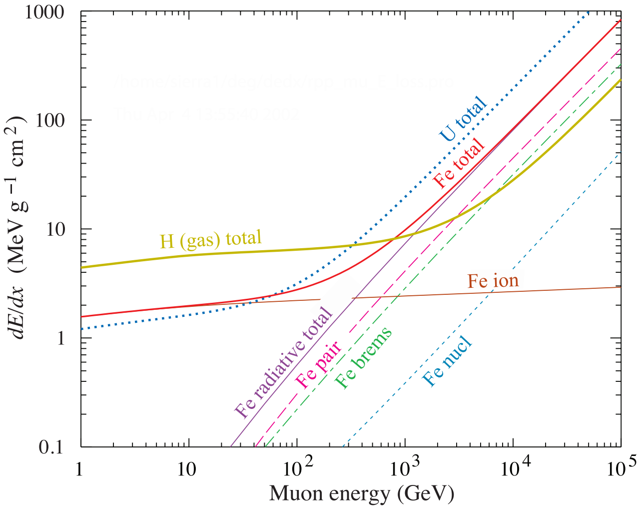

Fig. 3.3: The average energy loss of a muon in hydrogen, iron, and uranium as a function of the muon energy [17].

particles.

When simulating events, the detector effects must be taken into account as well. An adequate simulation of all these effects requires the accurate description of the material knowledge. CMS uses Geant4 [50] detector simulation to take all these effects into account during the propagation of particles in the detector volume. In figure 3.4, the material distribution (material budget) in the inner CMS tracker detector, as assumed in the simulation, is shown in units of radiation length. A simplified version of this material distribution is assumed in the software algorithms that perform track reconstruction.

Indeed, because of the high occupancy in the tracker detector and because of the many combinations of hits that must be checked against the hypothesis of having been generated from the same particle, the track reconstruction would be computationally highly time consuming, even significantly higher than the full simulation of events in the detector. For these reasons, unlike in the simulation of particle propagation in the detection volume with Geant4, for reconstruction, the detailed distribution of the detector material is replaced by a simplified model. The

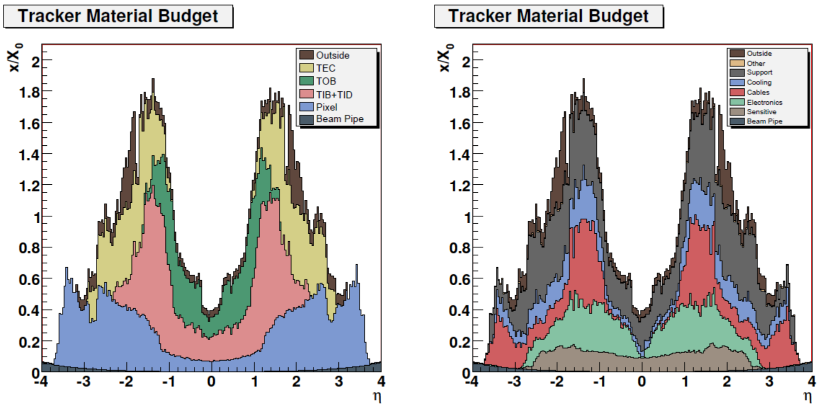

Fig. 3.4: The material distribution of the CMS tracker in units of radiation length as a function of pseudorapidity [51].

model attributes all the materiel existing between two detection layers, only to the (assumend infinitely thin) innermost detection plane. This model also highly simplifies the estimation of energy loss and multiple scattering. The energy loss is accounted by means of the Bethe formula, while the multiple scattering effect is introduced in the form of equation 3.2, by assuming the deflection angle is Gaussian distributed.

In order to measure the distribution of material in the tracker detector different methods are used. For example, the methods based on extracting the number of photon conversions and nuclear interactions in the tracking volume are the most commonly used techniques. We propose a new technique that exploits the deflections experienced by particles as a consequence of the multiple scattering. In practice, by analyzing the collision events, the method checks the consistency between the real detector material distribution and the one assumed at the track reconstruction stage. Given that the latter is derived from the simulated detector setups, conclusions on the accuracy of the simulated setup can also be inferred. In the following section, after introducing the common techniques used in CMS, the proposed new method and the results obtained on the CMS inner tracker detector will be presented.

3.3 Photon Conversion and Nuclear Interaction Techniques

Photon conversion is a pair of oppositely charged electron-positron created in a secondary vertex. In early phase of CMS data taking, up to 70% of photons traversing the tracker material creates soft e^+e^- pairs mainly coming from π^0 decays which are very unlikely to reach the electromagnetic calorimeter. Due to strong magnetic field, the pairs open in the transverse plane and therefore it becomes possible to detect such signals especially close to innermost tracker layers thanks to dedicated algorithms implemented in the track reconstruction software (for more details see [52]).

The material distribution of Silicon Tracker varies between 0.1-1.5 interaction length. Therefore, large number of nuclear interactions with tracker material is expected in each event due to interaction of charged or neutral hadrons traversing the tracker. Nuclear interactions, as implemented in the software, are reconstructed when two or more charged tracks are originated from the same secondary vertex with an invariant mass above few hundreds of MeV.

The number of photon conversions and nuclear interactions depends on the amount of material placed in the detector and therefore can be used to probe the material distribution. Assuming a negligible contribution from fake tracks (misreconstructed tracks), the number of reconstructed photon conversion N_{conv} in a given volume is given by [52]

$$N_{conv} \propto \varepsilon_{conv} \cdot \langle \frac{P}{X_0} \rangle \cdot f_{geom}$$

where ε_{conv} is the reconstruction efficiency and $\langle \frac{P}{X_0} \rangle$ is the average conversion probability ($P \sim 7/9$). The geometrical correction factor f_{geom} represents the initial flux in a detector volume. Similar formula is written for nuclear interactions $N_{n.i.}$ and is given by [52]

$$N_{n.i.} \propto \varepsilon_{n.i.} \cdot \langle \frac{1}{\lambda_I} \rangle \cdot f_{geom}$$

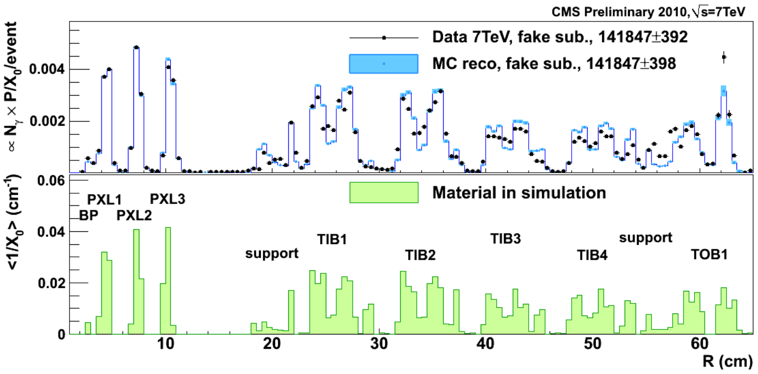

Fig. 3.5: Material distribution versus radius as estimated using reconstructed photon conversions from data. The plot at the bottom shows the material distribution implemented in simulation in average X_0^{-1} per bin [52].

If N_γ and N_{had} are the number of incoming photons and hadrons, formulations above, after subtracting fake tracks, for each geometrical volume can be redefined as photon conversion (or nuclear interaction) probability which are averaged in the counting volume.

Figures 3.5 and 3.6 show the amount of material measured for photon conversions and nuclear interactions from data, following the procedure mentioned above, with respect to radius of the tracker detector in a fiducial volume restricted to contain Pixel detector barrel and Inner Tracker barrel. For comparison, the material distribution, as implemented in the simulation, per X_0^{-1} and λ_I^{-1} bin are also plotted for each figure at the bottom. Figures clearly demonstrate that material description in the simulation is under control.

The ratio of number of photon conversion or nuclear interaction measured in data and simulation can be used for the comparison of material distribution between the real and simulated ones. Figure 3.7 shows this ratio for each substructure of the detector in radial bins in x axis. Overall agreement between data and simulation is at the level of $\sim$10% except a larger discrepancy observed in the "support" region between TIB and TOB.

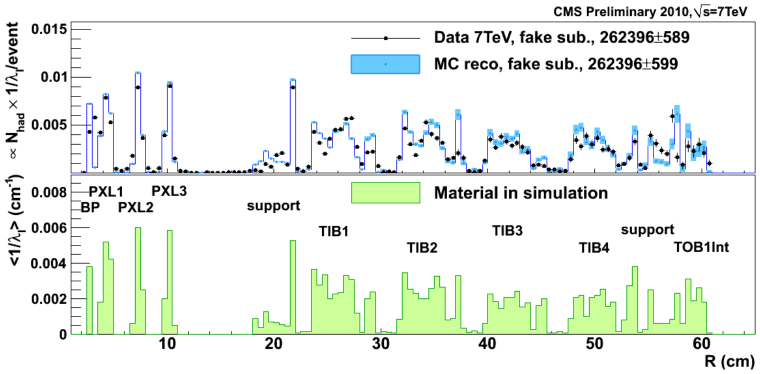

Fig. 3.6: Material distribution versus radius as estimated using reconstructed nuclear interactions from data. The plot at the bottom shows the material distribution implemented in simulation in average λ_I^{-1} per bin [52].

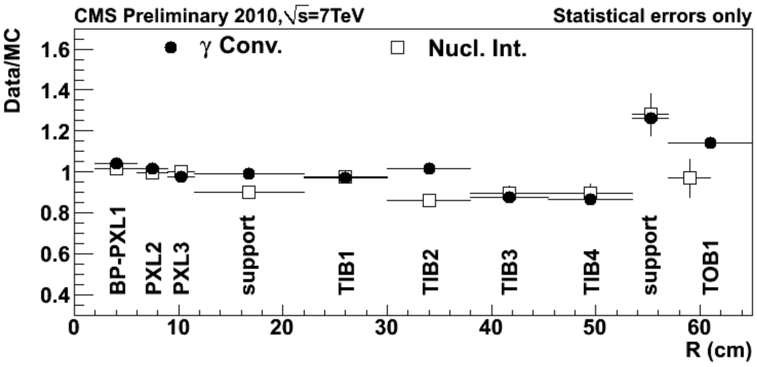

Fig. 3.7: Ratio of number of candidates for photon conversion (in circle) and nuclear interaction (square) measured from data over simulation in radial bins [52].

3.4 Multiple Scattering Technique

Multiple scattering plays an important role in the momentum resolution of a reconstructed charged track. In the case of the CMS inner tracker detector, it is the dominant effect in the momentum resolution for tracks with p_T up to 10 GeV/c, and accounts for 20 to 30% of momentum resolution at 100 GeV/c of transverse momentum [45]. The effect of multiple scattering on the reconstructed track trajectories can be exploited to probe the distribution of material in the tracker volume. The method is based on the standard CMS track reconstruction algorithm. As described in chapter 2, the CMS standard track reconstruction algorithm provides in each detection layer five estimated track parameters, together with estimated uncertainties in the form of a five by five covariance error matrix. The detection layers of the tracker are the sensitive silicon detectors as sketched in figure 2.2. The five track parameters and the associated covariance matrix will be referred as the track state at the considered detection plane in the following text.

In order to estimate the amount of material between two given detection planes, the track state on the starting plane (also called inner plane) is extrapolated to the destination plane (also called outer plane) under a certain assumption for the amount of material, which is the quantity that is being measured. In the extrapolation, the energy loss by ionization and the bending of the track in the magnetic field are taken into account. Although the energy loss by ionization also depends on the traversed material and affects the extrapolation, its effect is small compared to that of multiple scattering.

Therefore, as long as the particle momentum is below about 10 GeV, the uncertainty in the extrapolated track state on the destination plane is almost exclusively determined by the multiple scattering that the particle experiences while traversing the material between two detection planes. The uncertainty in the track state at the starting plane is another factor. However, the uncertainty in the track state at the starting plane is by far smaller than the uncertainty in the track state at the destination, thus the multiple scattering is expected to be dominant on the uncertainty in the extrapolated track state. Therefore the uncertainty in the extrapolated track state on the destination plane simply carries the information on the amount of material assumed between two detection planes at the reconstruction level.

The relevant observable that provides a direct comparison between the assumed amount of material and the actual one is thus the standard deviation of a Gaussian fit to the distribution of the ratio between the *residual* $(X_D - X_T)$ and the uncertainty in the extrapolated track state, which is given by

$$pull = (X_D - X_T)/\Delta_D. \tag{3.3}$$

Here X_D is the central position of the extrapolated track state at the destination and X_T refers to the central position of the track state updated with the measurement at the detection plane; Δ_D is the uncertainty in the extrapolated track state which is assumed to be mainly dominated by the multiple scattering. The standard deviation of the pull distribution σ^{pull} is obtained by a Gaussian fit to the pull distribution. The σ^{pull} will be called the sigma of the pull distribution and will be indicated more specifically by σ_i^{pull}, where i is an index that identifies the destination plane.

The distribution of the values of σ_i^{pull} must be equal to a unit Gaussian in the case the assumed amount of material coincides with the actual one. Gaussian distributions with sigma lower or larger than unity would indicate, respectively, an overestimation or an underestimation of the amount of material. This simple interpretation can not be strictly adopted if the track reconstruction is performed with different material distributions than in the actual detector setup. In fact, as already mentioned, the material distribution assumed by the CMS track reconstruction algorithm is a simplified one, where all material is concentrated at the starting detector surface.

3.4.1 Sensitivity of the Method

To avoid any unwanted bias, the position measurement on the destination plane and all the following measurements are not used in the computation of the track state on the starting plane.

Although the uncertainties in the extrapolated track state can also be affected by the uncertainties in the magnetic field, energy loss and position (alignment) of the detector, they are assumed to have a negligible contribution in comparison to multiple scattering effects as long as low momentum tracks are used. The uncertainty in alignment is around 10 μm while the effect of multiple scattering, which in general dominates the position resolution as well, is around 100-200μm. Therefore, the method is expected to suffer little from the effects of misalignment and other detector mis-calibrations. It should be noted that little statistics is sufficient to extract results in the entire tracking detection volume. On the other hand, it should be stressed that the method has no or little sensitivity to the actual details of the material distribution between two detection layers.

3.5 Iterative Corrections to the Track Reconstruction Material Model

The standard track reconstruction with its assumed material model can be tested with the multiple scattering method. If the reconstruction model describes well the material in the detector, one assumes to have a unit sigma of the pull distribution for each detector layer in which the material is being measured. In case the pull distributions do not have unit sigma, a correction factor, extracted from the pull distributions, can be computed and applied on the material model.

However, given the fact that the value of a correction relies on the other amount of materials (not yet corrected) to be correct, the corrections computed in this fashion do not allow in general to achieve the unit sigma results, though they improve the overall situation. Therefore the procedure is repeated iteratively until convergence to stable corrections is obtained. Using the equations 3.2 and 3.3, the correction factors that will be applied to the amount of material in between the layers L_i and L_{i+1} can be approximated to

$$c_i = (\sigma_{i+1}^{pull})^2. \tag{3.4}$$

Here σ_{i+1}^{pull} is observed sigma of the pull distribution in layer L_{i+1}. The assumptions made in the derivation of the relation are: the deviation from the trajectory is only due to the multiple scattering of the particle traversing this material in between the two detection planes, and the assumption of Gaussian distributed small deflection angles in the form of equation 3.2 where the width of the distribution is proportional to square root of the material thickness.

The final correction factor that should be applied to the material model is the multiplicative correction factors obtained in each iteration. We end up having a set of factors $\{C_i\}$ of

$$\begin{aligned} C_i &= c_i^1 \times c_i^2 \times c_i^3 \times ... \times c_i^n \\ &= \prod_{j=1}^{n} c_i^j \end{aligned} \tag{3.5}$$

where n is the number of iterations performed. Note that i is the layer number, not the number of iterations.

3.5.1 Feasibility Tests

In order to apply this method, there are few points that have to be verified. First is the convergence, meaning that the method should yield stable and accurate corrections after a relatively small number of iterations. The method should lead to distributions with close to unit sigma in as small as possible number of iterations. Another point is that the method should have little dependence on the material distribution on other detection layers. This condition can be satisfied as long as low momentum tracks are used, such that the uncertainty in the extrapolated track state is dominated by the multiple scattering and not by the effect of misalignment and hit resolution at the detection layers. Another point that should be verified is that the initial conditions should not affect the results.

In order to verify the conditions mentioned above, we simulated single muon particles with opposite charge, having a momentum of 1 GeV in all regions of the detector. We run the track reconstruction with its simplified material model to obtain the first iteration factors, then we continue to iteration by modifying the reconstruction material model with the obtained factors until we converge to the unit sigma distributions on the pulls. The material in the last barrel layer is kept constant we have no means to test this material because of the lack of accurate position measurements further out. Figure 3.8 and 3.9 show the sigma of the pull distributions with respect to layers of detector before and after iterations in barrel and edcap+ region. The simulated tracks having 1GeV momentum are used to obtain the distributions. Figure 3.10 shows the pull distribution obtained by modifying the material by a factor two in the barrel $|\eta| < 0.6$, using an ideal scenario (no misalignment). Figure 3.11 shows the same pull distributions after the second iteration.

As it was noted before, the method should be independent from the starting conditions. Figure 3.12 shows the standard deviation of the residual distribution for barrel layers up to the second iteration step starting from the standard reconstruction material. In all iteration steps, the residual distributions do not change significantly, the only difference is the uncertainty in the propagated track state, because of the multiple scattering effect being dominant.

Figure 3.13 is a good way to compare the sigma of the pull distributions obtained on barrel layers, after first and second iterations, starting from a factor two increased tracker material. As can be seen, the convergence is reached after a very low number of iterations. Simply two iteration steps are enough to reach the unit sigma on the pull distributions.

The final correction factors obtained with simulated events using the

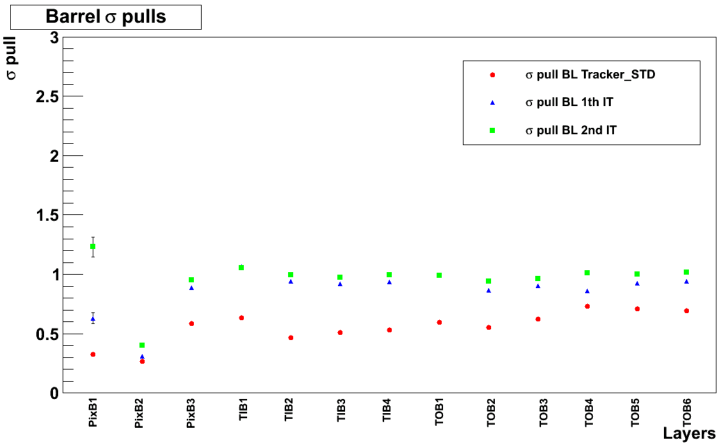

Fig. 3.8: The sigma of the pull distributions for barrel layers, including the ones from pixel detector, with simulated events having 1 GeV momentum before and after iterations starting from the standard material model in the reconstruction.

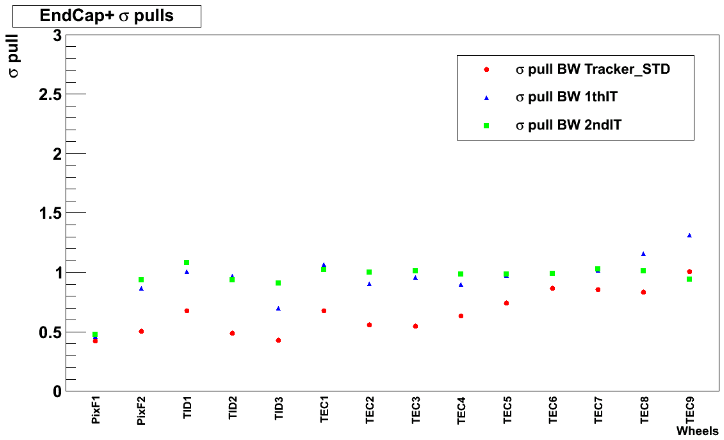

Fig. 3.9: The sigma of the pull distributions for endcap+ wheels, including the ones from pixel detector, with simulated events having 1 GeV momentum before and after iterations starting from the standard material model in the reconstruction.

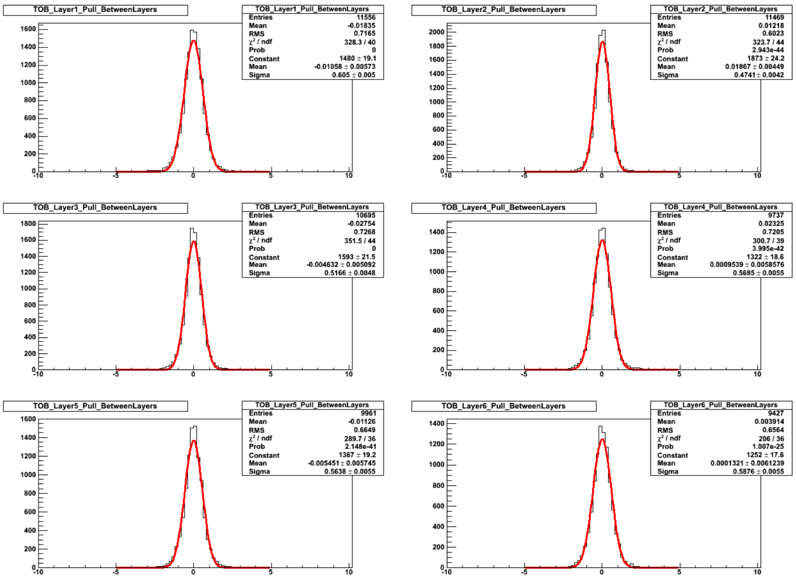

Fig. 3.10: The pull distributions for outer barrel layers (TOB) with simulated events. The factor two increased material model was run during the reconstruction.

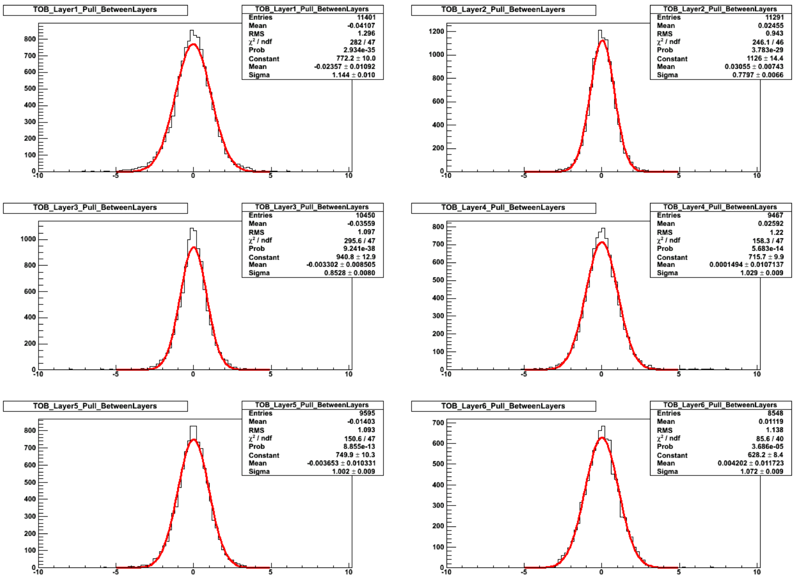

Fig. 3.11: The pull distributions for outer barrel layers (TOB) with simulated events after 2nd iteration. The factor two increased material model was run initially.

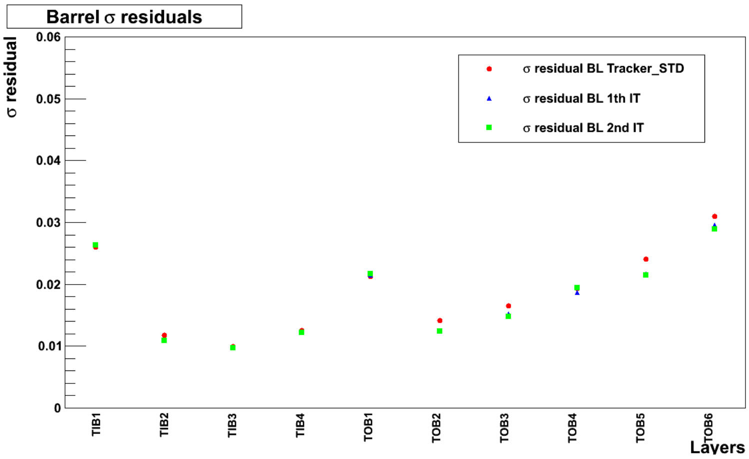

Fig. 3.12: The sigma of the residual distributions for barrel layers with simulated events, starting from the standard material model, after 1st and 2nd iterations.

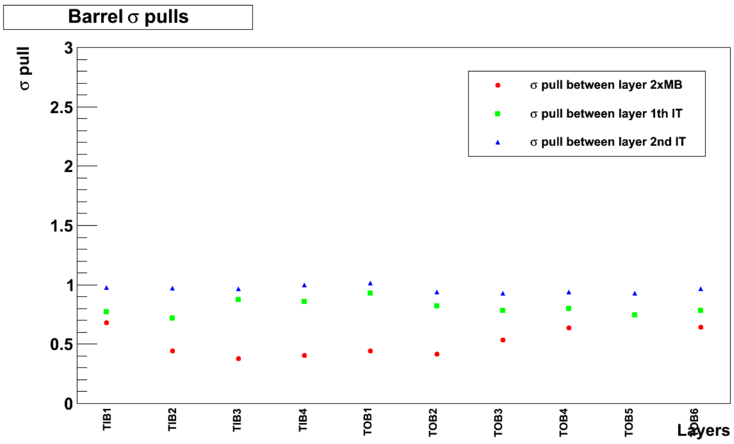

Fig. 3.13: The sigma of the pull distributions for barrel outer tracker layers (TOB) for simulated events, starting from factor two increased material, after the first and 2nd iterations.

material models described above can be seen in figure 3.14, for barrel and the plus-side end-cap region of the detector. The correction factors obtained starting from the configuration in which the inner tracker material was increased by a factor two have been divided by a factor two in order to ease the comparison with the same corrections obtained starting from the nominal configuration.

The results indicate that the standard material model adopted by the reconstruction algorithms is not adequate. The amount of material assumed in the track reconstruction software should be in general reduced by about a factor of two in order to be consistent with what assumed in the detailed simulated set-up, implemented in Geant4, of the inner tracker. This large bias may have escaped so far to the CMS Collaboration.

The (most) possible explanation for these striking results could be the fact that the standard track reconstruction algorithm assumes the concentration of all material in infinitely thin detection planes, and that the effect of the multiple scattering is assumed to take place at the starting detection layer, thus amplifying the effect of multiple scattering via the large lever arm that this assumption implies. Of course, other possible

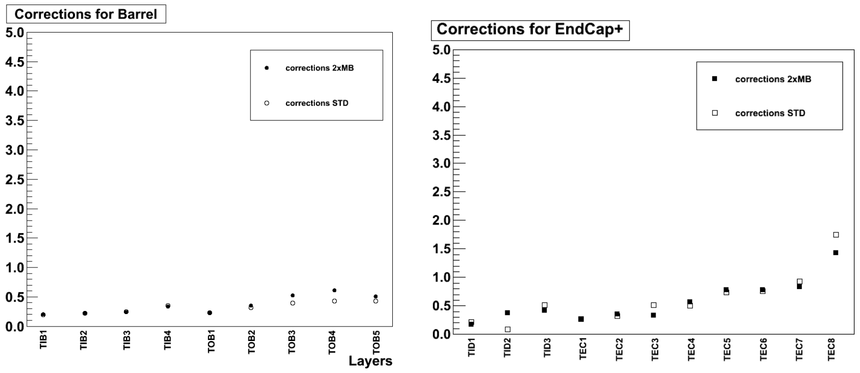

(a) (b)

Fig. 3.14: The correction factors (C_i) after two iterations for barrel (a) and for the ed-cap region (b) of the detector. Starting from factor two increased and standard material model, respectively.

explanations can be that the method of calculating the correction factors is not fully correct and (or) the assumptions made during the derivation of the correction factors do not hold in all cases; possible biases from previously used layers in the track state might be present as well. In any case, the other important conclusion of these results is that regardless of the initial material configuration, the method converges quickly and to the same final result.

3.6 Direct Measurement with the Collision Data

We now want to check the consistency between the material distribution in the real experiment and the material distribution in the detailed simulated setup, thus the standard track reconstruction with its simplified material distribution was run on both simulation and data. While simulated tracks experience the material present in the simulated setup, real reconstructed tracks experience the material of the actual detector setup. The ratio of the σ_i^{pull} values obtained on simulation and data provides a direct comparison between the amount of material present in the simulated and in the real setup. A ratio smaller (larger) than unity

A	B	C	D
$0< \|\eta\| <0.6$	$0.6< \|\eta\| <1.3$	$1.3< \|\eta\| < 1.7$	$1.7< \|\eta\| < 2.4$
1-1.1	1.6-1.8	2.4-2.7	3-3.3

Tab. 3.1: Selection of the samples of tracks according to their pseudo-rapidity (first row) and momentum range (second row).

would indicate that the amount of material in the simulated setup is smaller (larger) than the amount of material in the real setup.

3.6.1 Event Selection and Categorization

The collision events used to perform this measurement correspond to the a luminosity of $1.0\pm\ 0.1\text{nb}^{-1}$ collected by CMS detector during 2010 in stable conditions with all sub-detectors and magnet fully operating. A good reconstructed primary vertex associated to at least four tracks and its position within 15cm in longitudinal and 2cm in transverse plane with respect to beam spot are required. Beam-induced background events, producing an anomalously large number of hits in pixel detector, are rejected in the collected events. The MC datasets are generated with Phyhia6 and reconstructed with CMS software. Tracks having a transverse (longitudinal) impact parameter with respect to the primary vertex smaller than 0.1cm (1cm) are chosen. The collected events are categorized in samples as A, B, C, D according to their momentum range and pseudorapidity as shown in table 3.1.

The pull distributions for the TIB, TOB, TID and TEC detection planes are in all cases well fitted by a Gaussian function. As an example, the pull distributions for the four TIB detection layers obtained with the tracks from sample B observed data are shown in figure 3.15. In general the pull distributions are approximately Gaussian distributed and the sigma of the pull distribution σ_i^{pull} values are in general lower than unity, as also observed in the case of simulated tracks (see previous section). As discussed above, these low values are somehow expected because they could partly be due to the simplified material model adopted in the track reconstruction.

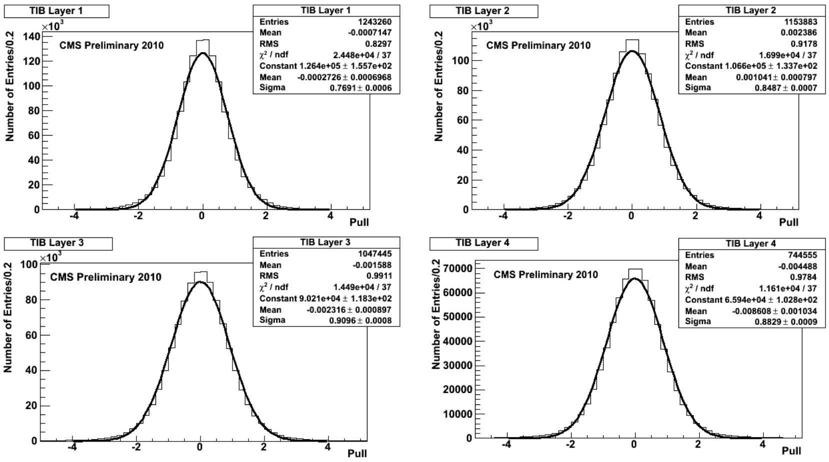

Fig. 3.15: Pull distributions at the four TIB detection planes obtained with tracks in sample B for observed data

The same conclusions do not hold for the distributions related to the pixel detection planes, which seem to be better fitted by the sum of two Gaussian curves with different widths. A possible explanation of this feature could be the presence of zones, within the considered η ranges and, possibly, along the ϕ coordinate, where the level of agreement between the assumed and actual amount of material is significantly different. Given that a simple Gaussian fit is not appropriate for the pull distributions relative to the pixel detection layers, only results related to the silicon strip detection layers are presented.

3.6.2 Systematic Effects and Sensitivity

The robustness of the technique with respect to misalignment effects and the sensitivity to differences in the assumed and actual amount of material can be computed with σ_i^{pull} values on simulated tracks under different conditions. The following scenarios were considered:

1. a perfectly aligned setup (ideal);

2. a misaligned (and mis-calibrated) setup, as expected at the start-up of the experiment (start-up);
3. the same misaligned setup, but with an assumed amount of material at the track reconstruction level increased by 20% with respect to the default one, which corresponds to the actual material at the detector simulation level;
4. the same misaligned setup, but with an assumed amount of material at the track reconstruction level decreased by 20% with respect to the default one, which corresponds to the actual material at the detector simulation level.

Three different ratios of the σ_i^{pull} values obtained in the scenarios listed above are shown in figure 3.16, 3.17 and 3.18. The statistical uncertainties on these ratios, deriving from the uncertainty on the fitted σ_i^{pull}, are much smaller than the size of the symbols used in the plots. In figure 3.16 the results were obtained with sample A using the simulated events, similarly in figure 3.17 with sample C and in figure 3.18 with sample D, in different η slices.

These results indicate that the method is, for all barrel layers except the first one, indeed sensitive to differences at the level of 20% between assumed and actual amounts of material and that systematic effects deriving from the misalignment expected at the start-up of the experiment would yield smaller observed discrepancies, of the order of 5%. The small observed value of the σ_i^{pull} ratio between start-up and ideal scenarios for the first barrel layer indicates that differences in these scenarios at alignment level dominate over differences in material at the level of 20%.

The results obtained in all end-cap layers demonstrate the dependence of the alignment at a level of 10-15%. This is expected behavior since the alignment effect in end-cap region of the detector is more dominant than in the barrel.

The absolute values of σ_i^{pull} obtained for MC generated events are shown in figure 3.19 for barrel $|\eta| <0.6$ region using sample A. It can be noted

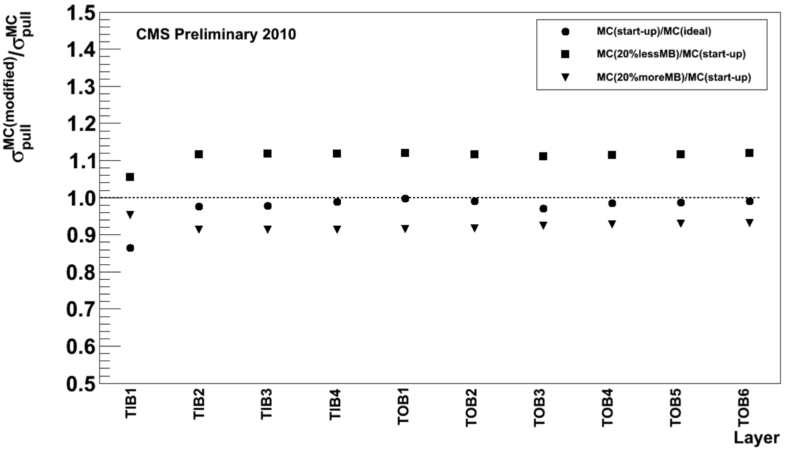

Fig. 3.16: Ratio of pull distributions obtained with simulated sample A. The circles compare the start-up and ideal scenarios. The triangles and squares show the effect of variation of the material by ±20% in the start-up scenario at the reconstruction level. The detection layers on the x-axis are the destination layers.

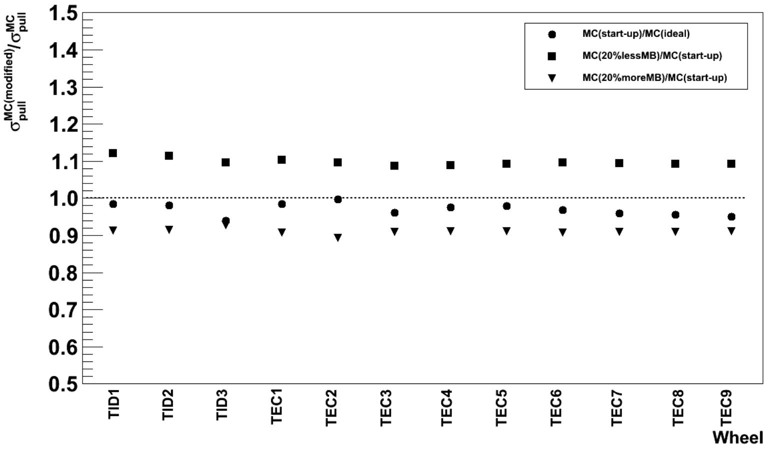

Fig. 3.17: Ratio of pull distributions obtained with simulated sample C. The circles compare the start-up and ideal scenarios. The triangles and squares show the effect of variation of the material by ±20% in start-up scenario at the reconstruction level. The detection layers on the x-axis are the destination layers

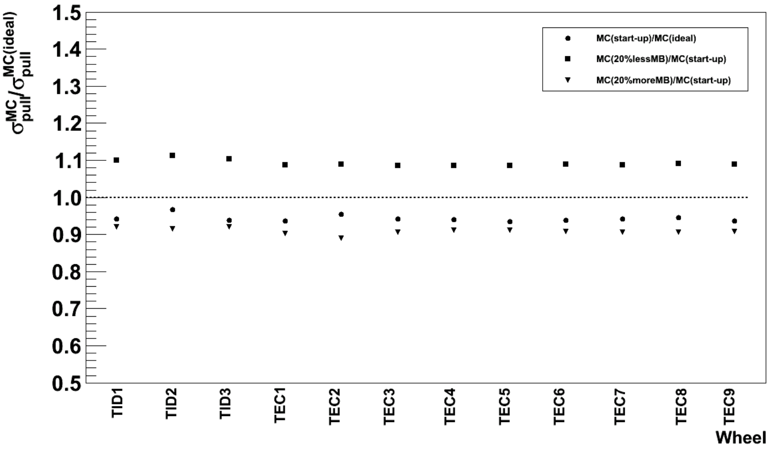

Fig. 3.18: Ratio of pull distributions obtained with simulated sample D. The circles compare the start-up and ideal scenarios. The triangles and squares show the effect of variation of the material by ±20% in the start-up scenario at the reconstruction-level. The detection layers on the x-axis are the destination layers

that the default σ_i^{pull} distribution are lower than unity. The effect of changes in the material at the reconstruction level can be clearly seen. The overall difference in the sigma of the pull distribution due to misalignment is less pronounced in the barrel region of the detector than in the end-cap.

Another very important robustness test is performed by comparing the results obtained with different track state parameters. The CMS track reconstruction algorithm performs the track reconstruction “inside-out”, starting from the inner layer to outer layer until the last layer of the detection plane is reached. Then, as also explained in chapter 2, in order to have the most accurate measurement also at the innermost layer, the backward propagation “outside-in” is performed as well. The final track parameters are the result of combined track states of these two fitting algorithms.

The results of the test are shown in figures 3.20, 3.21, 3.22 and 3.23 with respect to each η region of the detector using different samples,

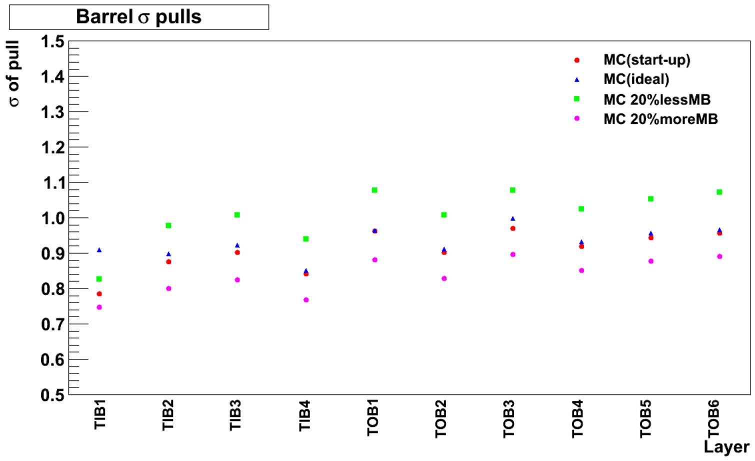

Fig. 3.19: Sigma of pull distributions obtained with simulated sample A for the start-up and ideal scenarios together with the effect of variation of the material ±20% in start-up scenario at the reconstruction-level.

as explained in the figures. The figures show the ratio of the sigmas of the pull distributions of MC events and collision data for different track states used in equation 3.3. The inside-out track fit parameters are called *forward state* and the combined result of inside-out and outside-in track fitting is referred as *updated state*. In order to not bias the results by using the subsequent hits in the updated track state, the forward track state parameters are chosen to be used in the direct comparison with the collision data.

It is important to check the sensitivity of the method in the measurement of the material distribution. This can be verified by altering the material and investigate the effect of this difference in the obtained distributions. For this test, the material between layer 3 and 4 in TIB and between layer 4 and 5 in TOB, are modified by ±20%. Figure 3.24 shows this test results obtained with MC generated events. The plot shows the ratio of the pull distribution with modified material at the reconstruction-level. The filled circles correspond to the ratio of sigma of pull distributions of +20% material; on the other hand, the circles correspond to -20% material difference. The results of this performance

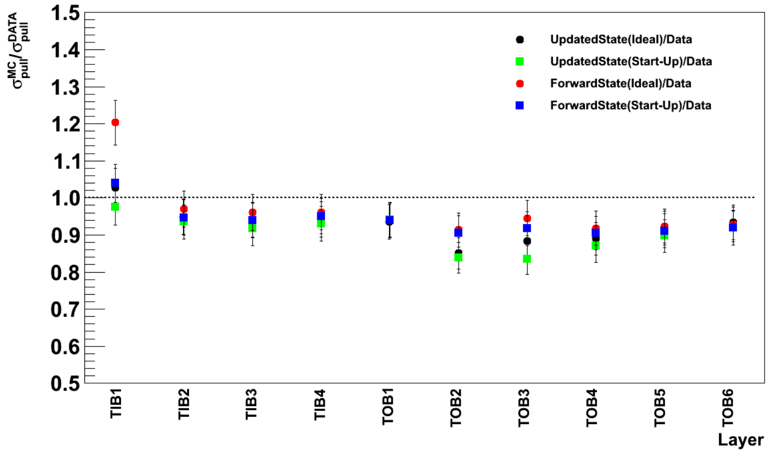

Fig. 3.20: The ratio of pull distributions of simulated events to obtained data, for the sample of A. The forward and updated track states are tested in MC with respect to the start-up and ideal scenarios at the reconstruction-level.

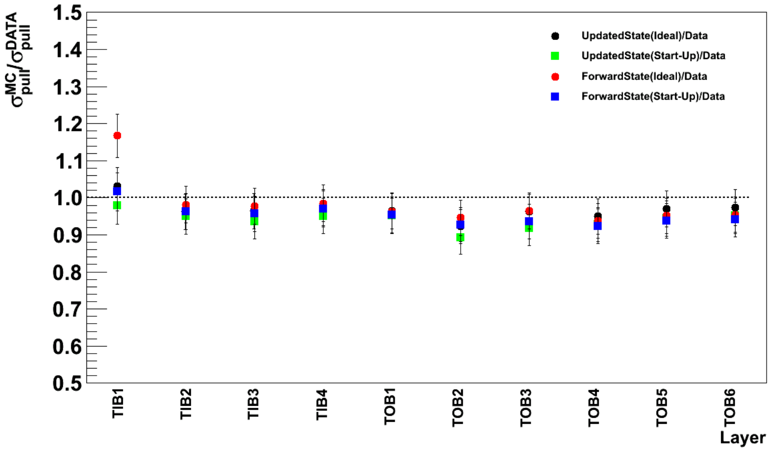

Fig. 3.21: The ratio of pull distributions of simulated events to obtained data, for the sample of B. The forward and updated track states are tested in MC with respect to the start-up and ideal scenarios at the reconstruction-level.

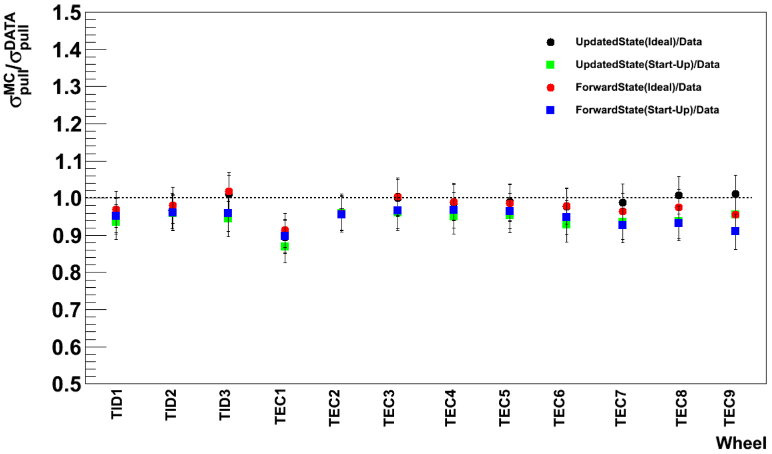

Fig. 3.22: The ratio of pull distributions of simulated events to obtained data, for the sample of C. The forward and updated track states are tested in MC with respect to the start-up and ideal scenarios at the reconstruction-level.

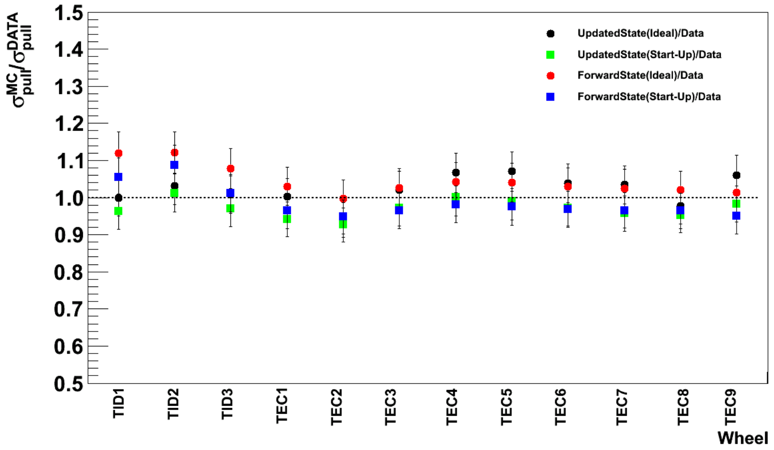

Fig. 3.23: The ratio of pull distributions of simulated events to obtained data, for the sample of D. The forward and updated track states are tested in MC with respect to the start-up and ideal scenarios at the reconstruction-level.

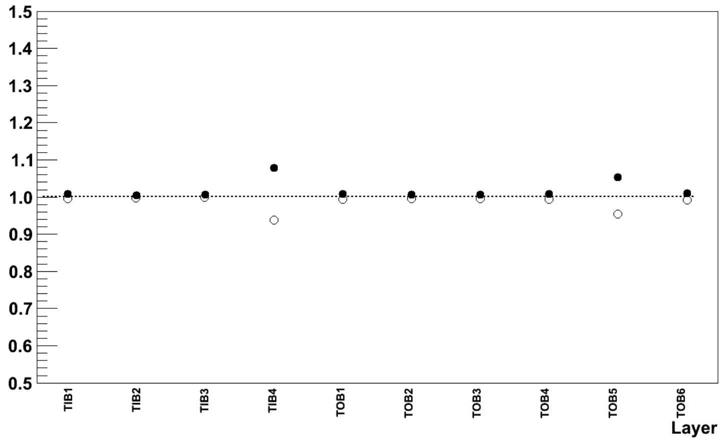

Fig. 3.24: The ratio of pull distributions of simulated events for the sample of A. The forward track state is used with modified material in between two detection layers at the reconstruction-level.

test show the robustness of the method as well as its excellent sensitivity.

3.6.3 Analysis Results

The ratio of the σ_i^{pull} values obtained on simulation and data for barrel and end-cap are shown in figure 3.25 and figure 3.26, respectively. Based on the results presented in figure 3.16 and 3.17, a systematic uncertainty of 5% is assigned to the measurements on every detection layer, except for the first barrel layer where a value of 10% is used. The ratio of the σ_i^{pull} values is generally close to one in all cases. Therefore it can be concluded that the amounts of material in the real and simulated Silicon Strip Tracker detector agree within ≈15% in both barrel and end-cap regions.

3.7 Conclusions

We have shown a novel method to measure material distribution of a tracking detector using the reconstructed tracks. The detailed descrip-

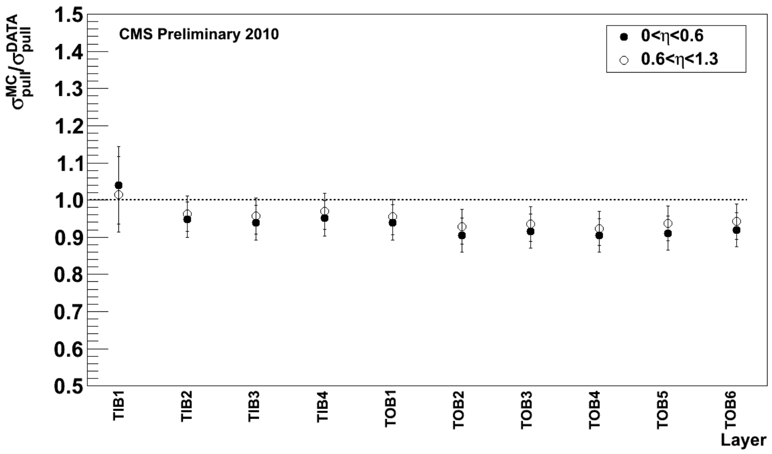

Fig. 3.25: Ratio of pull distribution for the values obtained in data and MC for barrel detection planes. The detection layers on the x-axis are the destination layers.

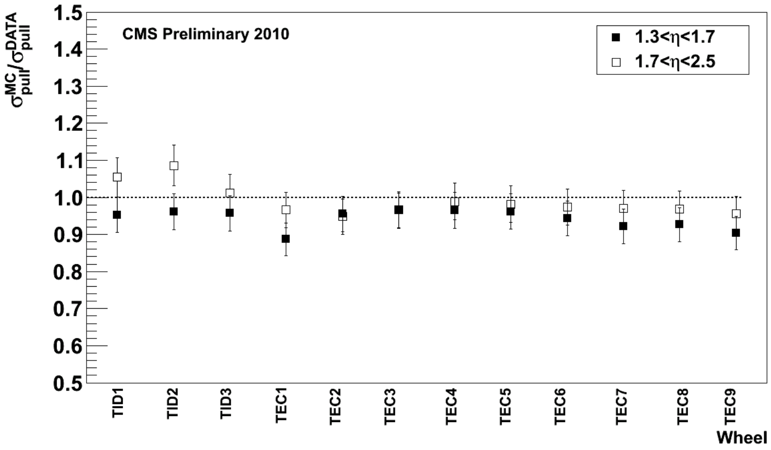

Fig. 3.26: The ratio of pull distributions obtained on simulation and data for the end-cap detection planes.

tion of the method and all possible systematic effects are discussed. The robustness and the sensitivity of the method are demonstrated using the MC generated events. As shown the method is robust against all possible detector effects and therefore sensitive to measure to material distribution in the CMS tracking volume to an accuracy of about 10%.

The method, in principle, can improve the material description in the standard track reconstruction algorithm. The studies with this motivation are presented in detail. Based on the correction factors derived from MC studies, the material description in the reconstruction software is found to be not adequate. The results indicate that the material in the reconstruction model should be decreased by factor two in order to obtain the unit sigma of the pull distributions. However, this result is expected to reflect not an actual lack of material, but rather an incorrect distribution of this material arising from the simplified model adopted in the reconstruction software.

It is found that the pull distributions used as observables in the measurement are well Gaussian distributed in all cases except pixel layers. The results of the tests show that the effect of misalignment and the detector conditions in the observable are around 5% in the barrel and can reach the level of 10-15% in the endcap. The material description in the simulation and the real detector set-up agrees within 10 to 20% in overall detector volume using the collision data.

In comparison to other methods aiming to perform similar measurements, for example the reconstruction of secondary vertices resulting from photon conversions and nuclear interactions in the tracking volume (see ref [52]) as described in section 3.3, our method is demonstrated to be relatively simple and data driven. It is not affected by the systematic uncertainties as such methods suffer from. Additionally, little statistics of reconstructed tracks are enough to give the results in overall detector volume. However it should be noted that the method has no or little sensitivity in details of the distribution of the material between detection layers. The results are in agreement and complementary to these more traditional methods performed independently, and can give feedback to the physics analysis for evaluation of the tracker related systematic uncertainties.

Chapter 4

The Matrix Element Likelihood Method

The classical analysis technique, where a possible resonance is searched in an invariant mass spectrum, is among the most common analysis methods used in high energy physics, as described in chapter 1. Such analysis techniques only exploit the information of the invariant mass of the final state decay products of the resonance. On the other hand, the more sophisticated multivariate analysis method, for example the Matrix Element Method, uses the full kinematic information of all the measured particles in the event, that an experiment can provide. Therefore the Matrix Element Method, in principle, could provide a better sensitivity for a signal searched on top of a smooth background.

This chapter presents a pure likelihood-based analysis approach with the Matrix Element Method for a possible improvement in sensitivity of the search for di-muon resonances. The first section of this chapter is an introduction to the Matrix Element Method and the general description of how the likelihood function based on this method can be constructed and used with offline reconstructed detector-level events in an analysis. The following sections focus on the use of this method in a statistical analysis built upon the joint pdfs of a possible signal and a known background model.

4.1 The Method

4.1.1 Introduction to the Matrix Element Method

The Matrix Element Method (or Dynamical Likelihood Method) [53, 54] uses the probability densities of the final states observed in an experiment, assuming that final states have taken place for a given parton-level process. In order to compute this probability density function, the uncertainties on the measurements should be taken into account. The infinitesimal probability density can be written

$$dP(x,y) = N d\sigma(y)/dy\, w(x|y)dx, \tag{4.1}$$

where $d\sigma$ is the parton-level differential cross section y is the set of kinematical variables defining the event at parton level, x is the set of kinematical variables of a given event as measured by the experiment, N is a normalization factor and $w(x|y)$ is so-called the transfer function, which represents the probability density function that a parton-level event y is observed as x by the experiment. The factor N and the transfer function will be discussed in the detail in the following sections.

The formulation above involves the squared matrix element of a given process, therefore the method is commonly known as the *"Matrix Element Method"* in high energy particle physics. The method first was successfully used in Tevatron experiments for the top quark mass measurement [55]. Since then, it has been used in few other occasions, for example, in the search for the Higgs boson in the $H \to ZZ^*$ to four leptons performed by CMS [56].

The method is in principle capable of exploiting the full kinematic information of all measured particles contained in observed events used as observables. The likelihood function built with the matrix element can also represent a powerful tool in searches for signals of physics beyond the standard model. Once a discovery of such a signal is established, the method can be used for the measurements of the parameters of the new model best describing the data.

Following sections are the discussions of how a likelihood function for an experiment can be built using this method with detector-level reconstructed events and the incorporation of systematic uncertainties.

4.1.2 Construction of the Likelihood Function

The likelihood function corresponding to an observed set of data, x, gives the probability density that an underlying model, defined in terms of a set of parameters M, yields the observed data. The likelihood is a function of the parameters M and, for the purpose of making measurements, it can be maximized. The likelihood function is also very important when searching for BSM physics, that is when there is no measurement to be made, but rather two alternative hypotheses to be compared (the background-only versus the background+signal). Its importance in such situations stems from the fact that the ratio of likelihoods corresponding to two alternative models is the most powerful test statistic for separating the outcomes of the two models, as established by the Neyman-Pearson lemma [57]. Therefore, our aim is, without requiring any other intermediate steps, to build accurately a likelihood function corresponding to an experimentally observed di-muon final state in the background-only and background+signal hypotheses, and use their ratios in the test statistics.

First, we show the main principles of the construction of the event likelihood via the underlying model parameters while taking into account all possible effects of the experimental detector set-up. Later, we build the likelihood for a set of events that can be observed in the experiment.

The probability of occurrence of a physics process can be given in terms of the invariant squared matrix element $|\mathcal{M}|^2$ of the scattering amplitudes for the underlying physics processes and the underlying model parameters (M) at the parton level. The differential cross section a parton-level process can be written

$$d\sigma_M = \frac{(2\pi)^4|\mathcal{M}|^2}{x_1 x_2 s} d\phi_n, \tag{4.2}$$

where $d\phi_n$ is the n-body phase-space element. Then, the total differential cross section summed over all initial parton states in the proton collisions is given by

$$d\sigma = \int_{x_1,x_2} \sum_{i,j} f_i(x_1) f_j(x_2) dx_1 dx_2 d\sigma_M. \qquad (4.3)$$

In order to construct the likelihood function, we need the *probability density function* (pdf) of the experimental outcome x, given the underlying model parameters M. The probability of having an experimental outcome x, given by a theoretical parton-level final state y, resulting from a model M, is given by

$$d^2P(x,y|M) = dP(y|M)dP(x|y) = \frac{1}{\sigma}\frac{d\sigma}{dy} dy w(x|y) dx, \qquad (4.4)$$

where σ is the total cross section for the process. Equation 4.4 yields to

$$P(x,y|M) \equiv \frac{d^2P(x,y|M)}{dxdy} = \frac{1}{\sigma}\frac{d\sigma}{dy} w(x|y) \qquad (4.5)$$

The parton-level differential cross section must be intended as a result of the integration of the parton distribution function and the matrix element of the corresponding physics processes (see equation 4.3). The implicit assumption is that an observed event (x) is not the result of a superposition of independent proton-proton collisions.

Here $w(x|y)$ is called the transfer function and defines the probability density function of measurements x, given a true parton-level final state y. It carries the information of the detector resolution on individual parton-level objects and detection efficiency.

The transfer function should satisfy the normalization condition over all reconstructed phase space. Namely, if X and Y are the full phase space of measured and parton-level objects, the transfer function must satisfy the condition of

$$\int_X w(x|y)dx = 1 \quad \text{(for any y in Y)}. \tag{4.6}$$

The pdf of an experimental outcome x, given M, is obtained from eq. 4.5 as

$$\frac{dP(x|M)}{dx} \equiv P(x|M) = \int_Y \frac{1}{\sigma}\frac{d\sigma}{dy} w(x|y)dy \tag{4.7}$$

and satisfies the condition of

$$\int_X P(x|M)dx = 1 \tag{4.8}$$

which is integrated over the phase space of all possible experimental outcomes X.

4.1.2.1 Normalization of the Likelihood Function

Having equations 4.7 and 4.8 at hand would allow in principle to construct the likelihood function for a set of experimental events x_i. However, the events x_i used in an experimental analysis have usually undergone online and offline event selections. Although analysis selection criteria are mostly introduced with the aim of reducing the background events, they also affect the efficiency for selecting signal events. For this reason the parent pdf of the x_i selected events must be defined only in the reduced space, X' of the events that are effectively observed in the detector and pass the analysis event selection. This fact has important implications.

Thus the pdf in x and y for events passing the analysis selection will be null in $X - X'$ and proportional to eq. 4.5 within X'. In other words, we must modify the pdf in equation 4.5 as

$$\begin{aligned} P(x,y|M\text{and}\,x\text{ in }X') &= K\frac{1}{\sigma}\frac{d\sigma}{dy}w(x|y)\;(for\,x\,in\,X'\,and\,y\,in\,Y) \\ &= N\frac{d\sigma}{dy}w(x|y)\;(for\,x\,in\,X'\,and\,y\,in\,Y), \end{aligned}$$

where the factor $N = \frac{K}{\sigma}$ can be determined by imposing the normalization condition of

$$\int_{X',Y} P(x,y|M\text{and}\,x\text{ in }X')dxdy = 1,$$

which yields to

$$N = \frac{1}{\int_{X',Y}\frac{d\sigma}{dy}w(x|y)dxdy}.$$

Now we have the problem of the integration over the full Y phase space. In fact, because of singularities, the differential cross section for many processes can not be integrated over the full Y. Theorists can only safely compute perturbatively total cross sections in reduced parton-level phase spaces. The experimental analysis selection, i.e. the fact that the integration over the variable x is only in the reduced space X', helps overcome this problem. Having the integration to restricted visible phase-space X', one can make the assumption that there is a reduced parton-level subspace Y' such that $w(x|y) = 0$ for any x in X' and y in $(Y - Y')$. This condition, which arises from the sufficiently good resolution of the detector, basically guarantees that the integration over y does not need to be performed down to very low particle energies and for collinear partons (isolation conditions applied at reconstruction level) , where the singularities occur. With this assumption, we write:

$$\begin{aligned} \int_{X',Y}\frac{d\sigma}{dy}w(x|y)dxdy &= \int_{X',(Y-Y')}\frac{d\sigma}{dy}w(x|y)dxdy + \int_{X',Y'}\frac{d\sigma}{dy}w(x|y)dxdy \\ &= 0 + \int_{X',Y'}\frac{d\sigma}{dy}w(x|y)dxdy \end{aligned}$$

and the normalization factor is equal to

$$N = \frac{1}{\int_{X',Y'} \frac{d\sigma}{dy} w(x|y) dx dy}. \tag{4.9}$$

This integral is calculable and does not suffer from theoretical singularities. The choice of Y' is completely analysis driven. In other words, this phase space is defined by the parton-level configurations. It should be large enough to comprise the whole subspace of reconstructed visible objects. It is defined by parton-level requirements that are loose enough such that the probability that a parton-level event that fails such requirements and, at the same time, gives rise to an experimental observed event that pass the analysis selection, is 0 to an excellent approximation.

The integration over X' in the denominator of the normalization factor results in a function $\varepsilon(y)$, that returns for any given parton-level configuration y, the efficiency to end up in X'. This aspect is very often forgotten when the matrix element method is applied. Indeed the transfer function $w(x|y)$ is usually constructed in the form of a unit-normalised resolution function that simply smears the energy and directions of the final state partons in order to reproduce the experimental effects. The detection efficiency and the event selection are wrongly neglected in such an approach. The remaining integral in Y' can be seen as the integral of differential cross-section weighted by this efficiency $\varepsilon(y)$. The result is the total cross-section times the total efficiency for a parton-level event in Y' to pass the analysis selection. Therefore N will be

$$N = \frac{1}{\int_{X',Y'} \frac{d\sigma}{dy} w(x|y) dx dy} = \frac{1}{\varepsilon' \sigma'}. \tag{4.10}$$

The total cross section (σ') for a given process can be found in the literature or computed with event generators, while the calculation of the efficiency term (ε') will require the full simulation, reconstruction and emulation of the analysis selections of events generated in space Y'.

Using the same reasoning, the pdf of experimental, observable outcome x, given the underlying model M, reads, replacing equation 4.7

$$\begin{aligned} P(x|M \text{and } x \text{ in } X') &= \int_Y N\frac{d\sigma}{dy}w(x|y)dy \\ &= \int_{Y'} N\frac{d\sigma}{dy}w(x|y)dy + \int_{Y-Y'} N\frac{d\sigma}{dy}w(x|y)dy \\ &= \int_{Y'} N\frac{d\sigma}{dy}w(x|y)dy \\ &= \frac{1}{\varepsilon'\sigma'}\int_{Y'} \frac{d\sigma}{dy}w(x|y)dy. \end{aligned} \tag{4.11}$$

Using this pdf, we can write the likelihood corresponding to an experimentally observed event x, as a function of a set of underlying model parameters M as

$$L(x|M) = pdf(x|M \text{ and } x \text{ in } X') = \frac{1}{\varepsilon'\sigma'}\int_{Y'} \frac{d\sigma_M}{dy}\varepsilon(y)w'(x|y)dy, \tag{4.12}$$

where we have rewritten the full transfer function as the product of an efficiency function $\varepsilon(y)$, giving the probability that a parton-level event y ends up in the space X', and a unit normalized transfer function that, for convenience we indicate, in the following with the symbol $w'(x|y)$, to distinguish it from the full transfer function as

$$w(x|y) = \varepsilon(y)w'(x|y).$$

4.1.2.2 Full Likelihood Function with Model Parameters

In the case of two (or more) exclusive non-interfering underlying physics processes (M_1 and M_2), the corresponding model pdfs must be the linear combination of each probability using the respective total probability of occurrence

$$P(x|M_1 + M_2) = N_1 P(x|M_1) + N_2 P(x|M_2). \tag{4.13}$$

If we write this formula using the relative probability of each process of our interest in an LHC bunch crossing in terms of total cross sections, the resulting pdf thus should be equal to

$$\begin{aligned} P(x|M_1 + M_2 \,\text{and}\, x \,\text{in}\, X') = & \frac{\sigma_1\varepsilon_1}{\sigma_1\varepsilon_1 + \sigma_2\varepsilon_2} P(x|M_1 \,\text{and}\, x \,\text{in}\, X') + \\ & \frac{\sigma_2\varepsilon_2}{\sigma_1\varepsilon_1 + \sigma_2\varepsilon_2} P(x|M_2 \,\text{and}\, x \,\text{in}\, X'). \end{aligned} \tag{4.14}$$

The likelihood for a set of *"n"* selected events is

$$L(\{x_i\}|M_1 + M_2 \,\text{and}\, x_i \,\text{in}\, X') = \prod_{i=1}^{n} P(x_i|M_1 + M_2 \,\text{and}\, x_i \,\text{in}\, X'). \tag{4.15}$$

4.1.3 Likelihood Function within the MadWeight Framework

The main difficulty of this method is the integration in equation 4.11 over all possible phase-space elements in Y' for a given experimental outcome. Thanks to the developed fast MC techniques this can be overcome. A dedicated software called MadWeight [58] calculates the integral in equation 4.11 for any given process that can be simulated with the MadGraph/MadEvent [59] multipurpose event generator. The squared matrix element provided by the generator is directly used to calculate so-called *"weights"* per event. MadWeight calculates the event weights in the following form [58]

$$W(x|\alpha) = \int d\phi(y) dq_1 dq_2 f_1(q_1) f_2(q_2) |M_\alpha|^2(y) w(x;y). \tag{4.16}$$

If we look at this formulation, we can see that it is similar to the the pdf formulation in the form of equation 4.11 with the normalization and definition of phase-space left to the user. Thus the weight returned by MadWeight is

$$W(x|\alpha) = \int \frac{d\sigma}{dy} w(x|y) dy,$$

where $w(x|y)$ is what the user has provided as the transfer function, i.e. very often just a unit-normalised function (in which case we should write $w'(x|y)$.

If we re-write the likelihood function using equation 4.14 with the weights returned by MadWeight for two non-interfering processes, we obtain

$$\begin{aligned} P(x|M_1 + M_2 \text{ and } x \text{ in } X') = & \frac{\sigma_1\varepsilon_1}{\sigma_1\varepsilon_1 + \sigma_2\varepsilon_2} N' W_1(x|M_1 \text{ and } x \text{ in } X') + \\ & \frac{\sigma_2\varepsilon_2}{\sigma_1\varepsilon_1 + \sigma_2\varepsilon_2} N'' W_2(x|M_2 \text{ and } x \text{ in } X'). \end{aligned}$$

Since $\varepsilon\sigma$ terms are the relative probability for each process, they are the same as the ones in the normalization terms ($N' = \frac{1}{\sigma_1\varepsilon_1}$ and $N'' = \frac{1}{\sigma_2\varepsilon_2}$) by construction of the analysis, thus they cancel out. The formulation can thus be simplified as

$$P(x|M_1 + M_2) = \frac{1}{\sigma_1\varepsilon_1 + \sigma_2\varepsilon_2} W_1(x|M_1) + \frac{1}{\sigma_1\varepsilon_1 + \sigma_2\varepsilon_2} W_2(x|M_2). \tag{4.17}$$

The corresponding likelihood function for a set of observed events is therefore defined as

$$L(\{x_i\}|M_1 + M_2 \text{ and } x_i \text{ in } X') = \prod_{i=1}^{n} P(x_i|M_1 + M_2). \tag{4.18}$$

Note that if the transfer function has been provided as a unit-normalised function, then one is neglecting the function $\varepsilon(y)$ in equation 4.12.

4.1.4 Construction of the Transfer Functions

In equation 4.12, $w(x|y) = \varepsilon(y)w'(x|y)$ must be known for any y in Y' and any x in X'. In the simplest case of a single final state object, one can construct it with the help of MC by simulating samples of single objects events for all y values. Then the function $w(x|y)$ can be obtained for each x value in X', either in bins or as a probability density function analytically parametrized. Note that the efficiency function $\varepsilon(y)$ in equation 4.12 should be also accounted for.

In case of final states with non-correlated multiple objects, it is common to factorize the transfer functions. Muon reconstruction algorithms, as described in chapter 2, are such that for di-muon final states it is safe to write the transfer functions as the product of two single muon transfer functions. Thus we can write the transfer functions for the di-muon final state as:

$$w'(x_1, x_2|y_1, y_2) = f(x_1|y_1)f(x_2|y_2)$$

$$w(x_1, x_2|y_1, y_2) = \varepsilon(y_1)f(x_1|y_1)\varepsilon(y_2)f(x_2|y_2) \tag{4.19}$$

where $f(x_1|y_1)$ (and $f(x_2|y_2)$) is the unit normalised resolution function for a single muon, $\varepsilon(y_1)$ (and $\varepsilon(y_2)$) is the efficiency. This formulation is valid as long as the reconstruction of every individual object is not affected by the reconstruction of any other object.

In a more complex final state, the transfer function should be written by taking care of the correlation between final state objects, since one can have an effect on the experimental outcome of the other. It is always useful to check the possible additional effects due to mis-reconstruction in the assignment of reconstructed object to partons. We will come to this point again in the section of the validation with MC tests.

4.2 Statistical Approach

Once the proper likelihood function is built, it can be used in the determination of the set of unknown parameters. If we consider $q\bar{q} \to Z \to l^+l^-$, the model M is characterized by the parameters M_Z, Γ_Z, spin and parity. This implies, for instance, one can determine each of these underlying parameters by maximizing the likelihood function corresponding to a given set of observed events, once the event kinematics are known.

If we introduce in equation 4.18 a parameter μ, which is a cross-section modifier for a BSM process to be searched for, then the likelihood function for the signal plus background hypothesis is

$$L(\{x_i\};\mu,S,B) = \prod_i^n \left(\frac{\mu W_S(x_i;S)}{\mu\sigma_S\varepsilon_S + \sigma_B\varepsilon_B} + \frac{W_B(x_i;B)}{\mu\sigma_S\varepsilon_S + \sigma_B\varepsilon_B} \right). \tag{4.20}$$

Here, S is the abbreviation of the signal model and signal parameters, and B is the background model and relevant model parameters in the weight calculation. The terms W_S and W_B are the weights returned by MadWeight under the signal and background assumptions, respectively, for every selected and measured event x_i.

Although the treatment of systematic uncertainties will be explained in section 4.2.4, for now we denote as θ_j, a set of parameters whose values are affected by systematic uncertainties and that will be called nuisance parameters. In order to take into account such uncertainties, the likelihood function in eq. 4.20 will be modified and become also a function of the nuisance parameters $L(\{x_i\};\mu,\theta_j,S,B)$.

The likelihood function can be used to determine the model parameters for signal or background with observed data.

4.2.1 Test-Statistics and Parameter Estimation

The likelihood function $L(\{x_i\}; \mu, \theta_j, S, B)$ can be used to estimate the signal and background model parameters by finding the values of the μ and θ parameters that maximize the likelihood. The procedure is called the Maximum Likelihood (ML) method. For handling easier the very small numbers involved, one typically maximizes the logarithm of the likelihood function. The parameters that maximize the log-likelihood are called the Maximum Likelihood Estimate (MLE). The maximum likelihood estimators, can give biased values of parameters, especially in a statistically small sample. Therefore the method should be checked carefully to verify possible biases.

We begin by using the maximum likelihood method with an un-binned data set to estimate model parameters and signal strength μ to search for heavy di-muon resonances. The likelihood function constructed out of signal and background pdfs can also be used to compute the significance of the observed data with respect to the signal hypothesis and to exclude the signal cross-section values. These tasks can require large amounts of CPU time. In order to save time, we use the so-called “Asymptotic” formulae for the Profile Likelihood Ratio (PLR) test statistic [60]. Later, we make the comparison in the significance between the accurate numerical calculation with toy-MC experiments and the asymptotic results. We only employ a numerical calculation for the upper limit on the signal strength parameter.

As anticipated earlier, in the hypothesis testing problem, the Neyman-Pearson lemma states that, the best discriminating variable , called “test statistic”, between two alternative hypotheses is the likelihood ratio. The general expression for the likelihood ratio to calculate the significance that includes the nuisance parameters can be given by the PLR as

$$\lambda(\mu) = \frac{L(\{x_i\}; \mu, \hat{\hat{\theta}})}{L(\{x_i\}; \hat{\mu}, \hat{\theta})}. \tag{4.21}$$

The single hat indicates the value that maximizes the likelihood when all the parameters are left free, while a double hat indicates the value of the parameter that maximizes the likelihood where one or more parameters, which are those indicated without hats, in the likelihood are set to certain values. Actually, the test-statistic, as defined in the asymtotic formulae of ref [60], is

$$q(\mu) = -2ln\lambda(\mu). \tag{4.22}$$

But, in terms of discriminating power, this one is completely equivalent to the one in equation4.21, given that $q(\mu)$ is a monotonous function of $\lambda(\mu)$.

4.2.2 P-value and the Maximum Significance

The aim of the analysis is to discover a (positive) BSM signal in the available set of events by rejecting the alternative background-only hypothesis, which corresponds to $\mu = 0$. The test-statistics defined in eq. 4.22 thus takes the form

$$q(0) = -2ln\frac{L(\{x_i\}; \mu = 0, B, \hat{\hat{\theta}})}{L(\{x_i\}; \hat{\mu}, S, B, \hat{\theta})}. \tag{4.23}$$

The test is based on the *background-only* hypothesis against the alternative *signal+background* hypothesis. Note the dependence of q(0) on $\hat{\mu}$. If the likelihood is maximized at negative values of μ that does not bring any information about the test. It could be an under fluctuation of data with respect to values expected in the background-only hypothesis. Therefore the test statistics will be redefined as

$$q(0) = \begin{cases} -2ln\lambda(\mu = 0) & \hat{\mu} \geq 0 \\ 0 & \hat{\mu} < 0 \end{cases} \tag{4.24}$$

To verify the presence of a signal in the data, one has to compute the so-called “p-value” of the test. This number represents the probability that a given hypothesis yields a value of the test statistics as or more extreme than the one computed on the observed data. Using the test-statistics definition, the p-value reads

$$p - value = \int_{q(0)_{obs}}^{\infty} f(q(0)|0)\, dq(0), \tag{4.25}$$

where $q(0)_{obs}$ is the observed test statistics, $f(q(0)|0)$ is the pdf of the test-statistics q(0) distribution obtained in background-only experiments.

In particle physics the common approach is to convert the p-value to an equivalent significance, basically to a “z-score” which is defined as the number of standard deviations in the upper-tail probability of a standard Gaussian distribution. It can be constructed as a double-sided and a one-sided tail probability. In our analysis we use the one-sided tail probability distribution. One can give the results in terms of a p-value or a z-score by converting one to another. Z=5σ means 5 standard deviations observed from the expectation and usually claims a discovery. The p-value of such an observation corresponds to $p = 2.87.10^{-7}$.

An approximate solution for calculation of significance can be found in Asymptotic approach [60]. It is proven that, under certain assumptions according to Wilk’s [61] theorem the test statistic is asymptotically χ^2 distributed. In this case, the significance is directly linked to the size of the likelihood ratio as

$$z - \text{score} = Z = \sqrt{q(0)}. \tag{4.26}$$

4.2.3 Upper Limit on the Parameter of Interest

In case of observed data showing compatibility with the background-only hypothesis, thus rejecting the alternative signal+background hypothesis, one would be interested in setting an upper-limit on the parameter of interest. To compute an upper limit on the signal strength, we consider the test-statistics $q(\mu)$ in equation 4.22, for hypothesized μ values to be tested with the observed data set. For setting an upper limit the proper test statistic is:

$$q(\mu) = \begin{cases} -2ln\lambda(\mu) & \hat{\mu} \leq \mu \\ 0 & \hat{\mu} > \mu \end{cases} \tag{4.27}$$

where $\lambda(\mu)$ is the profile likelihood ratio as defined in the equation 4.21. If the observed data set shows incompatibility with tested μ values, in this case $\hat{\mu} > \mu$, the test will be equal to zero. One needs to quantify the level of disagreement of the observed data with hypothesized μ value. This time the pdf of the test statistics values under the signal+background hypothesis is needed, $f(q(\mu)|\mu)$, and one must find the value of μ corresponding to a given probability, called the confidence level of the exclusion, that a signal+background experiment would have given an outcome as or more incompatible than the outcome of the real experiment. The relevant p-value is in this case given by the following expression:

$$p_\mu = \int_{q(\mu)_{obs}}^{\infty} f(q(\mu)|\mu)\, dq(\mu). \tag{4.28}$$

A standard 95% Confidence-Level (CL), namely a one-sided confidence interval (upper limit) is obtained by solving for $p_\mu = 0.05$. The computation of equation 4.25 and 4.28 requires the sampling distribution of the test statistics. Both integrals can be calculated to an approximation, the solutions exist in the literature with the Asymptotic approach [60].However, in our analysis we obtain the upper limit on the μ signal strength with a Monte Carlo technique, by generating the number of toy experiments.

4.2.4 Treatment of Systematic Uncertainties

It is important to check the analysis with respect to all possible effects of instrumental and theoretical uncertainties. There are many sources of uncertainties affecting the fitted model parameters. For example, the underlying theoretical model description and measured physical quantities are known within uncertainties.

In order to account for all systematic effects, a hybrid Bayesian- Frequentest approach is followed [62]. The systematic uncertainties are modeled via so-called "*nuisance parameters*" [63], assuming that the information on these uncertainties are available in the form of prior distributions. The prior pdfs corresponding to each nuisance parameter are then introduced as multiplicative factors in the likelihood function.

The "log-normal" pdfs [64] are used to describe the nuisance parameters. A log-normal distribution is obtained with a random variable whose logarithm follows a normal distribution. A pdf for the log-normal distribution is

$$P(\psi) = \frac{1}{\sqrt{2\pi\sigma^2}}\frac{1}{\psi}exp\left(-\frac{(ln\psi - \mu)^2}{2\sigma^2}\right). \tag{4.29}$$

The p-value computation is performed using a Monte Carlo method of generating samples of toy experiments which referred also as toy-MC experiments. Each toy-MC experiment is generated using a given set of nuisance parameters each extracted from its pdf. The uncertainty in the nuisance parameters is effectively taken care by varying the MC data set in each toy experiment. In principle, having an ensemble of toy experiments in which each is characterized by values of the nuisance parameters extracted from the estimated pdfs will be approximating the effects of the systematic uncertainties.

The approximate and numerical solutions are used in the computation of discovery significance while the computation of the upper limit at the desired confidence interval (95% CL) is performed numerically.

Since the determination of nuisance parameters depends on the relevant measurements and underlying dynamics of the analysis, the effect of nuisance parameters on the observables will be discussed in chapter 6. After the discussion of all possible sources of systematic uncertainties, the likelihood function with nuisance treatment and the likelihood fitting procedure will be presented therein.

Chapter 5

Validation of the Method with Monte-Carlo Generated Events

In order to use the likelihood-based analysis method described in the previous chapter in an experimental measurement or in a search analysis, a detailed validation is necessary. Therefore, this chapter will be dedicated to validation studies. A possible sensitivity gain that the matrix element approach could bring in comparison to a classical analysis, in which a peak is searched for in a smooth background, is investigated in depth.

The first section is dedicated to the validation of the likelihood function defined in the previous chapter with simulated signal and background events. As described in chapter 1, a benchmark model would be a narrow, high-mass Z' resonance decaying to two muons. The main background to this signal process is Drell-Yan production. Therefore all validation studies were carried out using the signal events $pp \to Z' \to \mu^+\mu^-$, and the Drell-Yan background events leading to the same final state. We consider the generic Sequential Standard Model as the main signal model to test. After describing how the underlying model parameters can be estimated using the maximum likelihood method in section 5.2, we compare the classical peak-search and matrix-elements-based analysis approaches using toy-MC experiments. Only statistical uncertainties are discussed in this chapter.

5.1 MC Event Generation, Selection and Normalization

As described in chapter 4, the likelihood can be written in the form of equation 4.12, where the definitions of Y' and X' should be established by considering the analysis requirements. Throughout the validation studies we assume a sequential standard model Z' with a mass of $1\text{TeV}/c^2$. Given the model, the width of the resonance is taken to be 3% of its mass and a width of 30 GeV is assumed for the signal.

The MadGraph MC generator is used for fully exclusive signal and background event production. As described before, Y' should be loose enough that any event outside will never end up in X'. Considering a signal of $1\text{TeV}/c^2$ mass, the 600-1400 GeV/c^2 invariant mass range is chosen at generator level for the Y' space, while restricting the analysis selection range to the 800-1200 GeV/c^2, which is driven by the mass resolution of the detector.

The simulation of detector effects in an experimental set-up is highly CPU demanding. In addition, the maximization of the likelihood function can also be CPU expensive if the number of parameters in the likelihood is high. In order keep the CPU demands within reasonable levels, we consider a limited set of model parameters and we apply simplified simulation of detector effects on the generated events.

A 5% smearing on the muon energy is introduced on the generated MC events. Since the CMS muon detection system extends up to $|\eta|$ =2.4, generated muons were restricted to $|\eta|$ <2.4, and a minimum of 20 GeV/c of transverse momentum is required. The transfer functions are built accordingly, to include the detector energy smearing effect on the parton-level generated particles. In other words, the muon energy transfer function is parametrized as a function of the generated muon energy in the form of a Gaussian distribution with a width equal to 5% of its mean value. Because of the extremely good particle direction resolution

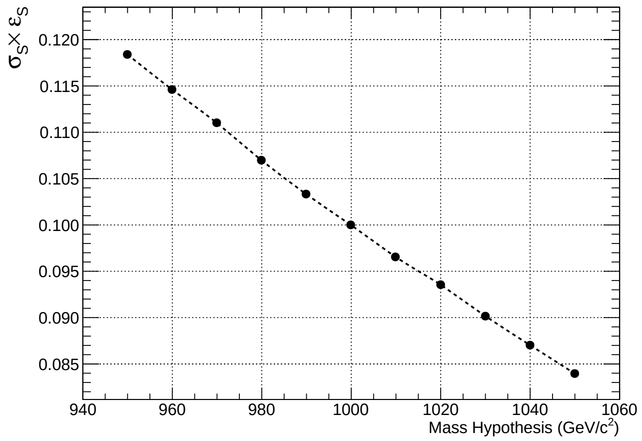

Fig. 5.1: The $\sigma_S \times \varepsilon_S$ normalization factor used in the likelihood normalization with respect to the signal mass hypothesis.

of the CMS detector, the η and ϕ of the produced muons are left to be the same as at the generator level during the smearing. In practice, the Dirac delta function is assumed for the η and ϕ angle transfer functions.

In the analysis selection, 45 GeV/c of transverse momentum is required on the muon transverse momentum after smearing the muon energy. Opposite charge is also required when pairing the smeared objects. By restricting the analysis selection to muon pairs with an invariant mass in the range 800-1200 GeV/c^2, we make sure that the probability that events outside the generator-level space are selected in the analysis is with excellent approximation equal to zero.

Figure 5.1 shows how the normalization term $\sigma_S \times \varepsilon_S$ changes with respect to the considered signal mass hypothesis by introducing the analysis selections on smeared signal events. Here, σ_S is the signal production cross-section in Y' and ε_S is the efficiency of selecting a set of signal events fulfilling the analysis requirements.

Figure 5.2 shows the logarithm of the likelihood value log-L(x;M) as a function of the signal mass hypothesis of 900, 980 and 1100 GeV/c^2.

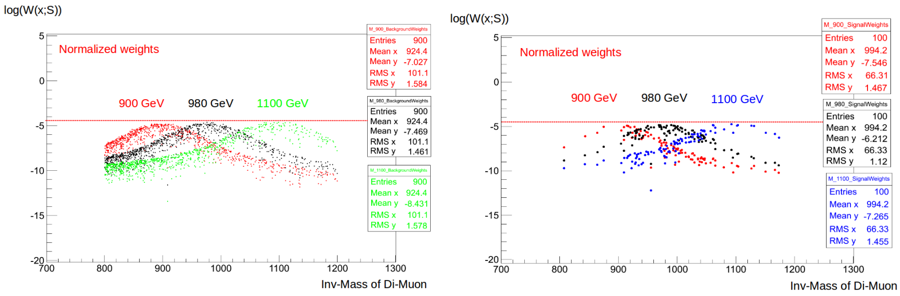

(a) **(b)**

Fig. 5.2: Logarithm of the likelihood function for signal mass hypotheses of 900, 980 and 1100 GeV/c^2 (a) with background events and (b) with signal events.

5.2 Parameter Estimation

We use the maximum likelihood method with unbinned data set to estimate the model parameters and signal strength μ. Equation 4.20 for a number of events *"n"* (smeared MC events or observed data) can be re-written in terms of the signal and background event fractions rather than event rates as

$$L(\{x_i\}; f_S, S, B) = \prod_i^n \left(\frac{f_S W_S(x_i; S)}{\sigma_S \varepsilon_S} + \frac{(1 - f_S) W_B(x_i; B)}{\sigma_B \varepsilon_B} \right), \tag{5.1}$$

where f_S is the signal fraction and equals to:

$$f_S = \frac{\mu \sigma_S \varepsilon_S}{\mu \sigma_S \varepsilon_S + \sigma_B \varepsilon_B}. \tag{5.2}$$

For the purpose of validation, we use a set of selected signal and background events distributed in the invariant mass range 800-1200GeV/c^2. In each set of event, called pseudo experiment, the signal fraction is fixed to 20%, though different number of events are used for testing the method.

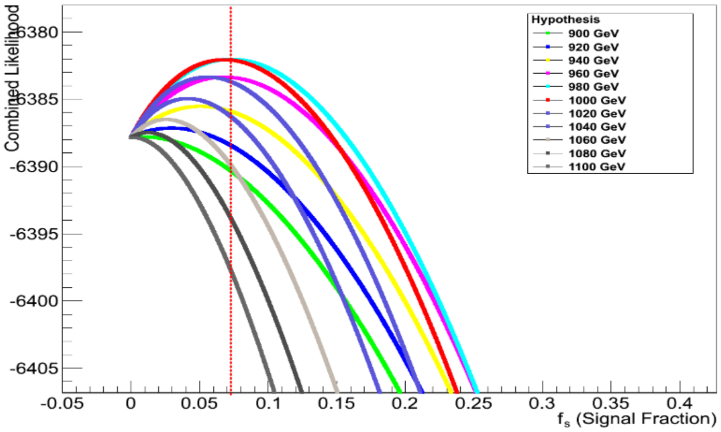

Fig. 5.3: Logarithm of the likelihood functions with respect to the signal fraction under different signal mass hypotheses. This procedure is followed to find the (best) estimates of the signal fraction (f_S) and the signal mass (M_S) values.

In the likelihood maximization, the signal fraction is estimated with respect to different signal mass hypothesis. The values of the resonance mass (M_S) and the signal fraction (f_S) that maximize the likelihood function are taken to be the estimated parameter values in the experiment. Figure 5.3 shows the values of the likelihood function as a function of the signal fraction, under different signal mass hypotheses adopted in a single experiment. The signal events used in the pseudo experiment are distributed around the resonance mass of 1TeV. The best estimates for f_S and M_S correspond to the ones having the highest (maximum) value of the log-likelihood, which are called the estimated (or sometimes fitted) values. As can be seen, for this pseudo experiment the best estimate for M_S is compatible with the input signal mass value of 1TeV.

The results obtained with this matrix element method are now compared to those obtained with a classical peak-search approach as it is the current analysis approach of the CMS experiment [65] to check whether a sensitivity gain is possible. In the classical approach the observed invariant mass distribution is compared to the ones expected under the background-only and signal+background hypotheses. Figure 5.4 shows the invariant mass distribution of a very large number of simulated signal and background events after smearing. Fits to these distributions, obtained with RooFit [66] data modeling package, are also shown on figure 5.4 and are used as models of the background and signal shapes. The signal model P_S is chosen to be a Breit-Wigner function convolved with a Gaussian function, while the chosen background model P_B consists of an exponential function. The signal and background models are defined as

$$P_S(m) = \text{Gauss}(m; M_S, \sigma_S) \otimes \text{Breit-Wigner}(m; M_S, \Gamma), \tag{5.3}$$

$$P_B(m) = N \exp^{am} m^b, \tag{5.4}$$

where m is the invariant mass of the di-muon events, M_S, Γ_S, σ_S are the signal mass (mean), width of the signal and the standard deviation of the Gaussian function that describe the signal model. In equation 5.4, N is the normalization factor, which does not have any impact on the shape, a and b are the two parameters that are determined by the fit which describe the background model. The values of the fitted parameters for signal and background models are shown on figure 5.4 separately.

The likelihood function built for the peak-search analysis for signal+ background model is

$$\begin{aligned} L(\{m_i\}; f_S, M_S, \Gamma_S, \sigma_S, a, b) = \prod_i^n &(f_S P_S(m_i; M_S, \Gamma_S, \sigma_S) + \\ &(1 - f_S) P_B(m_i; a, b)). \end{aligned} \tag{5.5}$$

In order to test the sensitivity of the methods, we estimate the model parameters with both analysis techniques for the same set of toy-MC experiments. Figure 5.5 shows the estimated signal fractions obtained in 400 pseudo experiments containing each 20 background and 5 signal events. The points indicate the mean of the estimated signal fractions

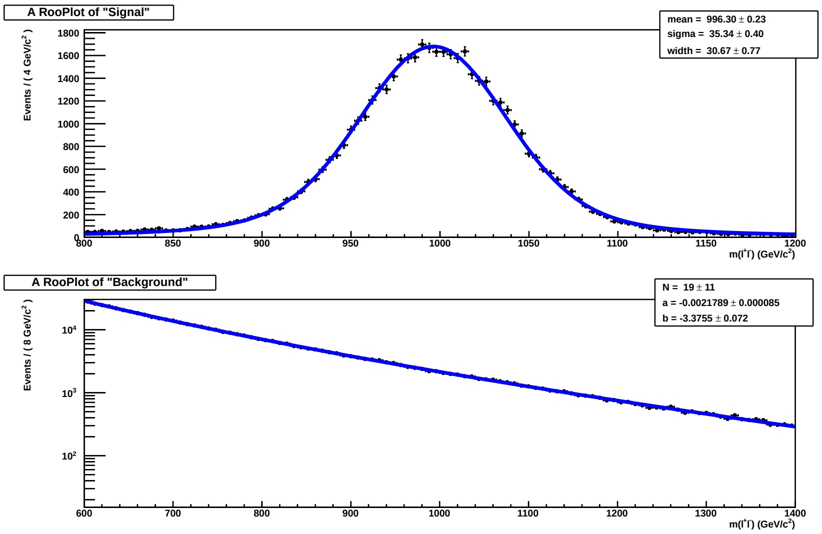

Fig. 5.4: The signal and background event distributions where fitted shape pdfs for each distribution are shown in blue curves and are used for modeling the signal and background.

for each mass hypothesis. The error bars indicate the RMS of each distribution, and therefore can tell about the sensitivity of the parameter estimation with both analysis methods. It can be seen that the likelihood estimators correspond to the correct signal fraction at the correct mass value with both analysis methods.

5.3 Hypothesis Testing

The two analysis approaches are compared in terms of a possible sensitivity gain. The procedure described in chapter 4 is adopted where the likelihood function for the matrix element approach is the one in equation 4.20 and for the peak-search approach in equation 5.5 are used in the profile likelihood ratio test statistics. The $q(0)$ test statistics is calculated to obtain the z-score according to the asymptotic approach (see eq. 4.26) for two analyses.

Figure 5.6 shows the mean of estimated significance (z-score) as a func-

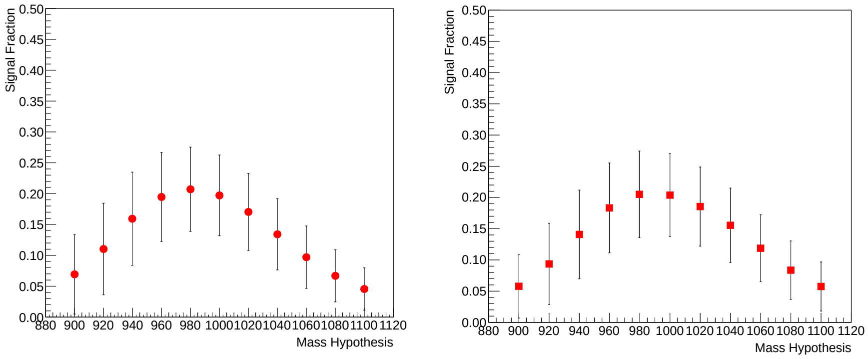

(a) **(b)**

Fig. 5.5: The estimation of signal fraction with respect to hypothesized signal mass points used in the signal model (for details see text). The figure on the left-hand side (a) shows the result obtained with the shape analysis, while the figure on the right-hand side (b) is the result of the Matrix Element Likelihood Method .

tion of fixed hypothesized signal mass points obtained in 400 pseudo experiments containing each 20 background and 5 signal events. The error bars indicate the RMS of each distribution, the statistical errors on the points are small (upto 5% of RMS) and not shown on the figures.

The significance obtained with the matrix element approach is found to be 10% higher than the one obtained in the peak-search analysis at the expected signal mass, thus, the sensitivity of the method is found to be improved approximately by 10%. On the other hand, the widths of the significance distributions at any given mass value are the same in both analyses.

In an experiment, one does not know a priori the signal mass and the signal event rate, since our knowledge of these parameters are limited by the description of the theoretical models being tested. Therefore, a scan in the parameter space is usually necessary for the measurements. If we perform the analysis with a simultaneous unbinned likelihood fit with respect to the hypothesized signal mass points and signal fraction, we

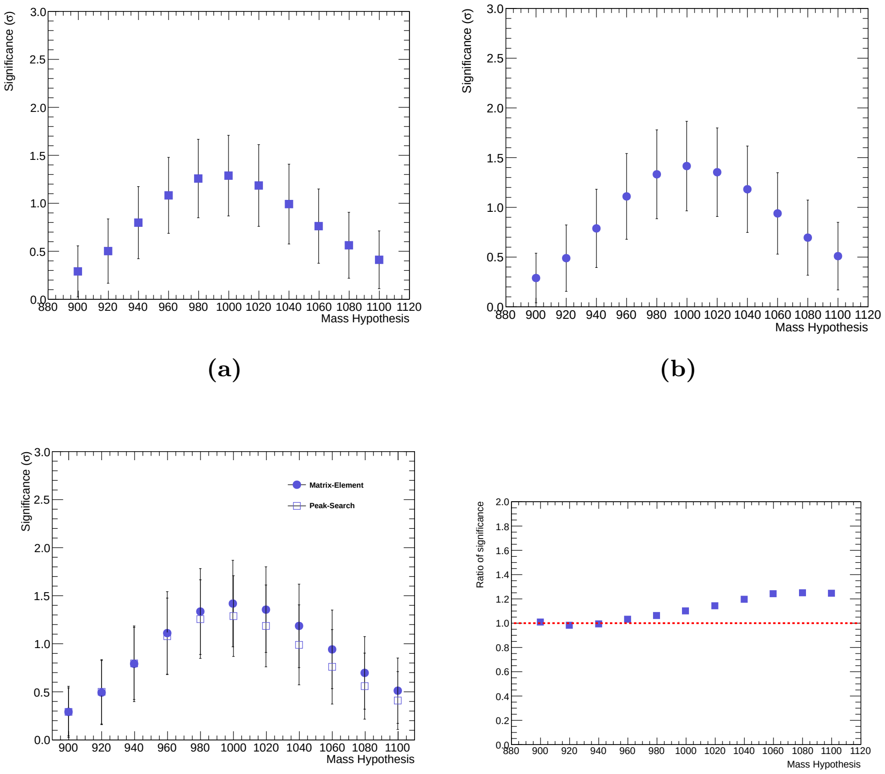

(a) **(b)**

(c) **(d)**

Fig. 5.6: The mean significance (z-score) with respect to hypothesized signal mass points. The figure on the top-left (a) shows the result with the shape analysis while the figure on the top-right (b) is the result obtained with the Matrix Element Likelihood Method The figure on the bottom-left is the results of both analyses shown together whereas the figure on the bottom-right is the ratio of the mean significance of Matrix Element Likelihood Method to peak-search analysis approach.

would estimate both parameters at the same time for a given data set. Therefore, in another test, we compute the results with both analysis approaches by taking the signal mass and the signal fraction as the parameters of interest in the likelihoods. Figure 5.7 shows the obtained results for the estimation of the (best) signal mass M_S with the Matrix Element Likelihood Method using different sets of statistical samples as indicated on the figure.

Figure 5.8 shows the estimated signal fractions in the simultaneous fits for different toy-MC experiments using different statistical samples; figures 5.11 and 5.12 show the results obtained in the simultaneous fits with the shape analysis for the estimation of signal mass and signal fraction.

Maximum likelihood estimators can be biased, although the bias is expected to vanish in the limit of large samples. From figure 5.8 we can see this bias effect. Clearly the results are biased when the low statistical samples are used while fitting. Hence, the simultaneous estimation of the parameters in the likelihood fit tends to give biased estimates for the signal fraction. This bias effect is more pronounced in the low-statistic experiments. As shown in figure 5.5, the results obtained with fixed mass hypotheses show no bias in such a test. In figure 5.9, the mean estimated signal fraction, obtained in the simultaneous fit, is plotted as a function of the type (named “set-up” in the label of the horizontal axis) of pseudo-experiments corresponding to the four different types used for the results of figure 5.8. The error bars are the RMS of each distribution. It can be seen that the result of the low statistics in the estimation of the mean signal fraction is more biased than the one obtained in higher statistical samples. This shows that if the statistic is increased sufficiently, the likelihood estimator tends to give more accurate results; the effect depends on the sample size, as expected.

Figure 5.10 is a good way of visualizing the estimated parameters. The distribution is obtained by performing 100 toy-MC experiments composed of 20 signal and 80 background events. As can be seen, the mean estimated values of the distribution for the signal fraction and the corresponding estimated mass value are in agreement with the expected input values.

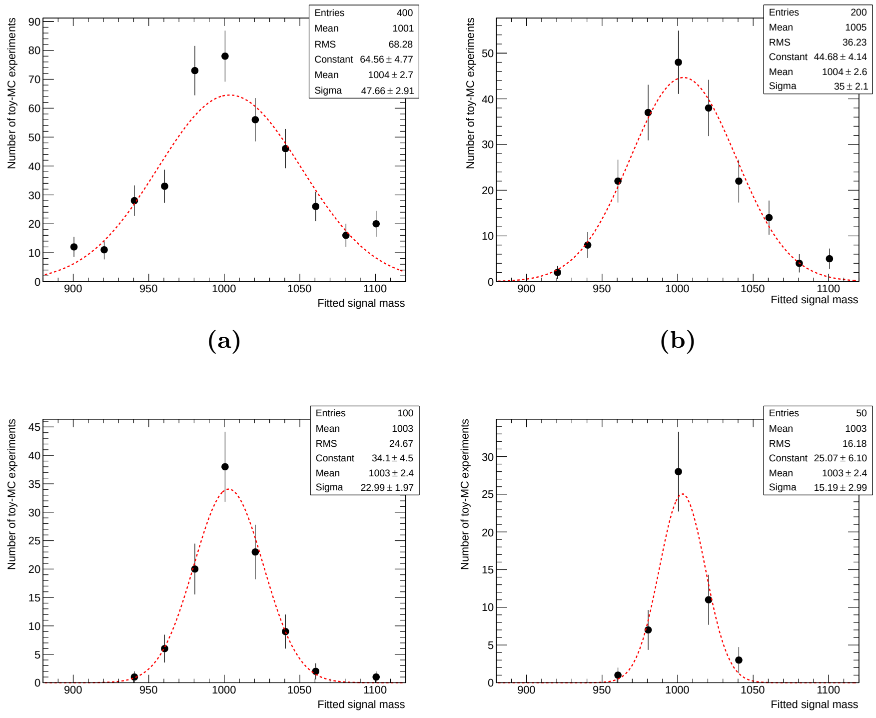

(a) **(b)**

(c) **(d)**

Fig. 5.7: The results of simultaneous fits for the estimation of the best mass with different sets of statistical samples using the Matrix Element Likelihood Method : (a) for toy-MC experiments of 20 background and 5 signal events, (b) for toy-MC experiments of 40 background and 10 signal events, (c) for toy-MC experiments of 80 background and 20 signal events, (d) for toy-MC experiments of 160 background and 40 signal events. The red dotted lines indicate the Gaussian fits to each distribution obtained. The error bars indicate the statistical uncertainties.

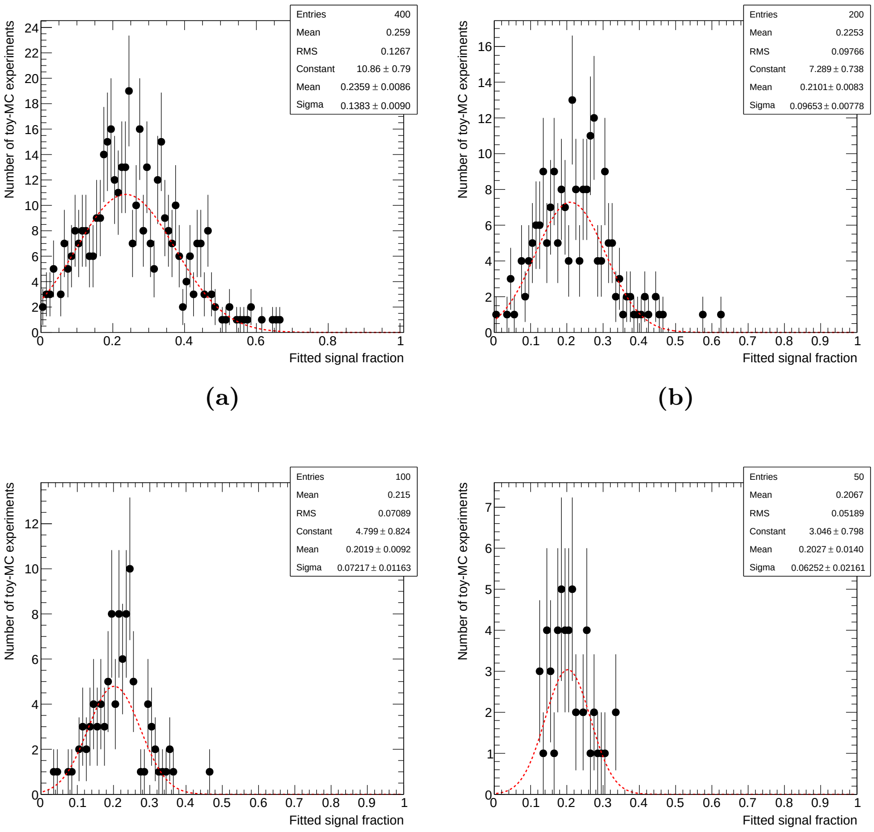

(a) **(b)**

(c) **(d)**

Fig. 5.8: The results of simultaneous fits for the estimation of the signal fraction with different sets of statistical samples using the Matrix Element Likelihood Method : (a) for toy-MC experiments of 20 background and 5 signal events, (b) for toy-MC experiments of 40 background and 10 signal events, (c) for toy-MC experiments of 80 background and 20 signal events, (d) for toy-MC experiments of 160 background and 40 signal events. The red dotted lines indicate the Gaussian fits to each distribution obtained.

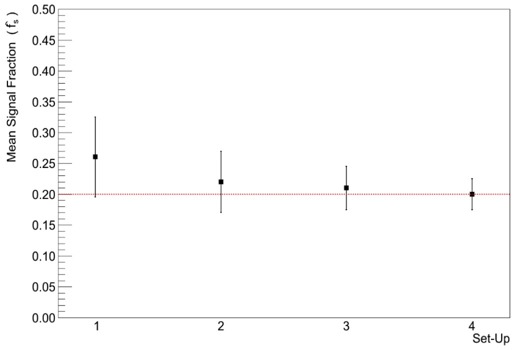

Fig. 5.9: Mean of the estimated signal fraction in the simultaneous fits with different set of toy-MC experiments used with the Matrix Element Likelihood Method . The x-axis refers to the four types of toy-MC experiments performed in the simultaneous fits with different statistical samples (see fig. 5.8).

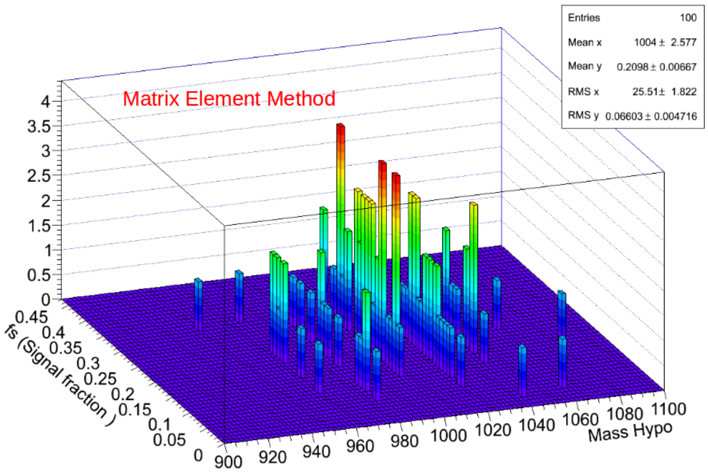

Fig. 5.10: The results of the simultaneous fits for the estimation of the signal mass vs. the signal fraction with 100 pseudo-experiments based on 80 background and 20 signal events.

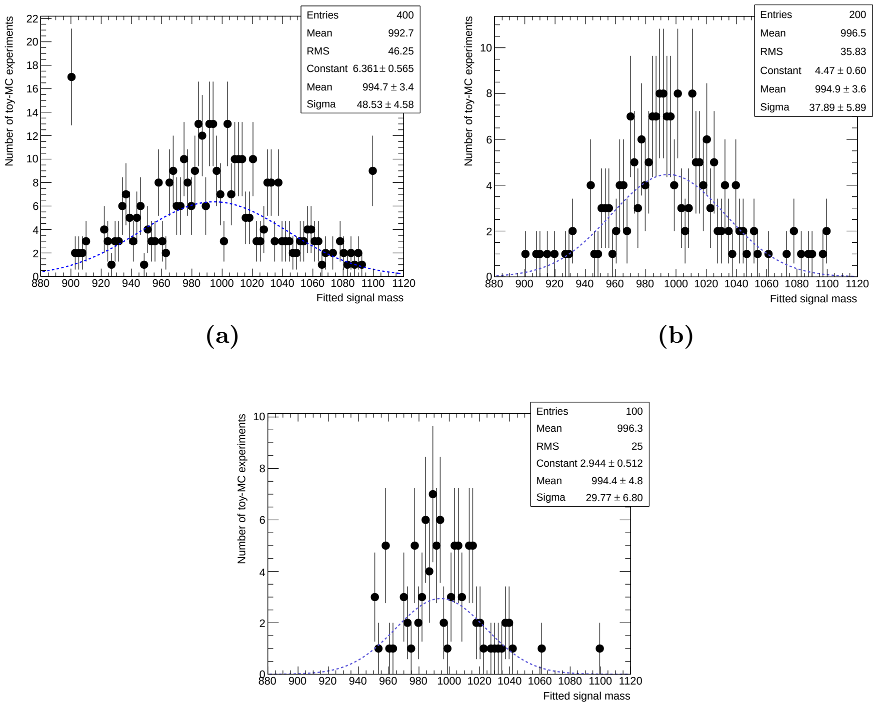

(a) **(b)**

(c)

Fig. 5.11: The results of simultaneous fits for the estimation of the best mass with different sets of statistical samples using the shape analysis: (a) for pseudo-experiments of 20 background and 5 signal events, (b) for pseudo-experiments of 40 background and 10 signal events, (c) for pseudo-experiments of 80 background and 20 signal events. The dotted blue lines indicate the Gaussian fits to each distribution obtained. The error bars indicate the statistical uncertainties.

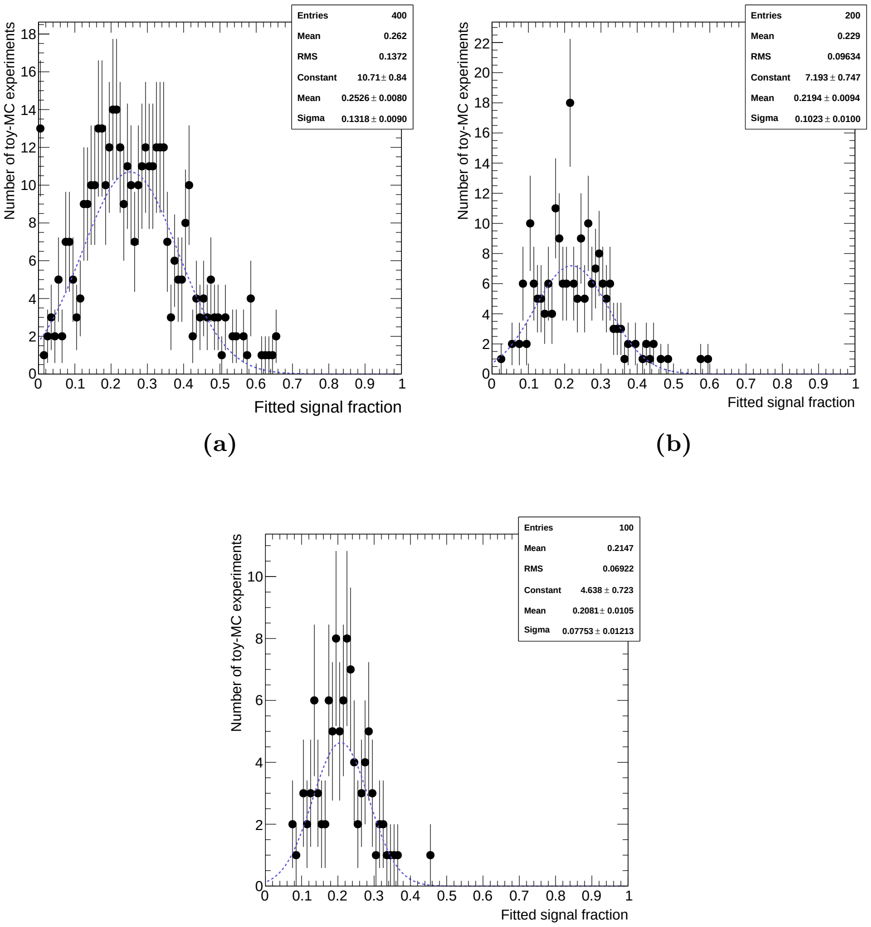

(a) **(b)**

(c)

Fig. 5.12: The results of the simultaneous fits for the estimation of the signal fraction with different sets of statistical samples with the shape analysis: (a) for toy-MC experiments of 20 background and 5 signal events, (b) for toy-MC experiments of 40 background and 10 signal events, (c) for toy-MC experiments of 80 background and 20 signal events. The dotted blue lines indicate the Gaussian fits to each distribution obtained.

It is important to test the method with the background-only toy-MC experiments to verify the sensitivity of the analysis in the scenario of background-only events. Therefore, we make another test with 400 pseudo-experiments composed of 20 background-only events. The results of these tests can be seen in figures 5.13 and 5.14 with respect to fixed signal mass hypothesis. It is found that the mean estimated signal fractions with matrix element approach are 10-15% lower than the ones obtained with the peak-search analysis at low mass points, which builds confidence in the good properties of the matrix element approach in the sense that it does not increase the significance of an excess in both signal+background and background-only experiments.

5.4 Other Effects

5.4.1 Effect of the MC Integrator

In the Matrix Element Method, the calculation of likelihood function requires the numerical integration reported in equation 4.20. This integration is in practice not straightforward, and complicated MC techniques are used. Therefore, we further investigate this effect of the MC integration on the fitted results. Figure 5.15 shows this effect of the integration with the default MadWeight MC integrator, called Vegas [67], for one pseudo-experiment of 900 backround and 100 signal events. Each point in the x-axis corresponds to the number of integration points in the integration space. Fluctuations on the estimated significance are observed with respect to the number of integration points. However, fluctuations stabilize by increasing the number of points sufficiently. Therefore, we adopt the calculation corresponding to a sufficiently high number of phase-space points (1M). The average variation in the likelihood calculation due to integration points is observed to be less than 1%.

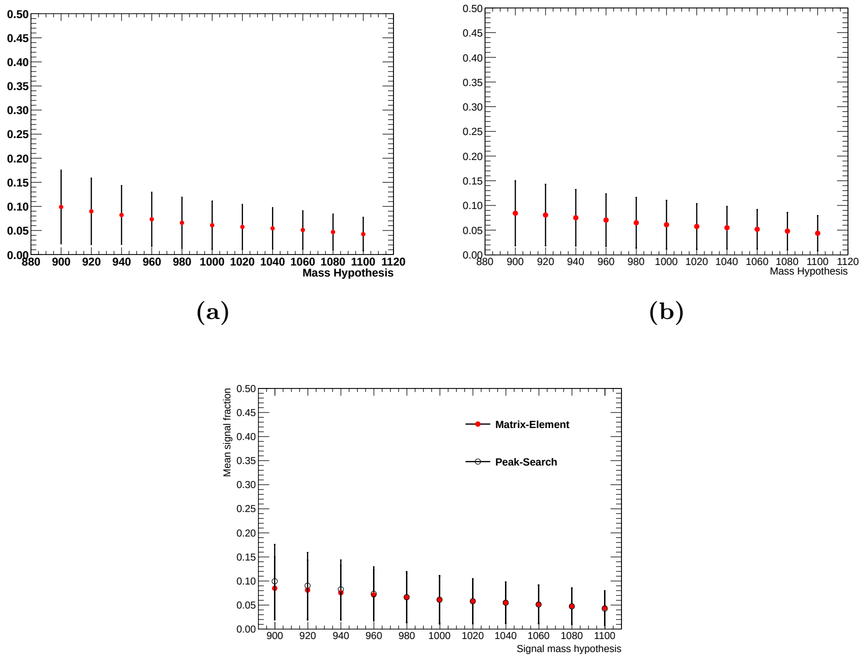

(a)

(b)

(c)

Fig. 5.13: The mean estimated signal fraction with respect to hypothesized signal mass points used in the signal model with toy-MC experiments of 20 background-only events. Figure on the upper-left (a) shows the result obtained with the shape analysis, while the figure on the upper-right (b) is the result of the Matrix Element Likelihood Method , the figure on the bottom (c) shows the two analysis results together. The error bars show the RMS of each distribution obtained.

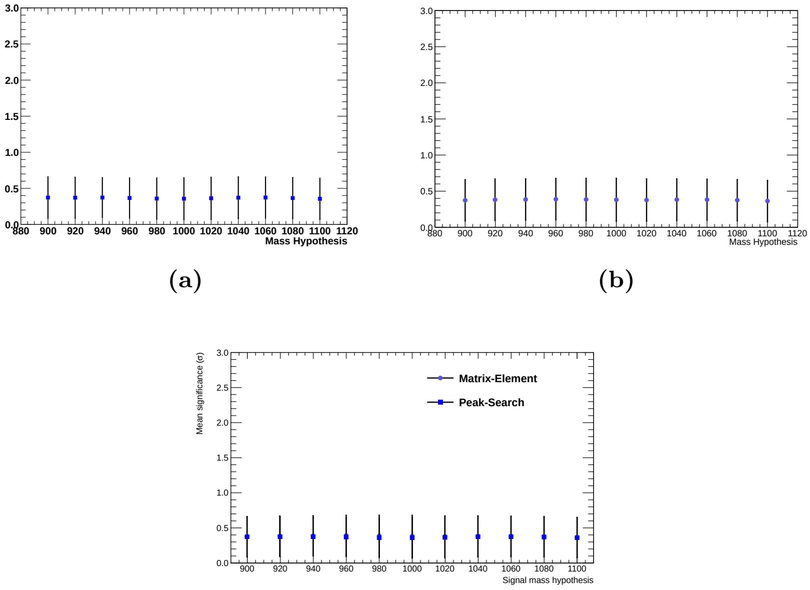

(a) (b)

(c)

Fig. 5.14: The mean significance (z-score) with respect to hypothesized signal mass with toy-MC experiments of 20 background-only events. The figure on the upper-left-hand side shows the result with the shape analysis while the figure on the the upper-right-hand side is the result estimated with Matrix Element Likelihood Method , the figure on the bottom (c) shows the two analysis results together. The error bars indicate the RMS of each distribution.

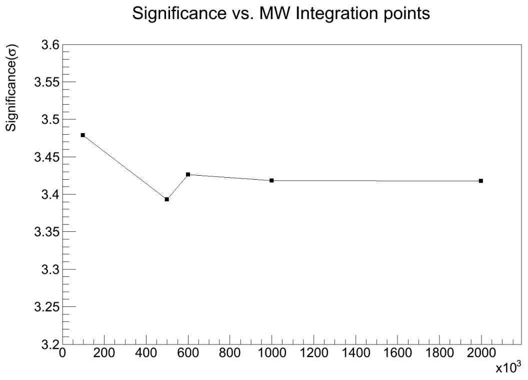

Fig. 5.15: Significance of the tests with respect to phase-space integration points.

5.4.2 Effect of the Detector Inefficiency

As described in chapter 4, the normalization of the transfer functions and therefore the detector effects are important features of the analysis. For instance any possible effect leading to an inefficiency (while reconstructing the final state objects, thus resulting to changes in the observables) should be taken into account in the transfer functions.

In equation 4.12, ε' is the overall normalization factor and plays a fundamental role in the parameter estimation. Neglecting this term would yield completely biased results during the parameter estimation. On the other hand, in hypothesis testing (searches), there is no problem because even if one neglects this term, he usually ends up with a test statistic that is a monotonous function of the likelihood ratio, which implies that the power of the test statistic is exactly the same as that of the likelihood ratio. An example is the $H \to ZZ^*$ to four lepton analysis performed by CMS [56], which has used $k_D = Ws/(Ws + Wb) = 1/(1 + \frac{(\varepsilon_b \sigma_b L_b)}{(\varepsilon_s \sigma_s L_s)})$.

On the other hand the $\varepsilon(y)$ stands for the detection efficiencies of the final state objects and only matters if $\varepsilon(y)$ varies over an interval centered around the experimentally measured value x and as large as a few times the experimental resolution. A special relevant case is one where the lepton p_T selection threshold is pushed to very low values like in the

$H \to ZZ^* \to 4l$ analysis [56]. Apart from this special case, the efficiency function in the transfer function can be considered constant, and in this case this factor goes out of the integration. In hypothesis testing it thus cancels out event by event in the likelihood ratio, whereas in parameter estimation it ends up in an overall constant multiplicative factor of the likelihood function, which thus plays no role.

In the CMS experiment, the detection efficiencies for reconstructed muons typically depend on η and p_T of muons. In order to verify the role of muon detection efficiencies on the analysis, we performed a simplified test by considering an experimental detector set-up where both muons are measured with a 60% efficiency in the end-cap and an 80% efficiency in the barrel by taking equation 4.19 where the transfer function (equal to a unit-normalized resolution function) multiplied by the efficiency. Our finding is that the constant detection efficiencies with respect to the η and p_T of muons do not play any role in the parameter estimation and in the the likelihood ratio test statistics, therefore supporting our statements previously made.

5.5 Conclusions of the Validation

In this chapter various tests with different statistical samples were performed for a search of a Z' vector boson as predicted by the sequential standard model scenario. All possible effects on an experimental measurement due to the detector set-up are introduced to the generated MC events and studied separately. These effects include the resolution of the detector, the detection efficiencies as well as the simplified analysis selection.

The likelihood function with joint signal and background pdfs is built accordingly, as described in chapter 4. As shown, the model parameters, of which fitted values define the underlying theoretical model, are estimated with a good accuracy even in cases where low statistics samples are used. This is the result of the analysis method, which is a rigorous way of constructing the likelihood function.

The number of free parameters in the likelihood are reduced by fixing some of the input model parameters. This procedure is necessary to lighten the computation of the weights over a multidimensional parameter space. By doing so, the estimation of signal fraction and signal mass were correctly obtained at their expected input values. On the other hand, a bias of possible statistical origin was seen in the simultaneous fit for the signal fraction and the signal mass. Although a higher signal fraction estimation than its input value is observed in the tests with low statistics, the erroneous estimation of the signal fraction disappeared when the number of events were increased in the samples while keeping the input signal fraction the same. The reduction in the free parameters during the likelihood fit, as shown in the results obtained with fixed mass hypotheses, is used to disentangle the bias effect. Conversely, the estimated mass values are compatible with the input in all tests.

A sensitivity gain of ≈10% in low statistics (and 20% in higher statistics) tests is observed in comparison to the peak-search analysis, depending on the sample size. Considering the fact that the same results are obtained with the peak-search analysis for the estimation of the parameters in a similar statistical approach, the analysis method is proven to be reliable.

It is found that the obtained results are also robust against MC integration techniques used during the weight calculation with sufficient integration points implemented in the MadWeight software. The role played by the overall likelihood normalization factor and by the efficiency term in the transfer function have also been discussed in detail.

The next chapter where this method is applied to CMS collision data, is performed in the light of these validation results.

Chapter 6

Application Studies with CMS Collision Data

After the description of the method and validation studies, this chapter focuses on the application of the likelihood method to the collision data gathered by the CMS detector during the LHC Run 1 at $\sqrt{s} = 7$ TeV. Section 6.1 is a brief description of the overall analysis strategy. After the description of the analysis selection, an auxiliary peak-search analysis is performed with the observed data set in order to restrict the search region. Section 6.4 is the discussion of the application of the method to the defined search window in the invariant mass of dimuon events. Finally, after addressing all possible sources of systematic uncertainties that can affect the measured parameters, the obtained results in terms of a local significance and an upper-limit on the cross section times branching fraction for the sequential standard model in the decay channel $Z' \to \mu^+\mu^-$ are presented.

6.1 Analysis Strategy

As described in chapter 1, classical peak-search analyses performed by the CMS experiment did not find any evidence of a resonance signal in the obtained invariant mass spectrum. Upper limits on the observable parameter space were set for various BSM signal models. A different approach with an independent analysis strategy might help to increase the sensitivity of the search. Therefore, the Matrix Element Likelihood Method is applied in an independent approach on the obtained di-muon events to search for a narrow resonance.

In order to use the Matrix Element Likelihood Method , the parameter space for signal and background should be defined. The computation of the weights required to establish a search (or a possible signal) region is a highly CPU expensive procedure to follow. Therefore, as a starting point, a faster analysis method is used to narrow down the search region where the highest (possibly an interesting) excess is seen. This also allows to construct the analysis region with confidence. Therefore we perform a scan in the obtained invariant mass spectrum with a classical peak-search analysis. After that, we construct the parameter space of the analysis accordingly. Namely, X' will be defined at this step, taking into the account the di-muon mass resolution at the boundaries of this mass window; Y' will be established as well. It follows the computation of weights for signal and background hypotheses, which requires the construction of the TFs via the parametrization of the detector resolution. After the discussion of all possible sources of systematic uncertainties, the obtained results are shown.

6.2 Event Selections

The analyzed data corresponds to $\sim 5fb^{-1}$ of integrated luminosity of the collision events produced by the CMS experiment during the LHC Run1 data taking. In order to obtain the final set of events used in the analysis, various cuts are introduced. Some of the cuts are applied on the single-muon events while others are applied on the di-muon events.

We apply the same selections as in the CMS analysis [68]. First of all, the trigger of selecting events is the lowest un-prescaled single muon trigger which have a $p_T > 40 GeV$ and to be within $|\eta| < 2.1$. The events are identified with high-purity tracks as the beam backgrounds are cut off. A good offline reconstructed primary vertex (PV) is required; the vertex must be associated with at least four tracks, it must be located within $|r| < 2cm$, and $|z|$ <24 cm of the nominal interaction point. This selection is very efficient for rejecting the cosmic muon background in an empty bunch crossing. Both muons are required to pass the "tight" selection criteria as described in chapter 2.

Both muons must be reconstructed as "global muon" and "tracker muon". The Tune-P (cocktail) algorithm should be used to in the momentum assignment. The offline reconstructed p_T should be greater than 45 GeV/c. The muons transverse impact parameter should be less than 2mm. Both muons should be isolated by requiring the tracker-only isolation cut to be less than 0.1. The global muon track associated with the identified muon must have at least measurements in 9 different layers in its fit. The global muon track must also include at least one measurement from each of pixel and muon system. The tracker-muon associated with the identified muon must be matched to segments in at least two muon stations. A common vertex fit compatibility is required on both muons in the events. To reduce the cosmic ray background the three-dimensional angle between two muons should be less than π-0.02 rad. The systematic uncertainties associated with all these requirements will be discussed in section 6.5.

6.3 An Auxiliary Peak-Search Analysis

A peak-search analysis (see ch. 5) is performed in order to restrict the search region on the di-muon invariant-mass spectrum obtained in the data. The pdf for the background model is obtained from the observed data while the signal model is described with MC events. Figure 6.1 shows the background pdf obtained by fitting the observed data: the shape parameters are defined by an exponential function as formulated

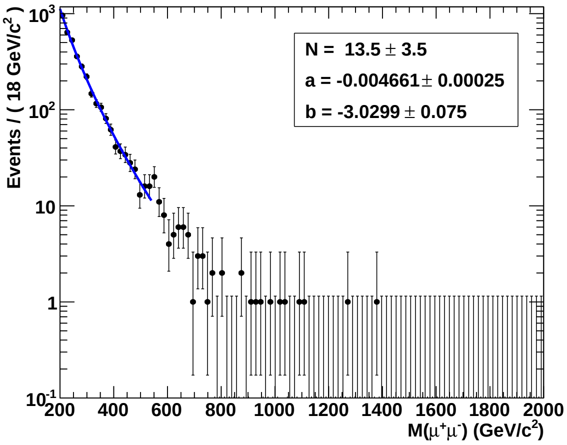

Fig. 6.1: The background pdf used in the description of the background shape by fitting the observed data at the low-mass region. The fitted parameters are obtained using RooFit package.

in equation 5.4. The shape parameters are obtained by only fitting the low-mass region of the invariant mass spectrum upto 540 GeV/c^2 where no excesses are seen. The region of the invariant mass spectrum above 540 GeV/c^2 is excluded while obtaining the background shape parameters. The signal shape parameters, on the other hand, are described by a Voigtian pdf (as defined in eq. 5.3) while taking the standard deviation equal to 50 GeV. Since the aim of the peak-search analysis is mainly to restrict the range of the invariant-mass spectrum, where the matrix-element analysis is performed, rather than drawing conclusions on the parameters, a likelihood fit based on the signal+background hypothesis (see eq. 5.5) has been performed alternative to background-only hypothesis without the treatment of the systematic uncertainties.

The PLR test statistic is used in the (statistical) test where the signal fraction is taken to be the parameter of interest. The likelihood function for the signal+background hypothesis is the one defined in eq. 5.5. Figure 6.2 shows the result of the local significance with respect to the signal mass hypotheses (used in the signal pdf) by the RooStats [69] implementation of the PLR test, based on the Asymptotic formulae.

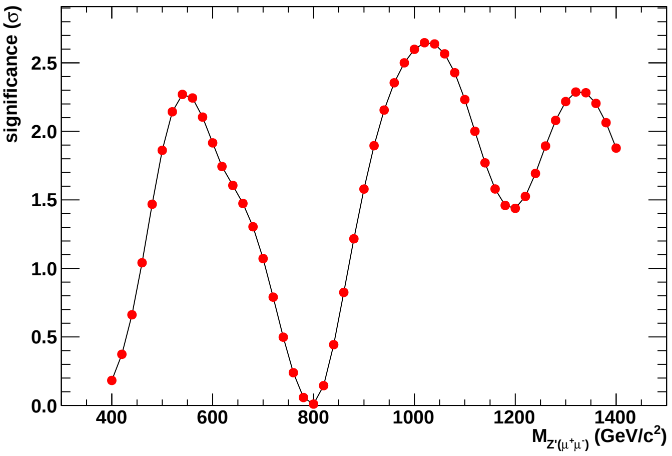

Fig. 6.2: Observed local significance in the full mass scan with peak-search analysis.

During the fit, the same signal width is assumed for each signal model, and data starting from the invariant mass of 400 GeV/c^2 is used. As can be seen, three different excess regions are observed. The invariant mass window of 800-1200 GeV/c^2 is chosen to be the mass range of interest where the largest excess is seen, and the matrix-element analysis is performed with the observed di-muon events falling into this mass window.

6.4 Application of the Method in a Narrow Mass-Range of Interest

6.4.1 Parametrization of the Detector Resolution

The mass resolution of the di-muon events, and thereby the muon momentum reconstruction, plays a crucial role in the analysis. The momentum assignment for high-p_T muons and the performance of the reconstruction algorithms have been studied by the CMS as presented in chapter 2. Tune-P is the suggested algorithm in the muon momentum assignment. In order to perform the analysis, first we need to define the TFs describing the muon momentum resolution.

The construction of TFs requires the complete description of the detector resolution. Let us remind that the TFs are defined by assuming factorization on the parameters defining the detector resolution, therefore the analytical parametrization will be performed on single muon tracks assuming no correlation between two muons (see sec. 4.1.4). Additionally, di-muon events coming from a heavy resonance decay are assumed to be mostly in the small η region. In order to parametrize the detector resolution, opposite-charge, back-to-back di-muon particles have been generated in a range of p_T values, from 50GeV to 700GeV/c, around 10k of events. The MC generated events were then passed through the CMS event reconstruction software. After the reconstruction of events, the analysis selection criteria are applied on the single-muon tracks by requiring the momentum assignment of the Tune-P algorithm. Then, the resolution of the reconstructed muon tracks is parametrized according to the generated muon p_T. The resolution parameter σ^{μ}_{Res} which defines the effect of detector reconstruction on the muon tracks, is defined as

$$\sigma^{\mu}_{Res} = \frac{q^{Gen}/P_T^{Gen} - q^{Rec}/P_T^{Rec}}{q^{Gen}/P_T^{Gen}}, \tag{6.1}$$

where q^{Rec} and q^{Gen} are the reconstructed and generated charge of muons, and P_T^{Rec} and P_T^{Gen} are the reconstructed and generated muon transverse momentum. The charge of the muon in the equation takes into account the possible charge flip due to mis-recontruction of the track curvature.

The σ^{μ}_{Res} is plotted for each generated muon p_T starting from 50GeV to 700GeV/c and inspected. It is found that the core of distributions can be fitted well with a single-Gaussian functions. The effect due to charge flip is observed to be very small and is only seen in the far tails of the distributions for high momentum tracks and it does not play any role in the analytical parametrization. Therefore, the charge terms have been dropped in the equation and the following definition is used, instead:

$$\sigma^{\mu}_{Res} = \frac{1/P_T^{Gen} - 1/P_T^{Rec}}{1/P_T^{Gen}}. \tag{6.2}$$

In figures 6.3, 6.4 and 6.5, the resolution parameter σ^{μ}_{Res} is plotted for each generated transverse momentum in three different η regions of the detector: barrel:$|\eta|$ <0.9, barrel-endcap (transition):0.9 < $|\eta|$ <1.2 and end-cap:$|\eta|$ >1.2. As can be seen, a single-Gaussian function is a good description for the detector resolution in the barrel and transition region of the detector. On the other hand, the resolution in the end-cap region shows more a double Gaussian behavior. Therefore, a double-Gaussian fit is performed for the end-cap region of detector, as shown in figure 6.5.

As can be seen from the figures of the resolution, the formalization in eq. 6.2 is a good description of the parametrization of the detector response for high-p_T muons. The non-Gaussian tails are rather in the low-p_T bins in the plotted histograms. Since the analysis region is restricted around 1TeV/c^2 in the invariant mass, the di-moun events entering this mass range are expected to have high-p_T values. Therefore, the chosen parametrization of resolution on the muon momentum is assumed to be adequate.

The functions used to parametrize the dependence of the single-Gaussian width of the $1/P_T$ resolution distributions in figures 6.3 and 6.4 are defined as:

$$\begin{aligned} \sigma^{\mu}_{\eta}(\frac{1}{P_T}) &= a + b(\frac{1}{P_T^{Gen}}) + c\sqrt{\frac{1}{P_T^{Gen}}} \qquad (|\eta| < 0.9) \\ \sigma^{\mu}_{\eta}(\frac{1}{P_T}) &= a + b(\frac{1}{P_T^{Gen}}) + c\log(\frac{1}{P_T^{Gen}}) \qquad (0.9 < |\eta| < 1.2) \end{aligned} \tag{6.3}$$

For the endcap ($|\eta| > 1.2$), the functions that parametrize the dependence of the two Gaussian widths used to fit the distributions in figure 6.5 are defined as

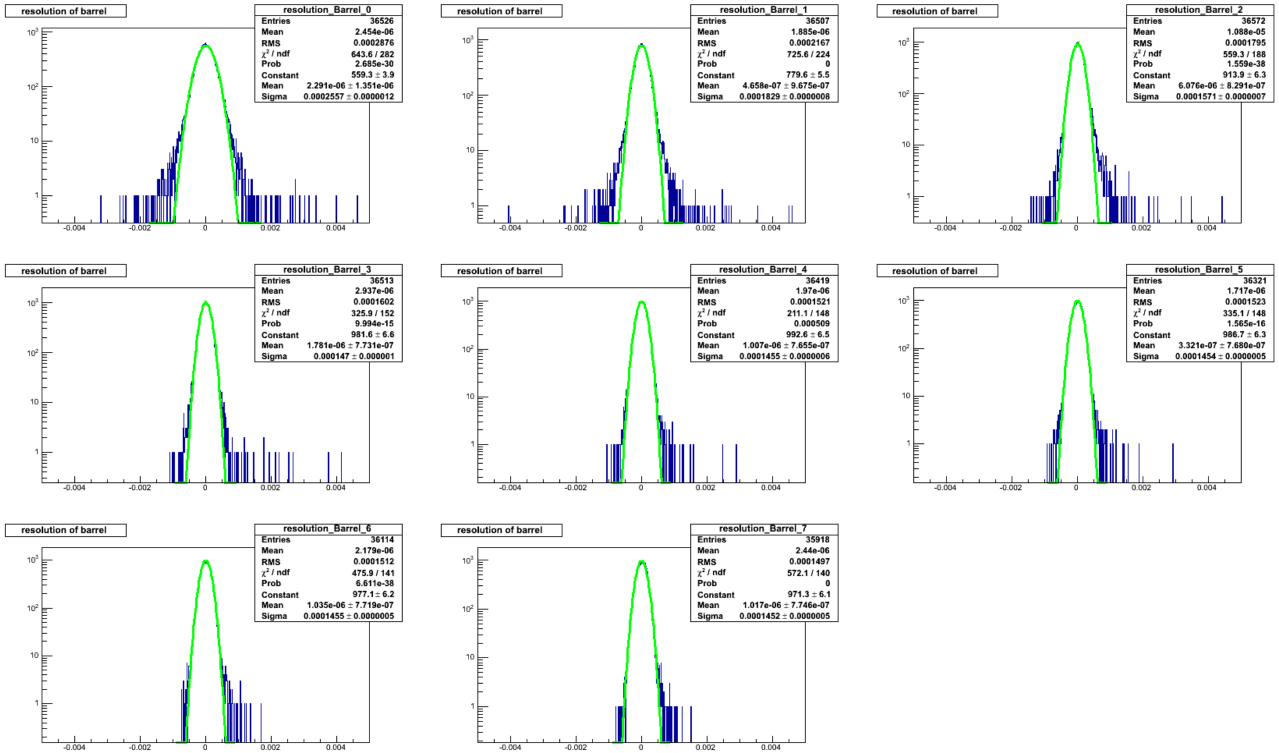

Fig. 6.3: The muon momentum resolution (σ^{μ}_{Res}) distributions obtained with generated single muon tracks having a generated p_T of 50,100,200,...,700GeV/c in the barrel:$|\eta|$ <0.9 region. Each green line corresponds to a single-Gaussian fit to obtained distribution.

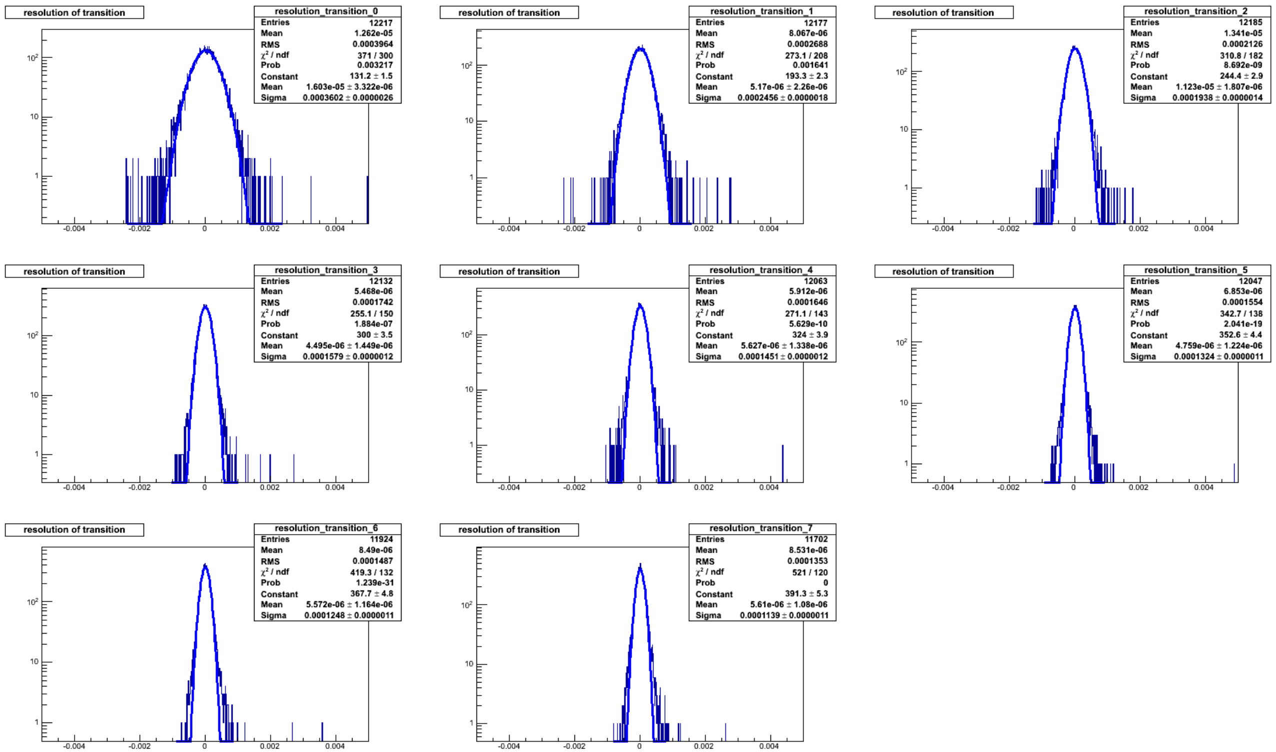

Fig. 6.4: The muon momentum resolution (σ^{μ}_{Res}) distributions obtained for the generated muon tracks in the barrel-endcap:0.9 $<$ $|\eta|$ $<$1.2 transition region of the detector for each generated muon p_T of 50,100,200,...,700GeV/c. Each blue line corresponds to a single-Gaussian fit to the obtained distribution.

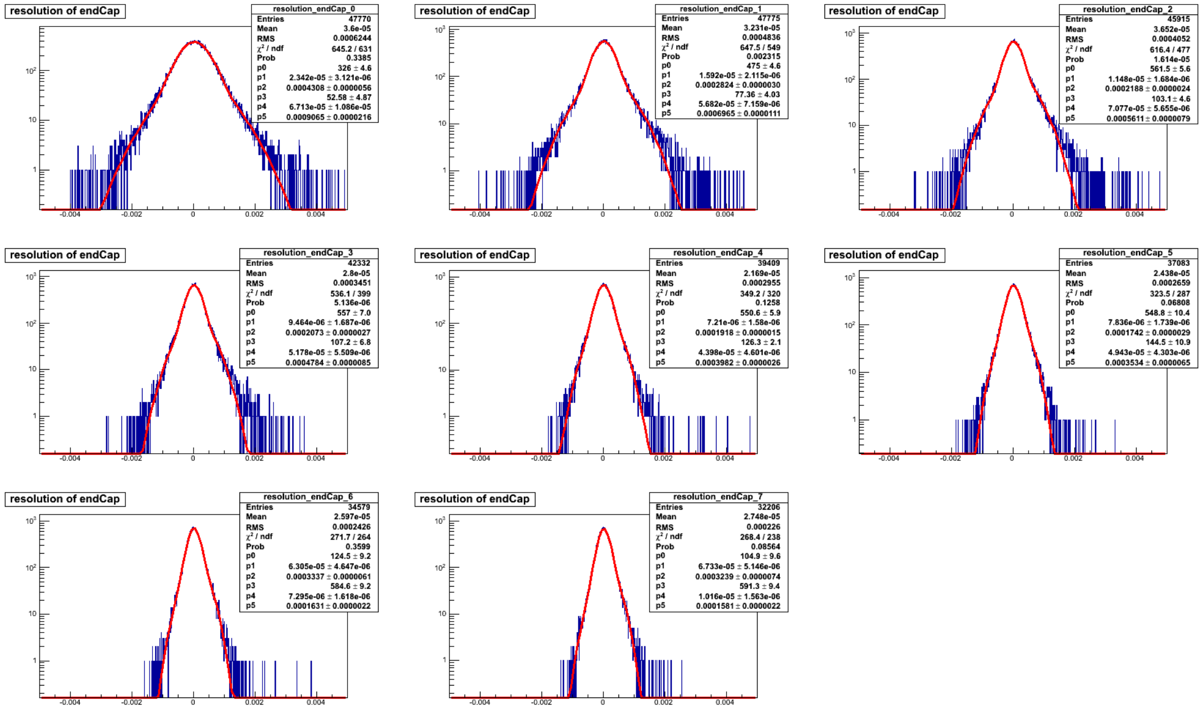

Fig. 6.5: The muon momentum resolution (σ^{μ}_{Res}) distributions obtained for the generated muon tracks in the endcap:$|\eta|$ >1.2 region for 50,100,200,...,700GeV/c of the generated muon p_T. Each red line corresponds to a double-Gaussian fit to each distribution obtained.

$$\begin{aligned}\sigma_1^{\mu}(\frac{1}{P_T}) &= a + b(\frac{1}{P_T^{Gen}}) + c\log(\frac{1}{P_T^{Gen}})\\ \sigma_2^{\mu}(\frac{1}{P_T}) &= a + b(\frac{1}{P_T^{Gen}}) + c\log(\frac{1}{P_T^{Gen}})\end{aligned} \tag{6.4}$$

The resolution function for the endcap region of the detector is given by*

$$N_1 Gauss((0, \sigma_1^{\mu}(\frac{1}{P_T})) + N_2 Gauss(0, \sigma_2^{\mu}(\frac{1}{P_T})), \tag{6.5}$$

where N_1 and N_2 are the relative normalization factors. Since the normalization condition is established by requiring $N_1 + N_2 = 1$, only N_1 is parametrized and N_2 is found by $1 - N_1$. Figure 6.9 shows the normalization factor N_1 with respect to the generated muon p_T. It should be noted that the resolution functions describing barrel and transition region are normalized to unity.

Although for simplicity, a, b and c terms in the equations (eq. 6.3, 6.4 and 6.5) and in the histograms are given with the same name, note that they correspond to different fitted values in each parametrization for three different region of the detector.

Figures 6.6, 6.7 and 6.8 show the muon momentum resolution analytically parametrized as a function of $1/p_T$ in the barrel, transition-region and in the end-cap region of the detector. The colored lines in each figure are the functions used for fitting, the values of the fitted parameters are shown on each figure as well.

6.4.2 Local Significance with the Asymptotic Approach

Having equation 6.3, 6.4 and 6.5) in hand, we can define the TFs on muon momentum as $w(P_T^{Rec}; P_T^{Gen}, \sigma_{\eta}^{\mu}(1/P_T^{Gen}))$ where the width is

---

*Note that Gauss(0,$\sigma_{1,2}^{\mu}(\frac{1}{P_T})$) terms in the equation stand for standard Gaussian distributions with a mean equal to zero and a width equal to $\sigma_1^{\mu}(\frac{1}{P_T})$ and $\sigma_2^{\mu}(\frac{1}{P_T})$.

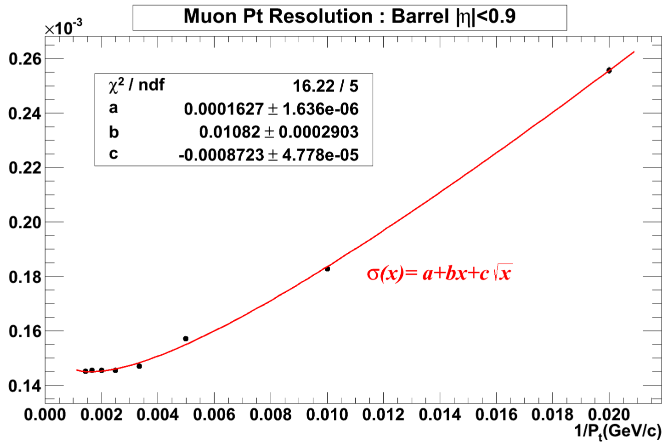

Fig. 6.6: The muon momentum resolution parametrization (see eq. 6.3) for the barrel region:$|\eta| < 0.9$.

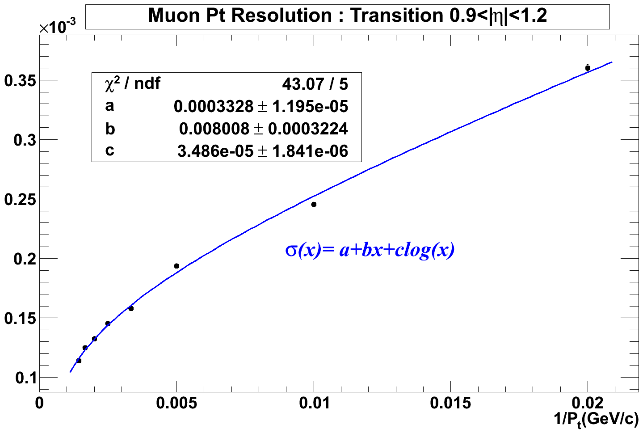

Fig. 6.7: The muon momentum resolution parametrization (see eq. 6.3) for the transition region:$0.9 < |\eta| < 1.2$.

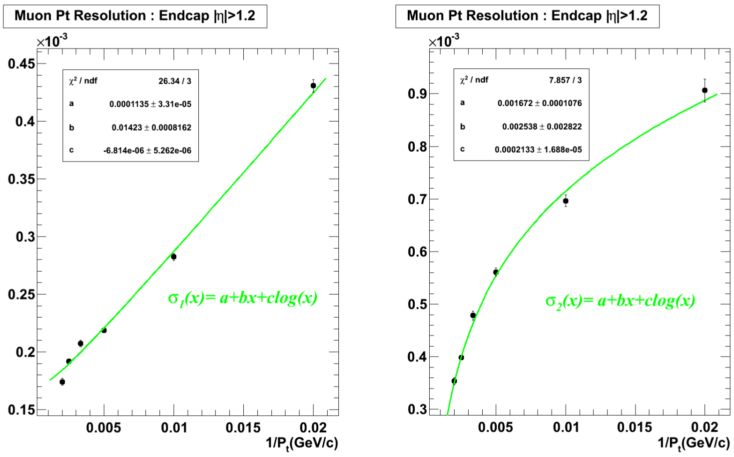

Fig. 6.8: The muon momentum resolution parametrization for the end-cap region:$1.2 < |\eta| < 2.4$. The plot in the left shows the parametrization for σ_1^μ, while the plot on the right shows σ_2^μ (see eq. 6.4).

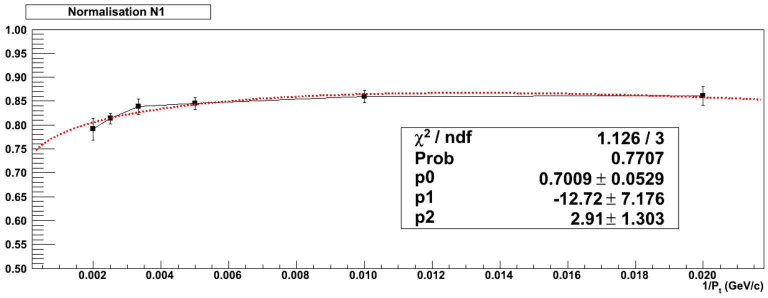

Fig. 6.9: Normalization factor N_1 with respect to the generated muon p_T for end-cap: $1.2 < |\eta| < 2.4$.

analytically parametrized in three η regions of the detector. Defined transfer functions are used during the calculation of the event weights for the signal and background hypotheses in all numerical computations of the test statistics.

In figure 6.10, the local significance with the asymptotic approach for the observed data can be seen with respect to the signal mass hypothesis from 900 to 1100 GeV/c^2. Each point corresponds to a different signal mass hypothesis used in the signal model tested. The highest significance is observed around 1050 GeV which is compatible with the highest significance obtained by the peak-search analysis (see fig. 6.2). On the other hand, there are few remarks need to made: First, this result is obtained with the TFs parametrized only with the core resolution (namely single-Gaussian) functions in all three regions of the detector, therefore should be compared directly with the numerical results where double-Gaussian parametrization is also used to describe the tails. Second, the scan with the peak-search analysis as shown in figure 6.2 is only performed to narrow down the search region, the pdfs used in the likelihood for signal and background models do not describe the real experiment, for example the background pdf model is only obtained by fitting the low mass region, therefore should not be compared with the figure 6.10. Third, there is no systematic effect considered in the calculations at this point, as it will be discussed in detail in the following sections.

6.5 Incorporating the Systematic Uncertainties

There can be various known uncertainties that affect the measured model parameters which can be categorized as experimental and theoretical depending on their origins. This section describes how these uncertainties are taken into account. First, all possible sources of experimental and theoretical uncertainties will be discussed. Later, an approach based on the generation of toy-MC data sets with nuisance parameters for the computation of the local significance and the upper-limit will be described.

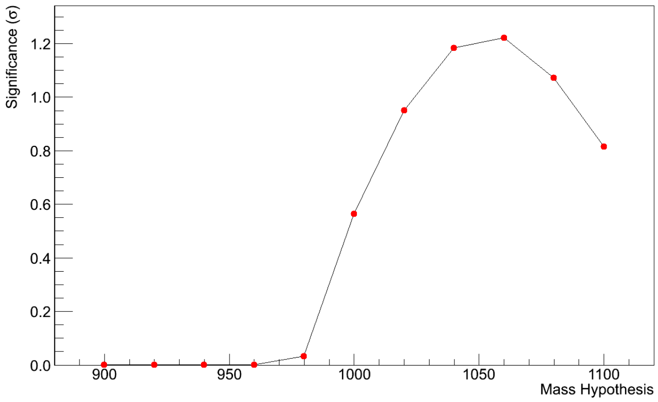

Fig. 6.10: Observed local significance obtained using the Matrix Element Likelihood Method with the asymptotic approach. The data points correspond to different signal mass hypotheses used in the signal pdf.

6.5.1 Experimental Uncertainties

The sources of experimental uncertainties considered in the analysis are categorized as following;

- **Muon Reconstruction and Identification**: Muon reconstruction and identification efficiencies vary with respect to the η of the detection region. The tight muon identification is required by the analysis selection on each muon. As estimated by CMS [46] the muon reconstruction and identification efficiencies are 96.4% in $0.0 < |\eta| < 1.2$ and 96.0% in the $1.2 < |\eta| < 2.4$ regions for muons with $p_T > 20$ GeV/c. The systematic uncertainties on these measured values are 0.2% and 0.4%, respectively.

- **Muon Momentum Resolution**: As described in section 6.4.1, the resolution on the muon transverse momentum is parametrized with respect to the muon p_T. According to the muon resolution studies performed by CMS [46], the difference between different track fitting procedures on the resolution is taken as an estimate of the systematic uncertainty. This difference is found to be about the same in the barrel and endcap and can be described by assigning a 20% systematic uncertainty to the fitted parameters that describe the momentum resolution (see eq. 6.3 and 6.4). These uncertainties are taken as fully correlated in the barrel, transition and end-cap region of the detector.

- **Muon Momentum Scale**: The muon reconstruction algorithms for high-p_T muons are tested with cosmic muons for a possible curvature bias. In CMS the shape of the q/p_T spectrum is used to study this effect [46]. Using the cosmic-ray muons reconstructed with p_T >200 GeV/c, a bias factor κ in the form of

$$q/p_T \rightarrow q/p_T + \kappa \tag{6.6}$$

  is measured by CMS. The value of κ in data is found to be $-0.20 \pm 0.12(stat) \pm 0.02(syst) c/\text{TeV}$.

- **Muon Isolation**: Muon isolation is used to discriminate muons coming from decay of W,Z or a heavy resonance from those coming from hadron decays or from hadron misidentifications. The isolation criteria used in this analysis is the “tracker-relative” isolation. The algorithm calculates the scalar sum of the p_T of all tracker tracks reconstructed in a cone centered around the muon with a radius of $\Delta R = \sqrt{(\delta\phi)^2 + (\Delta\eta)^2} < 0.3$ excluding the muon p_T itself. The sum is then compared to muon p_T and a threshold is set, in the relative comparison to muon p_T. In the analysis, the isolation threshold is required to be 0.1. It is found that the systematic uncertainty on the isolation efficiency is very small, 0.2% on the single muons [70].

- **Trigger**: The events used in the analysis are collected by requiring the lowest p_T threshold for the un-prescaled single muon trigger to be 40 GeV/c and $|\eta| < 2.1$. The overall trigger efficiencies, L1+HLT, of selecting two muons, one in $|\eta| < 2.1$ and the other in $|\eta| < 2.4$ with both muons having a $p_T > 45 GeV/c$, is predicted to be 98% [71, p.3]. The uncertainty on the trigger is estimated to be 1%, constant with respect to the invariant mass of the selected di-muon events.

- **Others**: The luminosity collected by the CMS detector corresponds to $5.3fb^{-1}$. The uncertainty on this value is 2.2% as provided by CMS [72].

6.5.2 Theoretical Uncertainties

The uncertainties on PDF sets are one of the main sources of systematic uncertainties on the cross sections for signal and background. A common way to study the effect of PDF uncertainties is to change the input PDF set to a different one, such that the effect of this difference is visible on the observables. The difference in the variation can be assigned as systematic uncertainty. Let us remind that the analysis is based on the usage of *weights* in a likelihood formalism provided by MadWeight software, based on the leading order matrix element calculations, while using the events as observables. Estimating the effect of change in the likelihood with respect to each parameter defined in the PDF sets by varying each set of parameters within their uncertainties requires large toy-MC generations.

Since including the PDF uncertainties with toy-MC experiments is highly CPU demanding, another simpler approach is followed in assessment of this effect. The determination of the effect is based on the evaluation of the variation of the invariant mass of the di-muon events. For the comparison, the nominal CTEQ6L1 (LO) PDF sets changed to CTEQM (NLO) sets via the usage of standalone LHAPDF libraries [73] during the event generation with MadGraph. In order to study the effect of the PDF, different set of signal and background events are generated while varying the input PDF sets during the generation step. Figure 6.11 shows the invariant mass distribution of signal events corresponding to CTEQ6L1 and CTEQM PDF sets at generation level, before any smearing applied due to detector resolution. The effect of the uncertainty in the momentum resolution is shown as well in figure 6.11 (b). Figure 6.11 (b) shows the invariant mass distribution of generated signal events, after introducing the detector smearing, for different input PDF sets. The blue line corresponds to the increase of the detector resolution about 1σ than the expected central value. As can be seen, the detector resolution is a dominant effect on signal events compared to varying such PDF sets.

Similarly, figure 6.12 is plotted in the same way for the background events. The obtained invariant mass distributions are fitted with various exponential fits describing the background model. The fit functions are shown in the figure corresponds to $\exp^{a.m}\, m^b$ where m is the invariant-mass of the dimuon events. The figure is plotted with the background events after detector effects, while different sets of PDFs were used during the event generation. The effect of detector resolution, in comparison to PDFs, was varied by $\pm 1\sigma$, while using the nominal PDF set as input. As depicted in the figure, in comparison to the detector resolution, the differences of such PDFs have a smaller effect on the fitted shape parameters, and therefore can be neglected, assuming that the effect of the PDF difference, in comparison to momentum resolution, is small in the event weights calculated for signal and background. However this does not hold for the background cross section (σ_B) which appears in the likelihood and is affected by PDF uncertainties.

As it was shown by a CMS analysis [74], a constant k-factor of 1.3 can be taken in the mass region around 1 TeV/c^2 to account for higher order QCD effects on the Drell-Yan background. The variation of the uncertainty on the mass-dependent k-factor is not more than few percent in the considered invariant-mass range of 800-1200 GeV/c^2. Since the invariant mass window of the analysis is restricted to this mass range, the same constant k-factor is applied. A constant k-factor does not require any special care in the statistical treatment of the analysis as a cross section scale factor is already present in the likelihood function for the background. The effect of the k-factor is not included in the calculation of the event weights, neither for the signal nor for the background.

In addition to the parton distribution functions inside the proton and the k-factor correction, initial state radiation, final state radiation and pure weak effects can be considered. These additional effects are not studied, therefore are not included in the calculation of event weights as well. On the other hand, the overall cross-section for background (σ_B) which is explicitly present in the likelihood function will be affected by

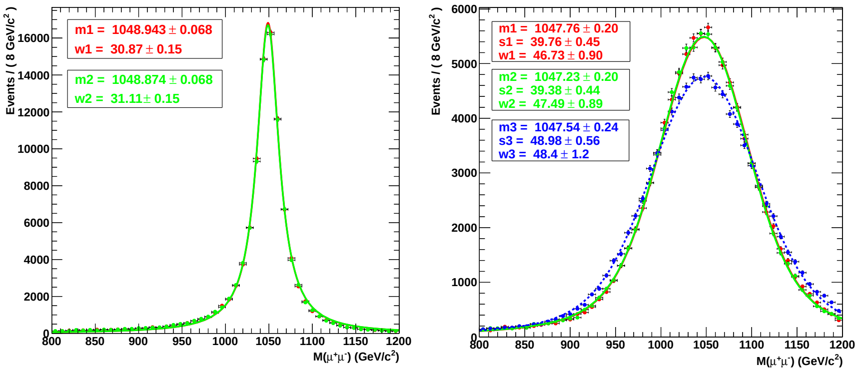

(a) **(b)**

Fig. 6.11: The effect of the PDF difference on the signal events. (a) At parton level without smearing with default PDF (CTEQ6L1) sets shown in the red line and the CTEQM shown in the green line with Breit-Wigner fits (b) After the detector smearing: the red line is old PDF sets, the green line shows the new PDF sets (CTEQM) and the blue line corresponds to the default PDF sets with resolution parameters increased by 1σ with the Voigtian fits (for the parameters see eq. 5.3).

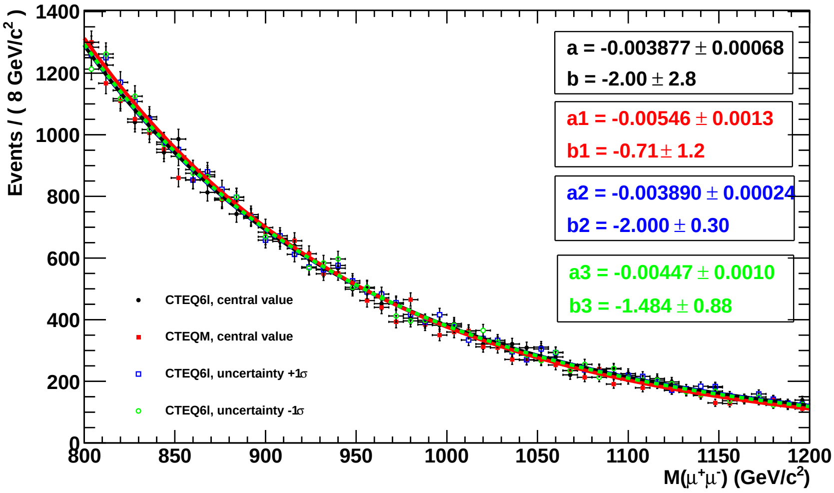

Fig. 6.12: The effect of PDF changes on the distribution of the background events (see text).

these theoretical uncertainties. An overall 20% uncertainty is assigned to the background cross section conservatively to account for all possible theoretical uncertainties mentioned.

6.5.3 Likelihood Function with Nuisance Treatment

In order to take into account all systematic uncertainties, one must define the nuisance parameters associated to such uncertainties and introduce them in the likelihood function. As it is defined before (see eq. 4.20), the likelihood function has the form of

$$L(\{x_i\};\mu,S,B) = \prod_i^n \left(\frac{\mu W_S(x_i;S)}{\mu\sigma_S\varepsilon_S + \sigma_B\varepsilon_B} + \frac{W_B(x_i;B)}{\mu\sigma_S\varepsilon_S + \sigma_B\varepsilon_B} \right).$$

The parameters ε_S and ε_B are the signal and background selection efficiencies and they will be affected by the choice of event selection and the mentioned experimental uncertainties. Therefore we need to estimate the variation of the efficiencies for selecting signal and background events in the analysis by considering all possible sources of systematic effects.

In order to determine variation on these efficiencies, we generate signal events corresponding to an SSM resonance with a mass of 1050 GeV, and background events in the 600-1400 GeV/c^2 invariant mass range. First, the generated events are smeared using the parametrized detector resolution functions (see sec. 6.4.1). Each parameter in the momentum resolution functions (in equation 6.3, 6.4 and 6.5) is considered as a nuisance parameter distributed according to a log-normal pdf. The momentum resolution parameters are fully correlated as discussed in section 6.5, the random values for each parameters are drawn using a single, auxiliary Gaussian-distributed random variable D, which is then simply analytically transformed into lognormal (with different central values and widths) distributed values[†]. For every toy experiment, the parameters defining the resolution functions of σ_η^μ describing the barrel, transition and end-cap region of the detector are generated following this procedure.

Not only the resolution, but also the systematic uncertainties associated with other detector effects are taken into account. The overall selection efficiencies for signal and background including the uncertainties of trigger, muon reconstruction, muon isolation and analysis selection efficiencies are evaluated using toy experiments composed of simulated events. In each toy experiment a set of efficiency values, each corresponding to one of the considered effects, is drawn from a lognormal pdf with a central value and a width corresponding to the estimated values. These efficiencies are then applied to all the events drawn in order to compose the toy experiment, either at the level of the di-muon or at that of the individual muons. Figures 6.13 and 6.14, show the distributions of the selection efficiencies of signal and background events, respectively. These distributions are obtained from 500 toy-MC experi-

---

[†] The generation of log-normal random distribution is based on the relation of generating the random numbers from a normal distribution. Given D is a standard normal distributed random variable, then theta, defined as $\theta = \exp^{\mu+\sigma \cdot D}$, is a log-normal distributed random variable where σ and μ are the parameters that characterize the log-normal distribution.

Uncertainties	di-muon	single muon
Trigger	1%	-
Muon Reconstruction	-	0.2% ($\|\eta\| < 1.2$)
	-	0.4% ($1.2 < \|\eta\| < 2.4$)
Muon Isolation	-	0.2%
Muon Momentum Resolution	-	20%

Tab. 6.1: The summary of experimental uncertainties used in the computation of signal and background selection efficiencies. Their effects on di-muon and single-muon events are also shown.

ments each containing 10k of background or signal events. Finally, each distribution is fitted to a log-normal function to obtain its nuisance pdf. In this way, a 1% uncertainty on the signal selection efficiency (ε_S) and 10% on the background (ε_B) are estimated while the central values are around 0.76 and 0.18, respectively.

In the derivation of the efficiency distribution, the effect of each systematic uncertainty can be controlled by switching it "on" and "off" in the software. Thus, the effect of the momentum scale on the selection efficiencies was studied separately by switching off the uncertainties on the momentum resolution parameters. In each toy, a shift κ is chosen, then it is is applied in the form of equation 6.6 to the muons that have a p_T >200 GeV/c. It was found that the effect of the momentum scale on the overall efficiencies is small , $\ll 1\%$, and it does not broaden up the distribution of efficiencies. Therefore, the effect due to the momentum scale is dropped and it is not introduced in the TFs during the computation of event weights as well.

The feature of the correlation of the detector resolution parameters reduces the number of nuisance parameters describing the momentum resolution to *one*, which is the D variable that has a standard normal distribution with a standard deviation equal to 1. In the likelihood, D is treated as a nuisance parameter. A possible way to accommodate the effect of momentum resolution is to vary the transfer functions. Therefore, a scan in the parameter D during the toy-MC generation and computation of weights is performed to include these sort of uncertainties, which

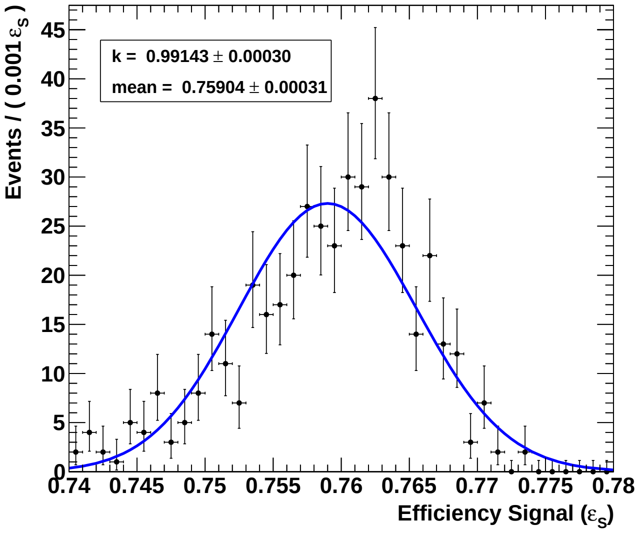

Fig. 6.13: Distribution of the signal selection efficiency (ε_S) for 500 toy-MC experiments. The blue line shows the log-normal fit to the obtained distribution.

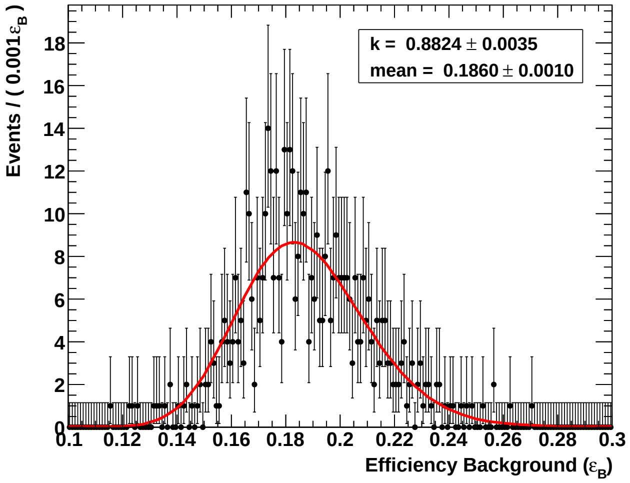

Fig. 6.14: The distribution of the background selection efficiency (ε_B) for 500 toy-MC experiments. The red line shows the log-normal fit to the obtained distribution.

Nuisance parameter	central value	uncertainty
Signal Selection Efficiency(ε_S)	0.76	1%
Background Selection Efficiency(ε_B)	0.186	10%
Luminosity	$5fb^{-1}$	2.2%
Muon Momentum Resolution	see TF	20%
Background Cross-Section(σ_B)	0.0097pb	20%

Tab. 6.2: Nuisance parameters and their uncertainties used in generation of the toy-MC data set.

will be discussed in the next section. Due to repetitive calculation of event weights by scanning over the parameter D, which brings a computational burden, a limited set of D values are considered.

The background cross section will be treated as another nuisance parameter with an uncertainty of 20% due the mentioned theoretical uncertainties. The signal cross section, on the other hand, is one of the parameter of interest through the signal strength modifier μ, therefore no uncertainty is assigned to this term. Table 6.2 is the summary of the nuisance parameters.

To summarize, the likelihood function including the nuisance parameters discussed above is defined as

$$\begin{aligned} L(\{x_i\}; \mu, \theta_j, S, B) = &\prod_i^n \left(\frac{\mu W_S(x_i; S, \theta_k(D))}{\mu \sigma_S \varepsilon_S + \sigma_B \varepsilon_B} + \frac{W_B(x_i; B, \theta_k(D))}{\mu \sigma_S \varepsilon_S + \sigma_B \varepsilon_B} \right) \\ &G(D) \prod_l LN(\theta_l), \end{aligned} \tag{6.7}$$

where θ_j is the set of nuisance parameters, ε_S, ε_B, σ_B. $G(D)$ is the unit Gaussian pdf centered at 0. LN(θ_l) indicates the log-normal pdfs. The $\theta_k(D)$, appearing in the signal and background weights, indicates the momentum resolution parameters established by variable D, which are a function of muon p_T. In summary, the likelihood is defined as a function of a set of nuisance parameters, observables and the parameters of interest.

Since the aim of the analysis is to estimate (or set an upper-limit on) the signal cross section times branching fraction, it is important to be protected against background fluctuations that give rise to a discovery significance in situations where no actual signal is present in the data. In order to take into account these possible fluctuations, a scale factor β on the background event rate is introduced. With this modification, the likelihood function is re-defined as:

$$\begin{aligned} L(\{x_i\};\mu,\theta_j,S,B) = &\prod_i^n \left(\frac{\mu W_S(x_i;S,\theta_k(D))}{\mu\sigma_S\varepsilon_S+\beta\sigma_B\varepsilon_B} + \frac{\beta W_B(x_i;B,\theta_k(D))}{\mu\sigma_S\varepsilon_S+\beta\sigma_B\varepsilon_B} \right) \\ & G(D)\prod_l LN(\theta_l). \end{aligned} \tag{6.8}$$

Scale factor β is treated in such a way to accommodate uncertainties on the background cross-section and the selection efficiency.

6.6 A Multiparameter Unbinned Maximum Likelihood Fit

The computation of the test statistics distribution requires computing the likelihood ratio for toy-MC experiments. Each toy-MC experiment needs to be generated according to a set of nuisance parameters which are constrained by their pdfs. Then, for every toy, the likelihood function needs to be maximised with respect to nuisance parameters and the parameter of interest, as detailed in section 4.2.4. In practice this maximisation is extremely computing power expensive.

It is crucial to find an easy way of the computation of the profile likelihood ratio over multiple nuisance parameters. A dedicated software has been developed to do such computations and the TMinut minimization package [75] is used to perform the likelihood maximization of lnL(μ, θ_j), or the minimization -lnL(μ, θ_j). In most cases, the Migrad algorithm [76] is employed. Additionally, the Simplex algorithm [77] is also used to further improve the fit in cases where Migrad failed to find a minimum. The data set was discarded where the fit did not converge and no local minimum was found which happened in only few cases among all computations.

To summarize the toy-MC generation and likelihood fitting procedure for upper limit calculation for example: a set of toy-MC experiments corresponding to D values chosen (-1, -0.5, 0, 0.5 and 1) as well as randomly chosen β and other nuisance parameters, were generated by allowing each component of data set (N_S and N_B) to Poisson fluctuate at the obtained value of signal and background events[‡]. In figure 6.15, for example, the distribution of generated β scale parameter can be seen. Then, given that a likelihood maximization is needed for the computation of the experiment test statistic, the event weights were computed with the transfer functions modified according to each D value for five times. During the likelihood maximization, nuisance parameters are bound in $\pm 5\sigma$, while the signal strength μ parameter is left free. The PLR test statistics is calculated under the conditions of the tested hypotheses. The same fitting procedure was repeated in order to obtain the distribution of the test statistics.

The discovery significance is calculated over background-only toy-MC experiments. On the other hand, toy-MC experiments of signal and background events are composed according to the tested signal strength parameter μ in the calculation of the upper limit.

6.7 Results

6.7.1 Local Significance

The determination of the presence of signal events can be quantified via the calculation of the discovery significance. The local significance is

---

[‡] In other words, N_S and N_B are allowed to fluctuate around $< N_S >= Luminosity.\sigma_S.\varepsilon_S$ and $< N_B >= Luminosity.\sigma_B.\varepsilon_B$.

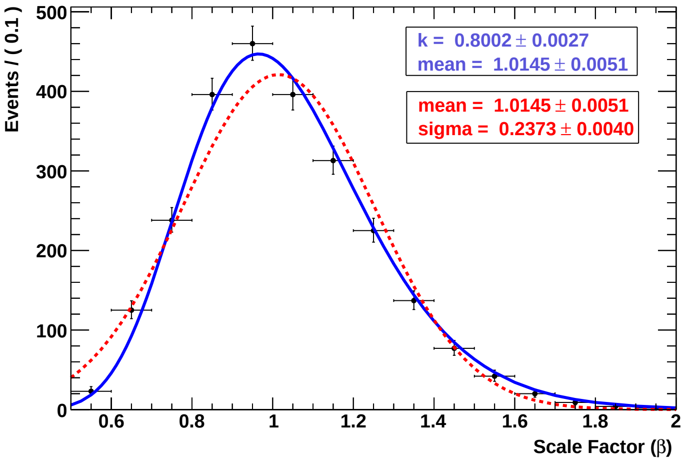

Fig. 6.15: The distribution of background scale factor (β) for 2k of toy-MC experiments. The blue line shows the log-normal and the red line is the Gaussian fit to the obtained distribution.

calculated via the distribution of the test statistics for a positive signal present in the observed data.

Figure 6.16 shows the test statistics distribution of q(0) for 2k of toy-MC experiments (blue) and observed data (red arrow). The toy-MC experiments contain the background-only events. The computed z-score corresponds to 1.3σ from the upper tail integral, for a signal mass hypothesis of 1050 GeV. The CMS analysis [68, 78] quotes 1.2σ local significance with a peak-search analysis performed around the same invariant mass region, with the highest excess occurring at the mass value of 1005 GeV.

6.7.2 Upper Limit on $\sigma_S \times BR$

For setting an upper limit, toy-MC experiments are generated with an ensemble of signal and background events for tested μ value. Each signal and background component is allowed to fluctuate with a mean expected value that is drawn from a Poisson distribution. The PLR test

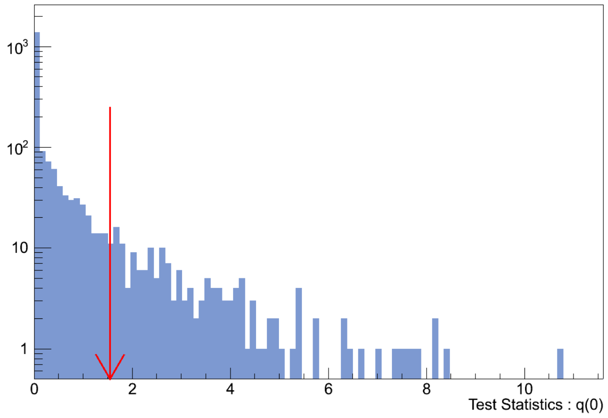

Fig. 6.16: Test statistics distributions of a discovery generated from background-only 2k toy-MC experiments. The red arrow corresponds to the observed value from data.

was performed for the ratio of the background hypothesis tested against the signal+background for different values of μ. The test statistic distribution q_μ (see eq. 4.27) is obtained for each tested value of μ. In figure 6.17 the distribution of the test statistics and the obtained value for observed data can be seen. The blue shade corresponds to the test results obtained with a thousand of toy-MC experiments. The red arrow is the observed data. The observed upper limit on the μ signal strength is found to be 0.063. Therefore, the upper limit on the cross section times branching fraction for a production of a sequential Z′ model is set to 0.0034pb at the 95%C.L.

Setting a lower mass bound on this signal model with observed data considering the full invariant mass range ($\geq 200GeV$), however, requires a large parameter scan it is not aimed in this analysis. Given that the analysis shown here is optimized in an invariant mass window, it can be considered as one of the future improvements.

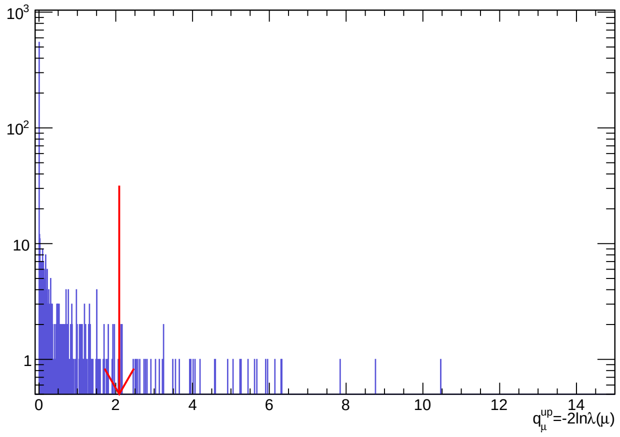

Fig. 6.17: Test statistics distribution for setting an upper-limit on the μ signal strength at 95%C.L. The blue filled area corresponds to the result of toy-MC experiments. The red arrow is observed value.

Conclusions and Outlook

The Standard Model of particle physics has proven to be a very successful theory to describe the fundamental interactions in nature. The discovery of a Higgs boson by the Atlas and CMS experiments at the LHC has been the ultimate confirmation of the predictions by the theory. However, this model does not answer to many open questions, for example the hierarchy problem, the origin of the fermion generations, quantum gravity, and the unification of the forces.

Many BSM models that address these problems predict new heavy neutral gauge bosons. An experimentally and particularly appealing final state to search for these new particles at the LHC is the di-muon final state. However, despite various searches conducted at the collider experiments, no evidence for such new particles has been found so far, indicating that these particles might be heavier and produced at a lower rate than expected.

By improving the reconstruction and analysis techniques, the sensitivity of these searches can be enhanced. This thesis presents the results of research performed along both of these lines: a novel method for mapping the distribution of the detector material and a matrix element likelihood approach are developed, fully validated and applied to the collision data. The first method aims to improve the measurement of the material distribution in the track reconstruction, and the second is an analysis method dedicated to the improvement of the sensitivity for a discovery of a narrow di-muon resonance.

The first method is based on the extraction of the CMS Tracker material distribution by checking the consistency of the track reconstruction algorithm, using the reconstructed tracks. The accurate knowledge of the material mounted in the detector is of importance to the reconstruction of the muons, hence a new method based on the track reconstruction to probe the inner tracker material is developed to measure the actual material distribution placed in the CMS Silicon Tracker detector. The method is easily applicable and its accuracy is comparable to that of more traditional methods. The method also proves to be complementary to such traditional methods in that it suffers from different sources of uncertainty. It has been shown that this relatively simple, data-driven method can provide results for the overall detector volume with relatively low statistics. An overall agreement around 10-20% is observed by comparing the MC results with the collision data, and these results can be used to give feedback to the physics analyses for the evaluation of the systematic uncertainties due to the Tracker material. The method aims to improve both the details of the simulation of the material inside the tracking volume, as well as the treatment of the material effects in the track reconstruction. Therefore, it allows for an improvement in the reconstruction model.

The second method, the Matrix Element Likelihood Method , relates the full event information to the invariant matrix element of the physics processes. The analysis approach has been formulated, developed and fully validated with MC generated events, demonstrating the robustness and the performance of the method. Depending on the sample size, a sensitivity improvement of 10-20% is obtained, in comparison to the method currently used in the CMS analysis. It has been shown that the method can be used for hypothesis testing and parameter estimation, incorporating both theoretical and experimental systematic uncertainties. The search method has subsequently been applied to the collision data, in a mass window where the highest excess is seen; numerical computations show a local significance of 1.3σ around $M(\mu^+\mu^-) = 1050$ GeV/c^2, compatible with the CMS measurement. Furthermore, an upper limit is set at this signal mass for the tested Sequential Z' signal cross section times branching fraction.

The analysis approach described here, implemented in independent software, is computationally limited, but improvements in the performance are a possible subject for future studies. In case a possible significant excess is seen in the invariant-mass distribution of di-muon events, the method can be used to determine the model parameters that describe best the observed data. This can be the subject of future developments as well.

The upcoming program of the LHC proton-proton collisions, at an increased center-of-mass-energy of 13 and 14 TeV, will make it possible to explore the higher invariant mass regions with di-muon events. The described analysis methods could be very useful to investigate these regions of the spectrum, in order to probe the existence or non-existence of new heavy particles, as expected by many theoretical models. Considering the fact that these high-mass regions will be statistically limited, sensitive analysis methods will gain importance in the future LHC searches; the analysis methods presented in this thesis can contribute to the future studies in this direction. In case of an observation of a new phenomenon, the method can be used to reveal the properties of this discovery.

Bibliography

[1] Nobelprize.org. The Nobel Prize in Physics 2013. `http://www.nobelprize.org/nobel_prizes/physics/laureates/2013/`.

[2] Michael E. Peskin and Daniel V. Schroeder. An Introduction to quantum field theory. 1995.

[3] *Quarks and Leptons An Introductory Course in Modern Particle Physics*. John Wiley and Sons, Inc., 1984.

[4] Y. Fukuda et al. Evidence for oscillation of atmospheric neutrinos. *Phys.Rev.Lett.*, 81:1562–1567, 1998.

[5] J. Hosaka et al. Three flavor neutrino oscillation analysis of atmospheric neutrinos in Super-Kamiokande. *Phys.Rev.*, D74:032002, 2006.

[6] R. Keith Ellis, W. James Stirling, and B.R. Webber. QCD and collider physics. *Camb.Monogr.Part.Phys.Nucl.Phys.Cosmol.*, 8:1–435, 1996.

[7] F. Englert and R. Brout. Broken Symmetry and the Mass of Gauge Vector Mesons. *Phys.Rev.Lett.*, 13:321–323, 1964.

[8] Peter W. Higgs. Broken Symmetries and the Masses of Gauge Bosons. *Phys.Rev.Lett.*, 13:508–509, 1964.

[9] Serguei Chatrchyan et al. Observation of a new boson at a mass of 125 GeV with the CMS experiment at the LHC. *Phys.Lett.*, B716:30–61, 2012.

[10] Georges Aad et al. Observation of a new particle in the search for the Standard Model Higgs boson with the ATLAS detector at the LHC. *Phys.Lett.*, B716:1–29, 2012.

[11] Precise determination of the mass of the Higgs boson and studies of the compatibility of its couplings with the standard model. Technical Report CMS-PAS-HIG-14-009, CERN, Geneva, 2014.

[12] Serguei Chatrchyan et al. Measurement of the weak mixing angle with the Drell-Yan process in proton-proton collisions at the LHC. *Phys.Rev.*, D84:112002, 2011.

[13] S.D. Drell and Tung-Mow Yan. Massive Lepton Pair Production in Hadron-Hadron Collisions at High-Energies. *Phys.Rev.Lett.*, 25:316–320, 1970.

[14] Ringaile Placakyte. Parton Distribution Functions. Technical Report arXiv:1111.5452, Nov 2011. proceedings of XXXI Physics in Collision, Vancouver, BC Canada, 28 Aug-1 Sep, 2011.

[15] Amos Breskin and Rüdiger Voss. *The CERN Large Hadron Collider: Accelerator and Experiments*. CERN, Geneva, 2009.

[16] Serguei Chatrchyan et al. Measurement of the differential and double-differential Drell-Yan cross sections in proton-proton collisions at $\sqrt{s} = 7$ TeV. *JHEP*, 12:030, 2013.

[17] J.Beringer et al. (Particle Data Group). Review of particle physics. *Phys. Rev. D*, 86:010001, Jul 2012.

[18] S. Kretzer, H.L. Lai, F.I. Olness, and W.K. Tung. Cteq6 parton distributions with heavy quark mass effects. *Phys.Rev.*, D69:114005, 2004.

[19] A. Leike. The Phenomenology of extra neutral gauge bosons. *Phys.Rept.*, 317:143–250, 1999.

[20] Serguei Chatrchyan et al. Measurement of the Drell-Yan Cross Section in pp Collisions at $\sqrt{s} = 7$ TeV. *JHEP*, 1110:007, 2011.

[21] Vardan Khachatryan et al. Measurements of Inclusive W and Z Cross Sections in pp Collisions at $\sqrt{s} = 7$ TeV. *JHEP*, 1101:080, 2011.

[22] Georges Aad et al. Measurement of the low-mass Drell-Yan differential cross section at $\sqrt{s} = 7$ TeV using the ATLAS detector. *JHEP*, 1406:112, 2014.

[23] Georges Aad et al. Measurement of the high-mass Drell–Yan differential cross-section in pp collisions at sqrt(s)=7 TeV with the ATLAS detector. *Phys.Lett.*, B725:223–242, 2013.

[24] Ryan Gavin, Ye Li, Frank Petriello, and Seth Quackenbush. FEWZ 2.0: A code for hadronic Z production at next-to-next-to-leading order. *Comput.Phys.Commun.*, 182:2388–2403, 2011.

[25] W. de Boer. Grand unified theories and supersymmetry in particle physics and cosmology. *Prog.Part.Nucl.Phys.*, 33:201–302, 1994.

[26] Paul Langacker. Grand unified theories and proton decay. *Physics Reports*, 72(4):185 – 385, 1981.

[27] J.L. Hewett and T.G. Rizzo. *Phys. Rep.*, pages 183–193, 1989.

[28] Mirjam Cvetic and Stephen Godfrey. Discovery and identification of extra gauge bosons. 1995.

[29] Marcela Carena, Alejandro Daleo, Bogdan Dobrescu, and Tim Tait. Z' gauge bosons at the Fermilab Tevatron. *Phys. Rev. D*, 70:093009, Nov 2004.

[30] Nima Arkani-Hamed, Savas Dimopoulos, and G.R. Dvali. The Hierarchy problem and new dimensions at a millimeter. *Phys.Lett.*, B429:263–272, 1998.

[31] Paul Langacker. The Physics of Heavy Z' Gauge Bosons. *Rev.Mod.Phys.*, 81:1199–1228, 2009.

[32] Lisa Randall and Raman Sundrum. A Large mass hierarchy from a small extra dimension. *Phys.Rev.Lett.*, 83:3370–3373, 1999.

[33] G.L. Bayatian et al. CMS technical design report, volume II: Physics performance. *J.Phys.*, G34:995–1579, 2007.

[34] Michael Dittmar, Anne-Sylvie Nicollerat, and Abdelhak Djouadi. Z-prime studies at the LHC: An Update. *Phys.Lett.*, B583:111–120, 2004.

[35] T. Aaltonen et al. Search for High Mass Resonances Decaying to Muon Pairs in $\sqrt{s} = 1.96$ TeV $p\bar{p}$ Collisions. *Phys.Rev.Lett.*, 106:121801, 2011.

[36] Victor Mukhamedovich Abazov et al. Search for a heavy neutral gauge boson in the dielectron channel with 5.4 fb-1 of $p\bar{p}$ collisions at sqrt(s) = 1.96 TeV. *Phys.Lett.*, B695:88–94, 2011.

[37] Georges Aad et al. Search for high-mass resonances decaying to dilepton final states in pp collisions at $\sqrt{s} = 7$ TeV with the ATLAS detector. *JHEP*, 1211:138, 2012.

[38] Georges Aad et al. Search for high-mass dilepton resonances in pp collisions at sqrt(s) = 8 TeV with the ATLAS detector. 2014.

[39] Serguei Chatrchyan et al. Search for narrow resonances in dilepton mass spectra in pp collisions at $\sqrt{s} = 7$ TeV. *Phys.Lett.*, B714:158–179, 2012.

[40] Search for Resonances in the Dilepton Mass Distribution in pp Collisions at sqrt(s) = 8 TeV. Technical Report CMS-PAS-EXO-12-061, CERN, Geneva, 2013.

[41] *The CMS magnet project: Technical Design Report.* Technical Design Report CMS. CERN, Geneva, 1997.

[42] G.L. Bayatian et al. *CMS Physics: Technical Design Report Volume 1: Detector Performance and Software.* Technical Design Report CMS. CERN, Geneva, 2006. There is an error on cover due to a technical problem for some items.

[43] Wolfgang Adam, Boris Mangano, Thomas Speer, and Teddy Todorov. Track Reconstruction in the CMS tracker. Technical Report CMS-NOTE-2006-041, CERN, Geneva, Dec 2006.

[44] R. Fruhwirth. Application of Kalman filtering to track and vertex fitting. *Nucl.Instrum.Meth.*, A262:444–450, 1987.

[45] S. Chatrchyan et al. The CMS experiment at the CERN LHC. *JINST*, 3:S08004, 2008.

[46] Serguei Chatrchyan et al. Performance of CMS muon reconstruction in pp collision events at $\sqrt{s} = 7$ TeV. *J. Instrum.*, 7(arXiv:1206.4071. CMS-MUO-10-004. CERN-PH-EP-2012-173):P10002. 81 p, Jun 2012. Comments: Submitted to the Journal of Instrumentation.

[47] Performance of muon identification in pp collisions at s**0.5 = 7 TeV. Technical Report CMS-PAS-MUO-10-002, CERN, 2010. Geneva, 2010.

[48] Particle-Flow Event Reconstruction in CMS and Performance for Jets, Taus, and MET. Technical Report CMS-PAS-PFT-09-001, CERN, 2009. Geneva, Apr 2009.

[49] Serguei Chatrchyan et al. Performance of CMS muon reconstruction in pp collision events at $\sqrt{s} = 7$ TeV. *JINST*, 7:P10002, 2012.

[50] John Allison, K. Amako, J. Apostolakis, H. Araujo, P.A. Dubois, et al. Geant4 developments and applications. *IEEE Trans.Nucl.Sci.*, 53:270, 2006.

[51] Riccardo Ranieri. The Simulation of the CMS Silicon Tracker. Technical Report CMS-CR-2008-007, CERN, Geneva, Nov 2007.

[52] Studies of Tracker Material. Technical Report CMS-PAS-TRK-10-003, 2010.

[53] K. Kondo. Dynamical Likelihood Method for Reconstruction of Events With Missing Momentum. 1: Method and Toy Models. *J.Phys.Soc.Jap.*, 57:4126–4140, 1988.

[54] K. Kondo. Dynamical likelihood method for reconstruction of events with missing momentum. 2: Mass spectra for 2 →2 processes. *J.Phys.Soc.Jap.*, 60:836–844, 1991.

[55] B. Abbott et al. Measurement of the top quark mass in the dilepton channel. *Phys.Rev.*, D60:052001, 1999.

[56] Serguei Chatrchyan et al. Measurement of the properties of a Higgs boson in the four-lepton final state. *Phys.Rev.*, D89:092007, 2014.

[57] J. Neyman and E. S. Pearson. On the problem of the most efficient tests of statistical hypotheses. *Philosophical Transactions of the Royal Society of London. Series A, Containing Papers of a Mathematical or Physical Character*, 231:pp. 289–337, 1933.

[58] Pierre Artoisenet, Vincent Lemaitre, Fabio Maltoni, and Olivier Mattelaer. Automation of the matrix element reweighting method. *JHEP*, 1012:068, 2010.

[59] Fabio Maltoni and Tim Stelzer. MadEvent: Automatic event generation with MadGraph. *JHEP*, 0302:027, 2003.

[60] Glen Cowan, Kyle Cranmer, Eilam Gross, and Ofer Vitells. Asymptotic formulae for likelihood-based tests of new physics. *Eur.Phys.J.*, C71:1554, 2011.

[61] S.S. Wilks. The Large-Sample Distribution of the Likelihood Ratio for Testing Composite Hypotheses. *Annals Math.Statist.*, 9(1):60–62, 1938.

[62] Louis Lyons, Harrison B. Prosper, and Albert De Roeck. Statistical issues for LHC physics. Proceedings, Workshop, PHYSTAT-LHC, Geneva, Switzerland, June 27-29, 2007. 2008.

[63] Pekka Sinervo. Definition and Treatment of Systematic Uncertainties in High Energy Physics and Astrophysics. *eConf*, C030908:TUAT004, 2003.

[64] Bob Cousins for CMS Statistics Committee. Probability density functions for positive nuisance parameters. Internal comittee report, May 2010.

[65] The CMS Collaboration. Search for heavy narrow dilepton resonances in pp collisions at $\sqrt{s} = 7$ TeV and $\sqrt{s} = 8$ TeV. *Phys. Lett. B*, 720(arXiv:1212.6175. CMS-EXO-12-015. CERN-PH-EP-2012-364):63–82. 27 p, Dec 2012.

[66] W Verkerke and D Kirkby. The RooFit toolkit for data modeling. Technical Report physics/0306116, SLAC, Stanford, CA, Jun 2003.

[67] Thorsten Ohl. Vegas revisited: Adaptive Monte Carlo integration beyond factorization. *Comput.Phys.Commun.*, 120:13–19, 1999.

[68] Search for Resonances in the Dilepton Mass Distribution in pp Collisions at sqrt(s) = 7 TeV. Technical Report CMS-PAS-EXO-11-019, CERN, Geneva, 2011.

[69] Lorenzo Moneta, Kevin Belasco, Kyle S. Cranmer, S. Kreiss, Alfio Lazzaro, et al. The RooStats Project. *PoS*, ACAT2010:057, 2010.

[70] MuonPOG. Reference muon id and isolation efficiencies. https://twiki.cern.ch/twiki/bin/viewauth/CMS/MuonReferenceEffs.

[71] G.Alverson at al. Seach for high-mass resonances decaying to muon pairs with collisions gathered at $\sqrt{s} = 7$ tev. CMS Note 2011/472, 2012.

[72] Absolute Calibration of the Luminosity Measurement at CMS: Winter 2012 Update. Technical Report CMS-PAS-SMP-12-008, CERN, Geneva, 2012.

[73] D Bourilkov, R C Group, and M R Whalley. LHAPDF: PDF use from the Tevatron to the LHC. 2006.

[74] B. Clerbaux at al. Statistical analysis of a resonant signal search in multiple final state modes. CMS Note 2010/312, 2011.

[75] F. James and M. Roos. Minuit: A System for Function Minimization and Analysis of the Parameter Errors and Correlations. *Comput. Phys. Commun.*, 10:343–367, 1975.

[76] F. James. MINUIT Function Minimization and Error Analysis: Reference Manual Version 94.1. 1994.

[77] J. A. Nelder and R. Mead. A Simplex Method for Function Minimization. *Comput. J.*, 7:308–313, 1965.

[78] Serguei Chatrchyan et al. Search for narrow resonances in dilepton mass spectra in pp collisions at $\sqrt{s} = 7$ TeV. *Phys. Lett. B*, 714(arXiv:1206.1849. CMS-EXO-11-019. CERN-PH-EP-2012-157):158–179. 33 p, Jun 2012.